

# Cometary Ionospheres: An Updated Tutorial

**Arnaud Beth**

Umeå Universitet

**Marina Galand**

Imperial College London

**Cyril Simon Wedlund**

Österreichische Akademie der Wissenschaften, Institut für Weltraumforschung

**Anders Eriksson**

Institutet för Rymdfysik

This chapter aims at providing the tools and knowledge to understand and model the plasma environment surrounding comets in the innermost part near the nucleus. In particular, our goal is to give an updated post-Rosetta ‘view’ of this ionised environment: what we knew, what we confirmed, what we overturned, and what we still do not understand.

## 1. INTRODUCTION

Comets have aroused the curiosity of Humankind for millennia. Reported in different ways throughout history, for instance through texts and artworks, a few of them have passed Earth close enough to be witnessed with the naked eye. But what makes comets visible and so bright? For those lucky enough to see them in their lifetime, comets in the sky display very singular shapes and colours: a very broad white tail and a thinner blue slightly transparent one, both originating from the same point where the nucleus is located. The ‘white tail’ is partly directed anti-sunward (that is, opposed to the Sun’s direction), with a component along the comet’s trajectory. It originates from the dust reflecting sunlight that is continuously expelled from the comet’s surface and pushed away, swept by the solar radiation pressure. This radiation pressure is induced by solar photons which, once they hit the dust, transfer a part of their momentum continuously to it, equivalent to a force. Depending on the size of dust grains, this force, in addition to inertial ones, is the main driver of the dust dynamics, which as a result may overcome the Sun’s gravity (Finson-Probstein model, see *Finson and Probstein* 1968).

The ‘blue’ tail itself originates from ions present in the coma. This was first evidenced in the band spectra of Comet C/1907 L2 (Daniel) (*Deslandres and Bernard* 1907; *Evershed* 1907) although its true origin was unknown at the time (*Larsson et al.* 2012). Subsequently, *Fowler* (1907, 1910) investigated these bands by means of laboratory experiments and electric discharges in different gases and concluded that carbon monoxide was the most likely cause. Fowler was *almost* right. The blue colour displayed by this tail comes in fact from the fluorescence of  $\text{CO}^+$  ions. Although the cometary gas is

mainly composed of water ( $\text{H}_2\text{O}$ ), other species are present such as carbon dioxide ( $\text{CO}_2$ ), carbon monoxide (CO), and formaldehyde (methanal,  $\text{H}_2\text{CO}$ ). As they leave the nucleus, these molecules may break into smaller fragments, neutral atoms/molecules (through photodissociation), be ionised (photoionisation), or undergo both processes at the same time (dissociative photoionisation). The newly formed  $\text{CO}^+$  may in turn be excited by absorbing solar photons at specific wavelengths and is de-excited by re-emitting a photon at the same wavelength (resonance fluorescence). Amongst cometary species,  $\text{CO}^+$  is the only one which efficiently emits in the visible, especially in the blue part (so-called ‘comet tail’ A-X bands emitting between 308–720 nm).

In almost a century, even though substantial progress has been made in astronomy and instrumentation, only a few other ions have been observed and confirmed at comets through remote sensing from Earth, for example  $\text{HO}^+$ ,  $\text{CO}_2^+$ , and  $\text{H}_2\text{O}^+$  (see the chapter by *Bodewits et al.* in this volume). Early on, another mystery was also associated with the ‘ion’ tail: its direction. Indeed, through the comet’s course around the Sun, and unlike the dust tail, the blue ion tail is exactly anti-sunward. The discovery of the solar wind was motivated by the observations of cometary ion tails from Earth. Following early works by *Hoffmeister* (1943), *Biermann* (1951) was the first to suggest then that there is a flow of ionised particles from the Sun, ‘a stream of solar matter’ (*Biermann* 1952), although why this stream could arise was another unanswered question. In 1958, Eugene Parker followed on Biermann’s lead and published his seminal paper on the generation and existence of the so-called ‘solar wind’ (*Parker* 1958), an idea which was initially ill received (*Obridko and Vaisberg* 2017).

Interestingly, contemporarily to these works, the true nature of comets and of their nucleus remained unknown. Only in 1950 did Fred Whipple formulate the idea that comets were made of a conglomerate of ices combined with a conglomerate of meteoric materials (Whipple 1950), known as the ‘dirty snowball’ nucleus model. Our modern view based on recent observations of cometary nuclei shows that comets are rather *dirt balls with some snow*. Based on this model, Haser (1957) (see Haser et al. 2020, for a modern, accessible, and translated version) later developed the mathematical framework to describe the cometary neutral environment, nicknamed ‘Haser model’ in the literature nowadays. Haser derived the mathematical formulation describing the spatial distribution and number density for neutral species, either those coming from the ice sublimation at the (near-)surface of the nucleus, the ‘parent’ species, or those coming from the dissociation of the parent species, the ‘daughter’ species. For ‘parent’ molecules, such as H<sub>2</sub>O and CO<sub>2</sub>, primarily released from the (near-)surface, the flux is conserved; the number density profile of the escaping gas of species  $p$  is thus given in m<sup>-3</sup> by:

$$n_p(r) = \frac{Q_p}{4\pi V_p r^2} \exp\left(-\frac{r}{\mathcal{T}_p V_p}\right) \quad (1)$$

where  $Q_p$  is the total number of ‘parent’ ( $p$ ) molecules expelled from the surface per unit time ([molecules s<sup>-1</sup>] or simply [s<sup>-1</sup>] for short),  $V_p$  is the radial speed of these molecules assumed constant [m s<sup>-1</sup>] estimated around 0.4–0.9 km s<sup>-1</sup> (see the chapter by Biver et al. in this volume and Hansen et al. 2016; Biver et al. 2019),  $r$  is the distance from the nucleus [m], and  $\mathcal{T}_p$  is the lifetime of these molecules against dissociation [s]. This equation remains valid for asymmetric outgassing (i.e.  $Q_p$  varies with latitude and longitude at a given  $r$  as long as the gas velocity remains radial). Usually, molecules are characterised, in a cometary context, by their so-called characteristic scale length  $L_p = V_p \mathcal{T}_p$ . This model is adequate for species and molecules that are mainly photodissociated by Extreme Ultraviolet (EUV) solar radiation, for instance H<sub>2</sub>O into HO+H. It also provides an easy way to retrieve the outgassing rate  $Q_p$  of the different cometary neutral parent species based on remote sensing observations.  $L_p$  is usually of the order of 10<sup>4</sup>–10<sup>5</sup> km corresponding to a typical lifetime of 10<sup>4</sup>–10<sup>5</sup> s (Huebner and Mukherjee 2015); the exponential correction in Eq. 1 should be accounted for when comets are observed remotely from Earth (as the full extent of the coma is probed) or when numerical simulations of the whole cometary environment are developed. Furthermore, not all neutral species may come directly from the nucleus. Some species, such as H<sub>2</sub>CO and CO, may also originate from dust and photodissociation of larger molecules already present in the coma, referred to as ‘extended sources’, and thus do not follow Eq. 1 (Eberhardt 1999). These extended sources must be accounted for as well in large-scale simulations beyond thousands of kilometres (see the chapter by Biver et al. in this volume). However, in the rest of this

chapter, the exponential term may be dropped in Eq. 1 as we are focusing on major neutral species (originating primarily from the nucleus) and on in situ observations at cometocentric distances  $r \ll L_p$ . In these regions, in situ observations performed at 1P/Halley (hereafter 1P, Krankowsky et al. 1986) and at 67P/Churyumov-Gerasimenko (hereafter 67P, Hässig et al. 2015) showed that  $n_{\text{H}_2\text{O}} \propto 1/r^2$  and Eq. 1 reduces to:

$$n_p(r) \approx \frac{Q_p}{4\pi V_p r^2} \quad \text{for } r \ll L_p \quad (2)$$

Although there are neutral species produced in part within the coma and linked to the so-called *extended sources* (Eberhardt 1999), such as CO and O, such a source can often be neglected in plasma models of the inner coma.

Similarly to Eq. 2, the total neutral number density  $n_n$  in the inner coma is given by:

$$n_n(r) = \sum_p n_p \approx \frac{Q}{4\pi V_n r^2} \quad (3)$$

where

$$V_n = \frac{1}{n_n} \sum_p V_p n_p \quad (4)$$

$Q$  is the total outgassing rate (total number of neutral species released by unit time from the (near) surface) and  $V_n$ , the mean bulk velocity of the neutral species.

The neutral gas released by sublimation of ices at the surface of the nucleus is primarily made of H<sub>2</sub>O, CO<sub>2</sub>, and CO (see the chapter by Biver et al. in this volume). Many other molecules are also present in the coma, such as dioxygen (O<sub>2</sub>), ammonia (NH<sub>3</sub>), and glycine (NH<sub>2</sub>CH<sub>2</sub>COOH), unambiguously detected in situ at 67P (Le Roy et al. 2015; Altwegg et al. 2016; Gasc et al. 2017) thanks to the mass spectrometer ROSINA (Rosetta Orbiter Spectrometer for Ion and Neutral Analysis)/DFMS (Double Focusing Mass Spectrometer, Balsiger et al. 2007). Along their path in the interplanetary medium, molecules may undergo different fates: They can be excited, dissociated into neutral fragments, or ionised by means of absorption of solar EUV radiation or impact of energetic particles. Although dissociation is more efficient than ionisation and excitation, a fraction of the molecules still undergoes ionisation; this forms a region made of plasma, a mixture of ions and electrons, surrounding the nucleus: the *ionosphere*.

Ionospheres are commonly present around any solar and extrasolar system body possessing a neutral gas layer, either an atmosphere, like at Earth, Mars, Jupiter and Titan, or an exosphere, like at Mercury or Ganymede. It plays a critical role in the interaction of the Sun (or the star) with the body. Indeed, none of these solar system bodies is isolated: They all bathe in an external plasma, either directly the solar wind for bodies without an intrinsic magnetic field or the magnetospheric plasma (and indirectly the solar wind) for magnetised bodies. Around comets, two broad types of plasma are present (see Fig.1):

- The *ionosphere* proper, made of cometary electrons and ions born from outgassed neutral molecules, is dense ( $10^2 - 10^9$  particles  $\text{m}^{-3}$ ). Cometary ions are heavy (above 12 unified atomic mass units [u] or Daltons [Da]), slow (from 0.5 to a few  $\text{km s}^{-1}$ ), and cold.
- In contrast, the *solar wind* is rarefied (1 – 10 particles  $\text{m}^{-3}$  at 1 au), made of protons ( $\text{H}^+$ ), alpha particles ( $\text{He}^{2+}$ ), and electrons ( $e^-$ ); it is fast ( $|\mathbf{V}_{\text{sw}}| = 400\text{--}800$   $\text{km s}^{-1}$ ) and hot (ion temperature  $T_i \sim 0.8 \times 10^5$  K, electron temperature  $T_e \sim 1.5 \times 10^5$  K at 1 au typically scaling to the heliocentric distance  $r_h$  as  $r_h^{-2/3}$  and  $r_h^{-1/3}$ , respectively; see *Slavin and Holzer 1981*).

The solar wind transports with itself electromagnetic fields. It carries the solar magnetic field  $\mathbf{B}_{\text{sw}}$  which is ‘frozen-in’, that is, the magnetic field is dragged into space by the expanding solar wind. Moreover, even though there is no electric field in the solar wind rest frame, as it moves, an observer in a moving frame with respect to the solar wind experiences an electric field from the advected magnetic field by means of relativistic Lorentz transformation. This field is the so-called convective or motional electric field defined as  $\mathbf{E}_{\text{sw}} = -\mathbf{V}_{\text{sw}} \times \mathbf{B}_{\text{sw}}$ . A simplistic view of the relationship between a star and comets is shown in Fig. 1.

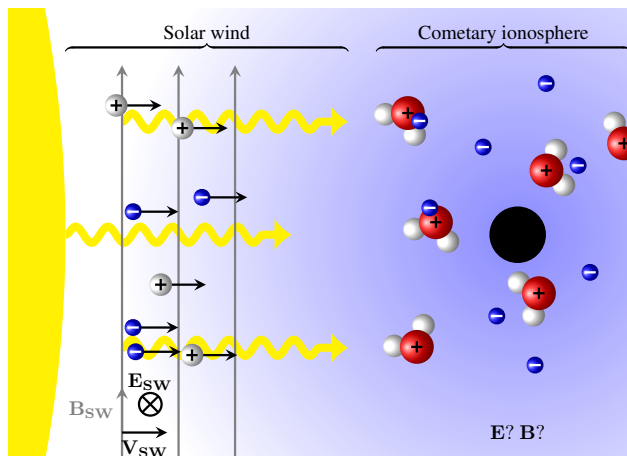


Fig. 1.— Schematic of the actors of the interaction of the comet (black disk) with its space environment. They include: (i) the cometary ionosphere, here represented by water  $\text{H}_2\text{O}^+$  ions (red/white) and electrons (blue around the coma), (ii) the solar extreme ultraviolet (EUV) radiation (yellow), responsible in part for ionising the neutral coma, and (iii) the solar wind plasma, made of  $\text{H}^+$  (white) and electrons (blue) carrying the interplanetary magnetic field (grey vertical arrows), filling the interplanetary medium and travelling at speeds typically between 400 and 800  $\text{km s}^{-1}$ . The transition between the solar wind and cometary ionosphere and the nature of this transition depend on many factors (e.g. outgassing activity, composition, heliocentric distance, etc.), discussed in detail in the chapter by Götz et al. in this volume.

The first spacecraft to visit a comet and its plasma environment was the NASA’s *International Cometary Explorer* (abbreviated *ICE*) spacecraft which flew by comet 21P/Giacobini-Zinner (21P) on 11 September 1985 at a closest approach of 7800 km through the comet’s tail (see *Farquhar 2001*). This mission was mainly dedicated to plasma measurements and was the first to provide in situ information on the interaction of the cometary ionosphere with the solar wind (*von Rosenvinge et al. 1986; Cowley et al. 1987*). *ICE* focused on the tail and could not investigate the innermost coma. Although ions of cometary origin were observed up to  $4 \times 10^6$  km from 21P’s nucleus, they were already significantly accelerated, picked-up by the solar wind convective electric field, at speeds around 150  $\text{km s}^{-1}$  (*Ogilvie et al. 1986*). At the time, mass spectrometers, which discriminate and separate ions according to their mass per charge (or simply their mass if ions are assumed singly-ionised), had a very limited mass resolution. The resolution in *mass spectrometry* is defined by  $R = m/\Delta m$  where  $m$  is the mass at which ions are measured and  $\Delta m$  is the width of the peak typically at half height (see IUPAC recommendation and nomenclature, *IUPAC 1978*). With *ICE*, the mass resolution was relatively poor, with measurements separated by 1–2  $\text{u q}^{-1}$  (mass unit per charge,  $q$  being the elementary charge in Coulomb), making it extremely difficult to separate species with relatively close molecular masses, for example  $\text{HO}^+$ ,  $\text{H}_2\text{O}^+$ , and  $\text{H}_3\text{O}^+$ .

The following year, the *Halley* armada, a fleet of five spacecraft from several space agencies (one from the European Space Agency ESA [*Giotto*], two from the Soviet Union and France [*Vega 1* and *Vega 2*] and two from the Institute of Space and Astronomical Science, now JAXA, in Japan [*Suisei* and *Sakigake*]), flew by the most famous comet of all and one of the brightest. As such, Halley’s comet was the first one to be identified as periodic (1P) with its 76-year period determined by Edmond Halley in 1705. In succession, *Sakigake*, *Vega 1*, *Suisei*, *Vega 2*, and finally *Giotto* flew by Comet 1P, each probe providing a more precise location of 1P and therefore helping the next probe to get closer to its nucleus. On 13–14 March 1986, the last spacecraft of the fleet, *Giotto*, achieved a closest approach of 600 km at a heliocentric distance  $r_h = 0.89$  au from the Sun (*Reinhard 1986*). The first detected ‘cometary’ ion was  $\text{O}^+$  (most likely candidate at the peak at  $16 \text{ u q}^{-1}$ ) at  $5.5 \times 10^5$  km from the nucleus (*Krankowsky et al. 1986*). Most likely, it resulted from the dissociation of  $\text{H}_2\text{O}$  into O followed by ionisation (*Balsiger et al. 1986*). The mass resolution was high enough to separate  $\text{HO}^+$  from  $\text{H}_2\text{O}^+$ , albeit not  $\text{O}^+$  from  $\text{NH}_2^+$  and  $\text{CH}_4^+$  ( $R \gtrsim 20$ , *Balsiger et al. 1987*).

As *Giotto* got closer to 1P’s nucleus, the ion composition changed. Between  $1.5 \times 10^5$  km and  $7 \times 10^4$  km, the cometary plasma composition was dominated by ion mass  $16 \text{ u q}^{-1}$  (most likely  $\text{O}^+$ ), followed by ion masses  $17 \text{ u q}^{-1}$  (most likely  $\text{HO}^+$ ) and  $18 \text{ u q}^{-1}$  (most likely  $\text{H}_2\text{O}^+$ ). From  $6 \times 10^4$  km to  $3 \times 10^4$  km, the order changed: mass

18  $\text{u q}^{-1}$  dominated, followed by 17  $\text{u q}^{-1}$  and 16  $\text{u q}^{-1}$ . From  $3 \times 10^4$  km to the closest approach, mass 19  $\text{u q}^{-1}$  ( $\text{H}_3\text{O}^+$ ) exceeded in counts mass 16  $\text{u q}^{-1}$ , and even dominated the overall composition below  $2 \times 10^4$  km. However, the reader should keep in mind that the main contributor at a given  $\text{u q}^{-1}$  may change during the flyby. For instance, close to the nucleus, the signal at 18  $\text{u q}^{-1}$  may be associated with  $\text{NH}_4^+$  while further away, it is more likely  $\text{H}_2\text{O}^+$  due to the ion chemistry. For this reason, ion measurements from Giotto had to be combined with photochemical models to infer the neutral and ion composition of the coma (e.g. *Allen et al.* 1987; *Geiss et al.* 1991). Furthermore, not only the composition, but also the spatial distribution of the plasma, changed. The ion count associated with cometary ions exhibited a  $1/r^2$ -dependence for cometocentric distances  $r$  beyond 16,000 km, whereas, in the innermost part of the coma, ion counts varied in  $1/r$ .

Giotto was a great mission for exploring large spatial scales around a comet in a very limited time, taking a veritable snapshot of the cometary plasma down to 600 km, the best achievement until the ESA cometary mission *Rosetta*, that escorted comet 67P over a two-year period (2014-2016), from  $r_h \sim 3.6$  au to  $r_h \sim 1.24$  au (perihelion) and back to 3.8 au at the end of mission (*Glassmeier et al.* 2007). Nevertheless, several important aspects should be kept in mind when we compare the Giotto mission to Rosetta. Comet 1P was very active ( $Q \approx 6.9 \times 10^{29} \text{ s}^{-1}$ ), close to the Sun (0.89 au), and, in that respect, its flyby by Giotto and the entire Armada is far from being representative of the whole cometary environment and development.

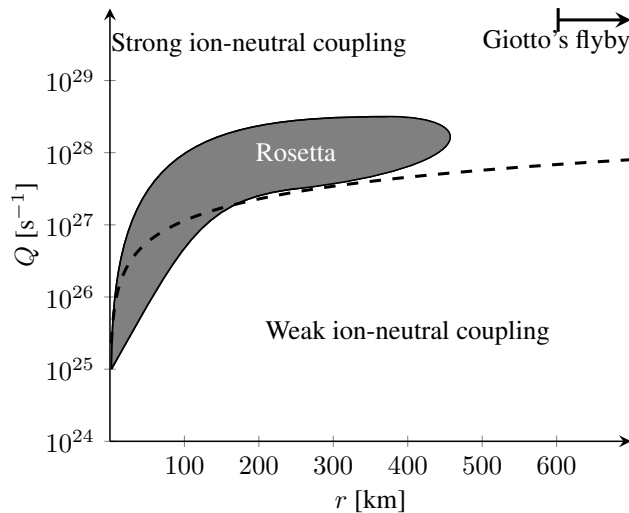


Fig. 2.— Schematic of the cometocentric distance covered by Giotto and Rosetta as a function of the outgassing activity. Excursions have been excluded. The dashed line defines the theoretical limit where ions and neutrals become collisionally decoupled (*Gombosi* 2015) referred to as  $R_{i,n}$  in this chapter.

As shown in Fig. 2, Giotto’s closest approach was quite far compared with Rosetta ranges of cometocentric dis-

tances, even when scaling these distances to their vastly different outgassing rates. Rosetta not only explored a wide range of distances, from 500 km to the surface, but also more than 3 orders of magnitude in terms of outgassing rate, from  $Q \approx 10^{25}$  to  $\sim 3 \times 10^{28} \text{ s}^{-1}$ , as 67P gradually became more active on its journey towards the inner solar system and then faded again on its outward journey. During the mission, the scientific community had thus the unique opportunity to monitor the cometary coma, the ionosphere and its relationship with the solar wind, and their combined evolution over time, providing a wealth of unprecedented scientific data. In the future, we may not have many opportunities to visit other comets with such a dedication; in this way, escorting 67P constitutes a major step forward in our understanding of solar wind-comet interactions.

This chapter proposes to look into the lessons learned from the combined past cometary flybys and the recent 2 years of escort by Rosetta, from the formation to the composition and evolution of a cometary ionosphere. It follows the example of the previous books on the matter, *Comets I* and *Comets II*. *Comets I*, published before in situ exploration of cometary environments (prior ICE and the Halley Armada), made use of remote-sensing observations from the Earth and possible theories (*Ip and Axford* 1982; *Huebner et al.* 1982), describing the solar wind assimilation into the cometary environment with the formation of plasma boundaries, and the emergence of photochemical models of the inner coma including ion-neutral gas chemistry. *Comets II* focused on the advances brought by the contemporary exploration of a very active comet, 1P/Halley, with the first attempt to compare models against in situ observations (*Ip* 2004). This chapter is a tentative harmonisation and consensus on our current knowledge of cometary ionospheres, in order to provide some sort of a ‘continuous’ picture from weakly active to very active comets. This chapter must be seen and read as a ‘tutorial’ or ‘manual’ for those who want to become familiar with cometary ionospheres; it sets the stage for future explorations of comets. In Section 2, we introduce the theory behind the formation of a cometary ionosphere and its chemical loss and discuss its plasma balance, composition, and evolution over time, in the light of both modelling and observations. In Section 3, we present and focus on the different electron populations and their role observed at comets, while in Section 4 we present and focus on the different ion populations and their behaviour. Section 5 is dedicated to the role of dust on cometary plasmas. Finally, in Section 6, we summarise the contemporary progress and discoveries made in cometary physics followed by a non-exhaustive list of open questions.

## 2. Birth of a cometary ionosphere

### 2.1. Ion continuity equations

After being ejected from the nucleus’ surface via sublimation, desorption, or other mechanisms (see the chapter by *Filacchione et al.* in this volume), the cometary neutral gas forming the coma is partially ionised by solar radiation

( $\lambda \lesssim 100$  nm, see Section 2.2.1), and by energetic electrons (Section 2.2.2) and ions (Section 2.2.3), leading to the formation of an ionosphere. The resulting ionosphere can be described by macroscopic, fundamental plasma quantities, such as the number density, mean velocity, and temperature, all in situ observables from instruments onboard a spacecraft:

- The plasma number density is the number of ions (or electrons assuming that ions only carry one positive charge  $+q$ ) per unit volume, often expressed in  $\text{m}^{-3}$ .
- The ion (resp. electron) mean (bulk) velocity is the statistical averaged velocity over all ions (resp. electrons) at a specific location, expressed in  $\text{m s}^{-1}$ .
- The ion (resp. electron) temperature represents the variance of the velocity around the mean ion (resp. electron) velocity. It can be expressed in K or in eV (where  $1 \text{ eV} \approx 1.6 \times 10^{-19} \text{ J} \approx k_B \times 11604 \text{ K}$ ,  $k_B$  being the Boltzmann constant).

Note that by virtue of quasi-neutrality of the plasma, ion and electron number densities (noted  $n_i$  and  $n_e$ ) must be ‘almost’ equal ( $n_i \approx n_e$ ). However, neither the mean velocities ( $\mathbf{V}_i$  for ions and  $\mathbf{V}_e$  for electrons) nor the temperatures ( $T_i$  and  $T_e$ ) are necessarily so.

Let us look at the ion number density. The fate of newly-born ions is manifold (see Section 2.2 for a detailed description). For instance, ions can be transported, near or away from the cometary nucleus by means of electromagnetic forces. They can also collide along their path with neutral molecules. Through such a collision, the ion may lose its charge to the benefit of the neutral species, the latter itself becoming an ion. Finally, ions may recombine with free electrons and neutralise/dissociate, creating a net loss of ions and electrons. Such processes need to be taken into account when assessing the ion number densities. This can be achieved with the use of a mathematical model based on solving a set of differential equations.

The time evolution of the number density of cometary ion species  $s$  is captured by the continuity equation, which describes the evolution of the number of particles over time and space:

$$\frac{\partial n_s(\mathbf{r}, t)}{\partial t} = - \underbrace{\nabla \cdot (n_s(\mathbf{r}, t) \mathbf{V}_s(\mathbf{r}, t))}_{\text{transport}} + \underbrace{S_s(\mathbf{r}, t)}_{\text{source}} - \underbrace{L_s(\mathbf{r}, t)}_{\text{chemical loss}} \quad (5)$$

where  $\mathbf{r}$  and  $t$ , the spatial and temporal coordinates respectively (the spatial reference frame is the comet’s inertial frame centred on its nucleus), and where:

- $\partial n_s(\mathbf{r}, t)/\partial t$  is the instantaneous temporal variation of the ion number density in the infinitesimal volume  $d\mathcal{V} = d^3\mathbf{r}$  at the position vector  $\mathbf{r}$  and time  $t$ ,
- $\nabla \cdot (n_s(\mathbf{r}, t) \mathbf{V}_s(\mathbf{r}, t))$  is the transport term and quantifies the rate at which plasma enters and leaves the

infinitesimal volume  $d\mathcal{V}$  at  $(\mathbf{r}, t)$ . It is the net outward flux (here  $n_s \mathbf{V}_s$ ) through the surface enveloping  $d\mathcal{V}$ . If there is no production and no chemical loss of ions  $s$  within  $d\mathcal{V}$ , the number density  $n_s(\mathbf{r}, t)$  depends only on the amount of ions  $s$  passing through the surface  $d\mathcal{S}$  at  $(\mathbf{r}, t)$ , the outer boundary of  $d\mathcal{V}$ . Beware that unlike some fluids, plasma is compressible (i.e.  $\nabla \cdot \mathbf{V} \neq 0$ ),

- $S_s(\mathbf{r}, t)$  is the local and instantaneous source (commensurable to a production rate) of the ion species  $s$  in the infinitesimal volume  $d\mathcal{V}$  at  $(\mathbf{r}, t)$  through ionisation or ion-neutral collisions (see Sections 2.2 and 2.3),
- $L_s(\mathbf{r}, t)$  is the local and instantaneous chemical loss rate of the species  $s$  in the infinitesimal volume  $d\mathcal{V}$  at  $(\mathbf{r}, t)$  through collisions (see Section 2.3).

All four terms in Eq. 5 are expressed in  $\text{m}^{-3} \text{s}^{-1}$ . One should note that there are as many continuity equations as there are ion species. This constitutes a challenging system to solve and therefore assumptions should be made. Physicists tend to reduce the number of independent variables, here 4: 1 for time and 3 for space.

The most practical and well justified assumption is to model the system at/near steady state, that is, in the limit of very slow variations/low frequencies and long timescales: The left-hand side of Eq. 5 becomes zero. Even if the system is disturbed, it will naturally converge and recover towards its steady state after a certain typical timescale, ruled here by transport and chemistry.

The second assumption is regarding the symmetry of the system. Although comets have various shapes, it has been shown that the neutral number density follows a  $1/r^2$  law, at least for the major species, such as  $\text{H}_2\text{O}$  and  $\text{CO}_2$  (e.g. at 67P, Hässig *et al.* 2015): This is the same as for a point source or a sphere emitting gas with a constant radial speed, as in Eq. 2. Close to the nucleus and in the first few hundred kilometres from it, this assumption appears reasonable. Farther away from the nucleus, the loss of neutrals needs to be taken into account (see Eq. 1).

Source and loss terms of cometary ions,  $S_s$  and  $L_s$  in Eq. 5, are described in detail in Sections 2.2 (net production of charge in the coma) and 2.3 (chemical production and loss of cometary ions through ion collisions with neutrals and with electrons). Solution of Eq. 5, along with the relative importance of the different terms, is discussed in Sections 2.4.1 when applied to the full plasma and in 2.4.2 when applied to individual ion species.

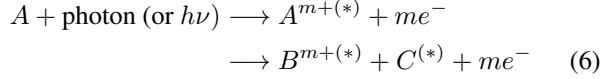
## 2.2. Source of the cometary plasma

We consider three net sources of charge for the cometary ionosphere: photoionisation by solar Extreme Ultraviolet (EUV) radiation (see Section 2.2.1), ionisation by energetic electrons (see Section 2.2.2) and ionisation and charge exchange by solar wind ions (see Section 2.2.3). The relative importance of each of these sources is reviewed in Sec-

tion 2.2.4. Complementarily, the reader is directed to other textbooks on the matter (*Schunk and Nagy 2009*).

### 2.2.1. Photoionisation

Photoionisation is the process of absorption of a sufficiently energetic photon by an atom/molecule  $A$  and the subsequent ejection of one or several of its bound electrons. This is a main plasma production process leading to the formation of an ionosphere at any solar system body with a gas envelop:



where  $m$  is the number of electrons released in the process (in most cases  $m = 1$ ) and the star  $*$  denotes a possible excited state of the ion  $A^{m+}$ ,  $B^{m+}$ , and/or the neutral species  $C$ . Photoionisation can produce new neutral atoms or molecules (here  $C$ ) if  $A$  is a molecule: The atoms constituting  $B$  and  $C$  together constituted  $A$ . The produced ion and/or the neutral may be in an excited state and emissions are produced when the de-excitation is radiative (see the chapter by Bodewits et al. in this volume). The efficiency of an photoionisation is linked to the *cross section* associated with the absorbing neutral species and produced ion species. The cross section depends on the energy (or wavelength  $\lambda$ ) of the photon absorbed, that is  $E = h\nu = hc/\lambda$  where  $h$  is the Planck constant, and the targetted neutral species.

For the most common molecules encountered around comets, photoionisation is triggered by photons of energy  $E \gtrsim 12$  eV ( $\lambda \lesssim 100$  nm) corresponding to the EUV range. The minimum energy can be lower in the case of alkali metals. Photoionisation depends on the distribution in energy of the incoming photons. First, the EUV spectrum significantly departs from the black body emission (see Fig. 3). Second, this spectrum is composed of emission ‘lines’ in the EUV/soft X-ray range originating mainly from the chromosphere, the transition region and the solar corona; They are emitted by excited (often highly ionised) species, such as H, He, C, O, Si, Fe, etc. (*Lean 1991*, see Fig. 3). The EUV photon energy distribution strongly depends on the solar activity and solar cycle.

In order to obtain an expression of the photoionisation source term in Eq. 5, several steps are necessary. These are detailed below. The starting point is to compute the resulting efficiency of the solar EUV flux in ionising neutrals. It is determined by the photoionisation frequency of neutral species  $p$  leading to the production of ion species  $s$ :

$$\nu_{p,s}^{h\nu,\text{ioni}}(\mathbf{r}) = \int_{\lambda_{\min}}^{\lambda_{p,s}^{\text{th}}} \sigma_{p,s}^{h\nu,\text{ioni}}(\lambda) F_{h\nu}(\lambda, \mathbf{r}) d\lambda \quad (7)$$

where:

- $F_{h\nu}(\lambda, \mathbf{r})$  [photons  $\text{m}^{-2} \text{s}^{-1} \text{nm}^{-1}$ ] is the spectral flux of the solar radiation at the position vector  $\mathbf{r}$

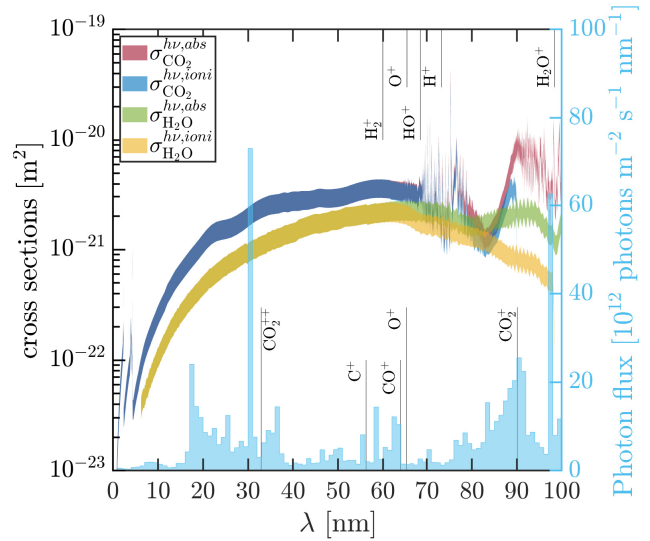


Fig. 3.— Left axis: Total photoabsorption ( $\sigma^{h\nu,\text{abs}}$ ) and photoionisation ( $\sigma^{h\nu,\text{ioni}}$ ) cross sections for  $\text{H}_2\text{O}$  and  $\text{CO}_2$  as a function of wavelength. Associated wavelength appearances for ionised products are indicated (top for  $\text{H}_2\text{O}$ , bottom for  $\text{CO}_2$ ). Right axis: EUV solar photon flux on 16 July 2016 between 0 and 100 nm from TIMED/SEE measured at Earth, normalised at 1 au, integrated over 1 nm-wide bins. Photoionisation and photoabsorption cross sections are from *Heays et al. (2017)* and references therein. Wavelength appearances are from *Zavilopulo et al. (2005)*.

(where the origin is taken at the centre of the nucleus,  $|\mathbf{r}| = r$  corresponds to the cometocentric distance). It is derived from Eq. 11,

- $\sigma_{p,s}^{h\nu,\text{ioni}}(\lambda)$  [ $\text{m}^2$ ] is the photoionisation cross section proportional to the probability to have the neutral species  $p$  absorbing a photon of wavelength  $\lambda$  and forming the ion species  $s$  (see Fig. 3),
- $\lambda_{p,s}^{\text{th}}$  is the maximum wavelength triggering the process; it corresponds to a threshold energy typically around 12 eV, referred to as the *ionisation energy*  $E_{p,s}^{\text{th}}$  (or archaically *ionisation potential*). For example, water has an ionisation energy of 12.5 eV (99.2 nm, see Fig. 3); if there is dissociation and/or excitation during the ionisation, the threshold energy has a value higher than for a single, non-dissociative ionisation generating all products in the ground state,
- $\lambda_{\min}$  is the minimum wavelength observable in the solar spectrum, approximately around 0.1 nm. Below this limit, the solar photon flux becomes negligible, even during flares.

As photons penetrate the dense coma, the amount of absorbed photons by cometary molecules becomes more and more significant. This results in the solar spectral flux being attenuated as the coma gets thicker and thicker, a process

known as *photoabsorption*. Photoabsorption at the position vector  $\mathbf{r}$  depends on the total column density  $N_p$  of neutral species  $p$  crossed by photons from a position  $\mathbf{r}_\infty$  along the line of sight (where the distance  $r_\infty$  is large enough such that there is no significant absorption of solar photons sunward of  $\mathbf{r}_\infty$  along the line of sight) to  $\mathbf{r}$ . It is defined as:

$$N_p(\mathbf{r}) = \int_{l=0}^{l=l_\infty} n_p(\mathbf{r}'(l)) dl \quad (8)$$

where  $l$  represents the curvilinear abscissa along the Sun-comet line of sight between the point of interest  $\mathbf{r}$  and  $\mathbf{r}_\infty$  (see Fig. 4). The number density  $n_p$  decreases fast enough for  $N_p$  to be finite. For a comet, the neutral number density decreases as  $1/r^2$  (see Eq. 2) and therefore the neutral column density is given by:

$$N_p(r, \chi) = \frac{Q_p}{4\pi V_p} \frac{\chi}{r \sin \chi} \quad (9)$$

where  $\chi$  is the solar zenith angle between  $\mathbf{r}$  and the direction of the Sun ( $\chi = 0^\circ$  in the subsolar direction, see Fig. 4). Eq. 9 neither accounts for asymmetric outgassing nor adiabatic acceleration of the neutral gas. However, it gives an idea of how strong photoabsorption is.

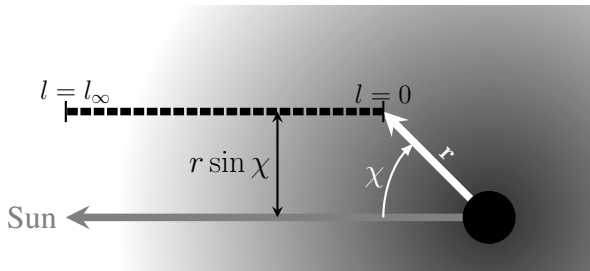


Fig. 4.— Schematic of the geometry of solar photon beams near the cometary nucleus (black disk) illustrating different quantities introduced in Eqs. 8 and 9, see text for further explanation.

To quantify the ‘thickness’ of a coma regarding the penetration of photons of wavelength  $\lambda$ , the dimensionless ‘optical depth’  $\tau$  is defined as:

$$\tau(\lambda, \mathbf{r}) = \sum_p \sigma_p^{h\nu, \text{abs}}(\lambda) N_p(\mathbf{r}) \quad (10)$$

where the subscript  $p$  refers to a specific neutral species and  $\sigma_p^{h\nu, \text{abs}}(\lambda)$  is the total photoabsorption cross section of the cometary neutral species  $p$  representing the probability of a photon of wavelength  $\lambda$  to be absorbed by the neutral species  $p$ , regardless of the process (ionisation, dissociation, excitation, see Fig. 3). The solar photon spectral flux  $F_{h\nu}(\lambda, \mathbf{r})$  at the location  $\mathbf{r}$  in the coma is then given by a simple Beer-Lambert law:

$$F_{h\nu}(\lambda, \mathbf{r}) = F_{h\nu, 1 \text{ au}}(\lambda) \exp[-\tau(\lambda, \mathbf{r})/r_h^2] \quad (11)$$

where  $F_{h\nu, 1 \text{ au}}$  is the observed spectral flux measured near Earth, for example by TIMED/SEE (*Woods et al. 2005*) and normalised to 1 astronomical unit [au], and  $r_h$  is the heliocentric distance given in au. Eq. 11 does not take into account the temporal variation of the solar EUV flux nor the phase shift correction. The latter stems from the fact that the solar EUV radiation varies with ecliptic solar longitude and that the comet is not aligned with Earth. It is then necessary to take into account the phase shift between Earth and the comet from the Sun in terms of days. For example, if the phase angle (i.e. the angle formed by Earth, the Sun, and the comet in the solar equatorial plane) is  $+90^\circ$ , the reader interested in the solar EUV radiation at the comet on day  $d$  should look for the solar EUV radiation measured at Earth,  $\sim 6.5$  days before (one fourth of the solar synodic period). Applying Eq. 11, Eq. 7 becomes:

$$\nu_{p,s}^{h\nu, \text{ioni}}(\mathbf{r}) = \int_{\lambda_{\text{min}}}^{\lambda_{p,s}^{\text{th}}} \sigma_{p,s}^{h\nu, \text{ioni}}(\lambda) \frac{F_{h\nu, 1 \text{ au}}(\lambda)}{r_h^2} \exp[-\tau(\lambda, \mathbf{r})] d\lambda \quad (12)$$

For  $\tau(\lambda, \mathbf{r}) \lesssim 0.1$ , the coma is optically thin at  $\mathbf{r}$  for photons of wavelength  $\lambda$ . Photoabsorption is thus negligible and the photoionisation frequency is constant (independent of  $\mathbf{r}$ ), reducing to:

$$\nu_{p,s}^{h\nu, \text{ioni}} = \int_{\lambda_{\text{min}}}^{\lambda_{p,s}^{\text{th}}} \sigma_{p,s}^{h\nu, \text{ioni}}(\lambda) \frac{F_{h\nu, 1 \text{ au}}(\lambda)}{r_h^2} d\lambda \quad (13)$$

For  $\tau(\lambda, \mathbf{r}) \gtrsim 0.1 - 1$ , the coma is optically thick at  $\mathbf{r}$  for photons of wavelength  $\lambda$ . In this case, photoabsorption needs to be taken into account as the solar flux is attenuated at  $\mathbf{r}$ . The coma was optically thick in the vicinity of the nucleus but not necessarily at the spacecraft location during the flyby of 1P by Giotto and during the escort of 67P by Rosetta near perihelion, though in both cases the spacecraft was far enough from the nucleus such that the ionospheric density at the location of the spacecraft was not affected by the photoabsorption occurring closer to the nucleus (*Heritier et al. 2018; Beth et al. 2019*). We can now calculate the production rate, through photoionisation, for the ion species  $s$  contributing to the source term in Eq. 5:

$$S_s^{h\nu}(\mathbf{r}) = \sum_p S_{p,s}^{h\nu}(\mathbf{r}) \quad (14)$$

where  $S_{p,s}^{h\nu}$  is the production of an ion  $s$  from photoionisation of the neutral species  $p$  given by:

$$S_{p,s}^{h\nu}(\mathbf{r}) = \nu_{p,s}^{h\nu, \text{ioni}}(\mathbf{r}) n_p(r) \quad (15)$$

The total photoionisation rate or photoelectron production rate (as only one electron is usually produced per ionisation process) is then simply given by:

$$S_{e^-}^{h\nu}(\mathbf{r}) = \sum_{p,s} S_{p,s}^{h\nu}(\mathbf{r}) \quad (16)$$

What are the typical behaviour and spatial distribution of this photoelectron production rate in the coma? For

$\tau(\lambda, \mathbf{r}) < 0.1$ ,  $S_e^{h\nu}$  is proportional to  $n_p$ , that is, to  $1/r^2$ . For  $\tau \gtrsim 0.1 - 1$ ,  $S_e^{h\nu}$  has additionally a spatial dependence associated with the optical depth. One might be interested in the location where most of the EUV radiation is absorbed within the coma and deposits its energy. This maximum absorption, which corresponds to a maximum in the photoelectron production rate is taking place as a result of the neutral number density increasing with decreasing  $r$ , while the solar flux decreases. For a monochromatic radiation, single-species coma, and for a fixed  $\chi$ , the photoelectron production rate induced by the absorption of photons at wavelength  $\lambda$  is maximum where (Beth et al. 2019):

$$\tau(\lambda, \mathbf{r}) = 2 \quad (17)$$

The value of 2 at the maximum production differs from what is usually encountered at planetary objects (including moons with a dense atmosphere such as Titan). At these bodies, the atmosphere can be assumed to be in hydrostatic equilibrium and hence varies exponentially with decreasing altitude: The maximum of absorption and of production rate thus occurs at  $\tau = 1$  (e.g. Schunk and Nagy 2009) instead of 2.

From Eq. 9 and 10, equality 17 is reached at a cometocentric distance corresponding to:

$$r_{p,s}^{\max, \text{abs}}(\lambda, \chi) = \frac{\sigma_p^{h\nu, \text{abs}}(\lambda) Q_p}{8\pi V_p} \frac{\chi}{\sin \chi} \quad (18)$$

As shown in Fig. 5, the spatial variation in the Sun-comet plane of the photoelectron production rate for a monochromatic solar radiation can be very asymmetric as the comet becomes more active (increasing outgassing rates lead to an increased optical depth). For an optically thin coma ( $\tau \ll 2$ ), the photoelectron production only depends on the cometocentric distance: Photoelectrons are produced uniformly, only as a function of the local neutral density. However, for  $\tau \geq 0.1 - 1$ , this changes. The neutral column density becomes high enough to significantly attenuate the photon flux, reducing the ionisation efficiency. Photoelectrons are thus produced in most numbers along the Sun-comet axis. As the outgassing rate increases, this maximum is located at a gradually increasing cometocentric distance upstream of the nucleus.

The photoelectron production rate is not constant along the lines of constant  $\tau$  as, for a given value of  $\tau$  and  $\lambda$ , both the neutral number density and the column density of absorption depend on  $\mathbf{r}$ . This is of importance as, when considering all wavelengths, the total photoelectron production rate will result from the sum of different production profiles through the coma. Each profile is associated with a different energy distribution of the photoelectrons which varies with cometocentric distance. The energy of the newborn photoelectron is given by:  $E_{e_{h\nu}}^- = E_{h\nu} - E_{p,s}^{th}$  where  $E_{h\nu}$  is the solar photon energy.

Above 20 eV,  $\sigma_{\text{H}_2\text{O}}^{h\nu, \text{abs}}$  decreases with energy, meaning that the maximum of absorption occurs closer to the nucleus for photons at 100 eV than those at 20 eV. Where

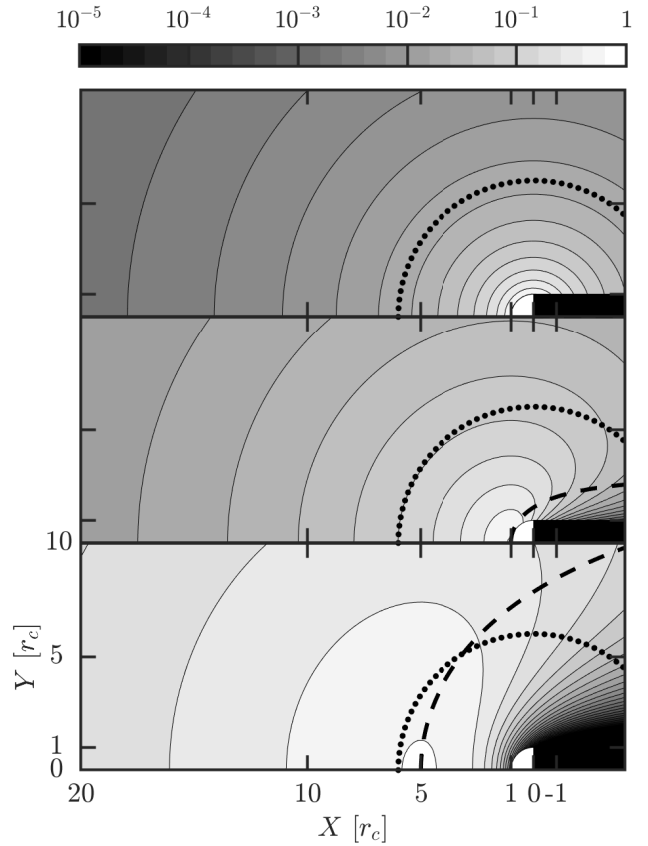


Fig. 5.— Normalised photoelectron production rate for a monochromatic radiation in a pure water coma for different cometary activities using Eq. 16. The Sun-comet axis is along  $X$ , with origin at the nucleus' centre, whereas the terminator plane is along  $Y$ . Instead of setting the outgassing rate, we set three different optical depths on the surface at the subsolar point ( $X = r_c$  at  $\chi = 0$ ): 0.01 (top panel, low activity), 2 (centre panel, intermediate activity), 10 (bottom panel, high activity). The dashed line refers to the optical depth level  $\tau = 2$ , along which the neutral column density is constant. The neutral number density described by Eq. 2 is constant along the dotted lines (spherical symmetry). Cometocentric distances in the  $X - Y$  plane are expressed in terms of nucleus' radius,  $r_c$ .

photons at 100 eV are efficiently absorbed and ionise the neutral species, photons at 20 eV cannot do so as they have been absorbed upstream due to their larger photoabsorption cross sections. Therefore, the energy distribution of photoelectrons is depleted around 20 eV when the coma starts to be optically thick. Nevertheless, the 100 eV photons produce highly energetic electrons, which in turn impact neutral molecules to produce secondary electrons. This accounts for the main ionisation source close to the nucleus for highly active comets, above  $Q = 10^{29} - 10^{30} \text{ s}^{-1}$  (Bhardwaj 2003).

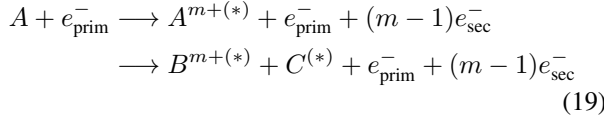
For more information regarding photoionisation and photoabsorption, the reader is invited to read the historic



work of *Chapman* (1931) initially developed for planetary atmospheres under hydrostatic equilibrium (exponentially decreasing with height) and monochromatic radiation. The theoretical application to comets hosting an expanding coma is presented in full by *Beth et al.* (2019).

### 2.2.2. Electron-impact ionisation

Electron-impact ionisation (sometimes refers as electron ionisation) is another critical process in the birth of a cometary ionosphere (e.g. *Heritier et al.* 2018). Like photons, free electrons, with an energy above the ionisation energy  $E_{p,s}^{th}$  ( $\approx 12$  eV) efficiently tear off electrons attached to an atom/molecule  $A$  following:



where subscripts ‘prim’ (resp. ‘sec’) refer to the primary impacting electron (resp. the secondary electron, freed during the ionisation). The impacting electron can be a photoelectron, a solar wind electron, or a secondary electron (see 3.1.3). It loses energy through the ionisation: It loses the ionisation energy to the neutral target, and eventually more whether one or more products are left in excited states and/or if  $A$  is dissociated, plus a fraction of it that is passed on to the secondary electron as kinetic energy. The corresponding electron-impact ionisation frequency is given by:

$$\nu_{p,s}^{e^-, \text{ioni}}(\mathbf{r}) = \int_{E_{p,s}^{th}}^{+\infty} \sigma_{p,s}^{e^-, \text{ioni}}(E) F_{e^-}(\mathbf{r}, E) dE \quad (20)$$

where  $F_{e^-}(E)$  is the electron flux (also referred sometimes as differential flux) given in (electrons)  $\text{m}^{-2} \text{s}^{-1} \text{eV}^{-1}$  and  $\sigma_{p,s}^{e^-, \text{ioni}}$  is the electron-impact cross section of the neutral species  $p$  leading to the ion species  $s$  (see Fig. 6). This formula is very similar to Eq. 7 except that (i) solar spectral flux is replaced by electron flux and (ii) the problem is defined in terms of energy instead of wavelength.

We can now calculate the electron-impact production rate for the ion species  $s$  contributing to the source term in Eq. 5:

$$S_s^{e^-}(\mathbf{r}) = \sum_p S_{p,s}^{e^-}(\mathbf{r}) \quad (21)$$

where  $S_{p,s}^{e^-}$  is the electron-impact ionisation rate of cometary neutral  $p$  leading to the production of a new cometary ion  $s$  and given by:

$$S_{p,s}^{e^-}(\mathbf{r}) = \nu_{p,s}^{e^-, \text{ioni}}(\mathbf{r}) n_p(r) \quad (22)$$

Although it is an endothermic reaction (the ionisation energy is lost), the repartition of the remaining energy between the primary and secondary electrons varies. In extreme cases, when the incident electron is very energetic, above 200–300 eV, two electrons can be kicked out through

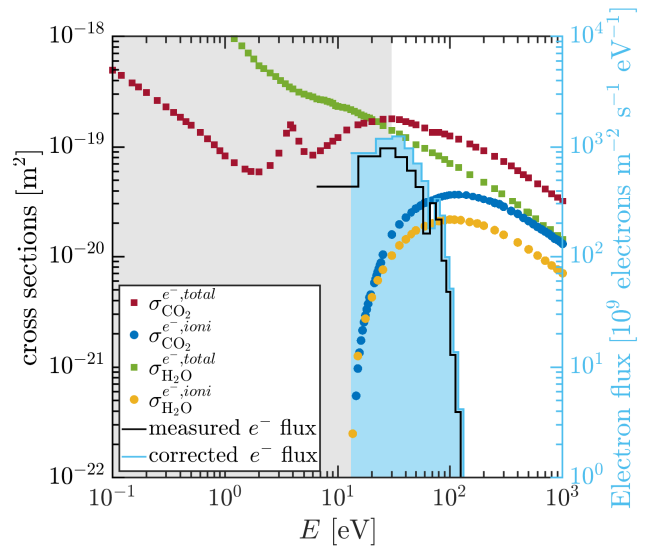


Fig. 6.— (Left axis) Total and ionisation cross sections resulting from the impact of electrons on  $\text{H}_2\text{O}$  and  $\text{CO}_2$ . (Right axis) Raw and corrected (from the spacecraft potential) electron flux by the electron spectrometer onboard Rosetta on 14 January 2015 00:06:59 (*Stephenson et al.* 2021). The grey region represents values of  $-qV_{\text{SC}}$  during Rosetta’s mission (see Section 3.1.1 for fuller explanation). It represents the minimal energy required by an electron to reach the spacecraft. Cross sections are from *Itikawa* (2002) for  $\text{CO}_2$  and *Itikawa and Mason* (2005) for  $\text{H}_2\text{O}$ .

the ionisation process. This can also occur with energetic photons of the same energy. Such high-energy primaries may lead to a process known as the *Auger effect* (*Auger* 1923), caused by the ejection of an electron from the innermost atomic or molecular shells (K-shell) and the subsequent filling of that gap with a higher-shell electron, itself leading to photoemission and/or emission of a so-called *Auger electron* (*Fox et al.* 2008).

It is important to note that the produced ion  $A^+$  in Reaction 19 can be in an excited state  $A^{+*}$ , in a similar way to photoionisation: its radiative de-excitation towards a lower excited state (ultimately ground state) leads to the emission of a photon in the FUV-Visible range, a process at play most famously in cometary ion tails, but also in aurora-like structures throughout the solar system and recently discovered at comets (see *Galand et al.* 2020, and the chapter of *Bodewits et al.* in this volume for more detail).

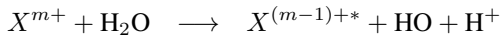
### 2.2.3. Charge-exchange and ionisation by solar wind ions

In addition to solar photons and energetic electrons, energetic ions emitted by the Sun, such as protons ( $\text{H}^+$ ) and alpha particles ( $\text{He}^{2+}$ ), may ionise the neutral species surrounding the comet. This generally occurs either through (*Simon Wedlund et al.* 2019b; *Simon Wedlund et al.* 2020):

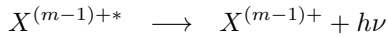
- direct impact ionisation, as for energetic electrons; we refer to it as *Solar Wind Ionisation* (SWI),

- *charge-exchange processes* (with no *net* production of charge), referred to as SWCX in the following.

As solar wind energetic ions pass through the coma, they may strip electrons from the neutral atoms and molecules they encounter, thereby lowering their charge state. The first evidence of such a phenomenon was reported by *Lisse et al.* (1996), who observed at Comet Hyakutake C/1996 B2 a strong sunward emission of the coma in the X-Ray and EUV ranges. Quickly after, *Cravens* (1997a) identified the mechanism behind these emissions. Solar wind plasma is not only formed of protons and alphas, but also of heavier ions amounting to a small proportion ( $< 0.1\%$ ) of the total solar wind density. These ions, highly charged because of their origin in the deep solar corona, are for example  $O^{m+}$ ,  $C^{m+}$ , and  $N^{m+}$  (noted  $X^{m+}$  in the following), where  $m \geq 4$  is their charge number (*von Steiger et al.* 2000). Such ion species have large and very different first ionisation energies  $E_i$ , that is, the minimum energy required to eject an electron from an isolated atom/molecule in the gaseous phase (*Muller* 1994). As they stream through the coma, multiply-charged heavy ions undergo collisions with cometary molecules, such as water:

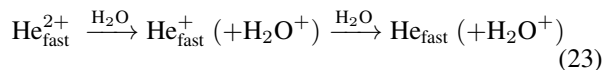


a dissociative ionisation process followed by radiative de-excitation:



The emitted photons have typical wavelengths below about 12 nm ( $\sim 100$  eV), placing them in the soft X-ray (roughly 0.1–10 nm) and EUV ranges (*Cravens* 2002; *Krasnopolsky et al.* 2004). SWCX is responsible for global X-ray and EUV emissions not only at comets, but also throughout the Universe (*Dennerl* 2010). Starting with comets, it has only recently become a rich subject of investigation and neutral gas diagnostic in astrophysics and space physics, from supernova remnants (*Lallement* 2012) to planetary magnetospheres and exospheres (*Bhardwaj et al.* 2007), with applications in fusion plasmas (*Dennerl et al.* 2012; *Semay et al.* 2012). Moreover, laboratory measurements of charge-transfer processes have also experienced an unprecedented ‘boom’ over the last two decades (see *Wargelin et al.* 2008; *Simon Wedlund et al.* 2019c, and the chapter by *Bodewits et al.* in this volume).

SWCX does not only concern heavy solar wind ions: Protons and alphas constituting the bulk of the solar wind are also subject to it (*Simon Wedlund et al.* 2019a), although they do not produce such energetic photons. In this case, the main effect of SWCX is to neutralise the solar wind (creating H and He energetic neutral atoms or ENAs, from incoming protons alphas, respectively) and implant heavier cometary ions into the solar wind flow so that, for example for alpha particles:



This in turn partakes of the so-called *mass/momentum-loading* of the solar wind as the newly-born  $H_2O^+$  molecules are accelerated by the convective electric field (see Section 4.2 and the chapter by *Götz et al.* in this volume).

For a solar wind ion species  $sw$  (e.g.  $H^+$ ) charge-exchanging with a heavy neutral species  $p$  (e.g.  $H_2O$ ) thereby creating heavy ion species  $s$  (e.g.  $H_2O^+$ ), the charge-exchange frequency  $\nu_{p,s}^{sw,CX}$  can be expressed as:

$$\nu_{p,s}^{sw,CX}(\mathbf{r}) = \int_{E_{p,s}^{th,CX,sw}}^{+\infty} \sigma_{p,s}^{sw,CX}(E) F_{sw}(\mathbf{r}, E) dE \quad (24)$$

where  $F_{sw}$  [ $m^{-2} s^{-1} eV^{-1}$ ] is the attenuated flux of solar wind ions  $sw$  at the position  $\mathbf{r}$ ,  $\sigma_{p,s}^{sw,CX}$  the corresponding charge-exchange cross section, and  $E_{p,s}^{th,CX,sw}$  the threshold energy of the reaction involving solar wind ion species  $sw$  reacting with the neutral species  $p$  to form ion species  $s$ . SWCX is a cumulative process, hence the flux of solar wind ions is progressively attenuated the deeper they penetrate in the coma, whereas keeping most of its initial energy (at least to a first approximation). Assuming straight-line trajectories with no energy change of the solar wind along the Sun-comet axis even after charge-exchange, this translates to (*Simon Wedlund et al.* 2016; *Simon Wedlund et al.* 2019a):

$$F_{sw}(\mathbf{r}, E) = F_{sw}^{\infty}(E) \exp\left(-\sum_{p,s} \sigma_{p,s}^{sw,CX}(E) N_p(r, \chi)\right)$$

where  $F_{sw}^{\infty}$  is the upstream ‘undisturbed’ solar wind flux,  $N_p(r, \chi)$  the neutral column density at distance  $r$ , assuming cylindrical symmetry along the Sun-comet axis of the neutral coma, and solar zenith angle  $\chi$ , defined in Eq. 9.

Similarly to photoionisation and electron ionisation processes, and summing through all solar wind ion species  $sw$ , the source term for charge-exchange reactions leading to the production of a new cometary ion  $s$ :

$$S_{p,s}^{CX}(\mathbf{r}) = \sum_{sw} \nu_{p,s}^{sw,CX}(\mathbf{r}) n_p(r) \quad (25)$$

Compared to photoionisation and electron ionisation, SWCX is expected to be a minor source of new plasma in the inner coma. That said, large-scale 3D numerical simulations of the cometary plasma environment have shown that it is one of the most important processes responsible for the formation of boundaries upstream of the inner ionosphere (*Simon Wedlund et al.* 2017, and the chapter of *Götz et al.* in this volume).

Because charge-exchange processes have large interaction cross sections (and thus efficiencies), SWCX production rates usually dominate those of SWI. This is especially true outside transient solar wind phenomena such as Coronal Mass Ejections (CME) or Co-rotating Interaction Regions (CIR), which carry away particles at much larger bulk speeds (up to  $\sim 1-3 \times 10^3$  km  $s^{-1}$ ) than the nominal ‘slow’

solar wind ( $\sim 400 \text{ km s}^{-1}$  or  $\sim 833 \text{ eV u}^{-1}$ ). The explanation is straightforward: SWCX cross sections peak below  $1 \text{ keV u}^{-1}$  whereas proton and helium ionisation cross sections in  $\text{H}_2\text{O}$  and  $\text{CO}_2$  have their maximum above that limit (Simon Wedlund *et al.* 2019c).

#### 2.2.4. Which ionisation sources matter at comets?

The relative importance of each separate source of cometary ions, namely photoionisation (see Section 2.2.1), electron-impact ionisation (see Section 2.2.2), and solar wind charge-exchange (see Section 2.2.3), depends on outgassing activity and cometocentric distance (Heritier *et al.* 2018; Simon Wedlund *et al.* 2019b; Simon Wedlund *et al.* 2020). Whereas solar wind charge exchange plays an important role at large cometocentric distances, typically far upstream of the comet, the production of ions in the inner ionosphere is heavily driven by electron-impact ionisation and photoionisation. For example, at comet 67P, Rosetta made it possible to monitor the ionisation frequencies of each of these sources individually from low to high outgassing rates. Outside of the so-called *solar wind ion cavity* (see Section 4.3, the chapter by Götz *et al.* in this volume, and Fig. 13), the electron-impact ionisation frequency was on average 5–10 times larger than that of photoionisation, the latter a factor 10 (respectively, 100) or so larger than solar wind charge-exchange (ionisation) frequencies, except for exceptional solar transient events when charge exchange could briefly rival the other two main ionisation sources. Inside the *solar wind ion cavity*, photoionisation frequencies at the cometocentric distances probed by the spacecraft steadily increased with decreasing heliocentric distance, to progressively dominate over electron-impact ionisation frequencies by the time the comet reached perihelion (Heritier *et al.* 2018).

### 2.3. Centre of chemical reactions

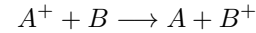
Beside the net production of charge in the coma presented in Section 2.2, there are additional chemical processes which contribute to the source and loss terms,  $S_s$  and  $L_s$ , in Eq. 5 (see Section 2.1). Firstly, there are ion-neutral collisions, which heavily influence the cometary ion composition. Through such processes, there is no net change in charge in the coma, but there is a change in cometary ion species: it is a loss for the reacting ion and a production for the new ion species formed. Secondly, there are electron-ion dissociative recombination reactions, through which there is a net loss of charge. These two types of processes are presented hereafter.

At low outgassing activity (at large heliocentric distances), a coma can be described as a quasi-collisionless medium. In the case of comet 67P, farther than 3 au, the outgassing rate was lower than  $10^{26} \text{ s}^{-1}$ , which corresponds to two 1.5-l bottles of water released to space each second. Hence, the probability of collisions between ions and neutrals was low. As the comet gets closer to the Sun and the outgassing activity grows, ion-neutral collisions occur more

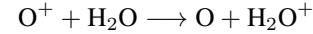
often and chemistry becomes increasingly effective within the inner coma, generating a rich zoo of ion species (Beth *et al.* 2020).

What are the different key chemical processes contributing to the sources  $S_s$  and losses  $L_s$  in Eq. 5? These are:

- **charge exchange:** through the collision of a cometary ion  $A^+$  with an atom/molecule  $B$ ,  $A^+$  captures an electron from  $B$ , such that



For example

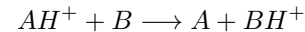


This is similar to an oxidation-reduction reaction but here in the context of gases:  $B$  is oxidised and  $A$  is reduced. Mathematically, this translates into the ion source/loss rates, as follows:

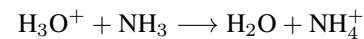
$$S_{B^+} = L_{A^+} = k_{A^+,B}(T) n_{A^+} n_B \quad (26)$$

where  $k(T)$  [ $\text{m}^3 \text{ s}^{-1}$ ] is the reaction rate coefficient, which depends on the temperature of the gas  $T$ ,  $n_B$  [ $\text{m}^{-3}$ ] is the local number density of neutral species  $B$ , and  $n_{A^+}$  [ $\text{m}^{-3}$ ] is that of ion species  $A^+$ . This process is a chemical source for  $B^+$  ( $S_{B^+}$ ), while it is a chemical loss for  $A^+$  ( $L_{A^+}$ ). For single electron capture, there is no net production of ions since we start with one ion and end up with another.

- **proton transfer:** through the collision of a cometary ion  $AH^+$  with an atom/molecule  $B$ , a proton is transferred from  $AH^+$  to  $B$  such that:



For example



Mathematically, this translates into the ion source/loss rates, as follows:

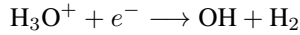
$$S_{BH^+} = L_{AH^+} = k_{AH^+,B}(T) n_{AH^+} n_B \quad (27)$$

This process is a chemical source for  $BH^+$  ( $S_{BH^+}$ ), while it is a chemical loss for  $AH^+$  ( $L_{AH^+}$ ). Compared with charge transfer, this reaction produces ‘unique’ ions. For example, whereas  $\text{H}_2\text{O}^+$  can be produced both through ionisation of  $\text{H}_2\text{O}$  and charge transfer,  $\text{NH}_4^+$  can only be produced through protonation of  $\text{NH}_3$ . Thus, the existence of  $\text{BH}^+$  (e.g.  $\text{NH}_4^+$ ) does not imply that of  $\text{BH}$  (e.g.  $\text{NH}_4$ ). This process is governed by the proton affinity (PA) of both neutral species  $A$  and  $B$ . This reaction occurs only if  $B$  has a higher PA than  $A$ . In the context of cometary ionospheres, this is of importance and pointed out initially by Aikin (1974), the first to apply ion-neutral gas chemistry at comets. Through ionisation, the main ion produced is  $\text{H}_2\text{O}^+$  (which may be loosely seen as protonated hydroxyl

radical HO-H<sup>+</sup>). Any neutral with a higher proton affinity than HO (PA(HO)= 6.15 eV) may steal the proton from H<sub>2</sub>O<sup>+</sup> to be in turn protonated. Amongst cometary neutrals, candidates include: H<sub>2</sub>O (7.16 eV), H<sub>2</sub>S (7.30 eV), H<sub>2</sub>CO (7.39 eV), HCN/HNC (7.39/8.00 eV), and NH<sub>3</sub> (8.84 eV) (Hunter and Lias 1998). Ammonia, the latter, is thus at the top of the ‘proton food’ chain. In the coma, once protonated ammonia NH<sub>4</sub><sup>+</sup> (ammonium ion) is formed, it is only destroyed through recombination with electrons or transport, and therefore it should persist for a long time (as such, it is referred to as terminal ion). The mass resolution of the ROSINA/DFMS mass spectrometer onboard Rosetta was high enough to unambiguously identify it for the first time at a comet, differentiating it from H<sub>2</sub>O<sup>+</sup> (Fuselier et al. 2016; Beth et al. 2017, see also Fig. 10).

Ion-neutral chemistry affects ion composition but, as there is no net production of charge, the total ion and electron number densities remain unchanged. Only one known process affects the electron density, reduces the net amount of charges, and efficiently removes ions and electrons from a plasma. It is the so-called:

- **electron-ion dissociative recombination (DR)**: a molecular ion recombines with an electron, which yields fragmented neutral species. For example



“Dissociative” refers to the breaking of the molecular ion into neutral fragments in order to dissipate the exceeding energy. The temperature-dependent loss rate for the DR reaction is given by:

$$L_{\text{DR},s}(T_e) = \alpha_s(T_e) n_s n_e \quad (28)$$

where  $\alpha_s$  stands for the DR reaction rate coefficient (a function of the electron temperature  $T_e$ ),  $n_s$  for the number density of ion species  $s$ , and  $n_e$  for the electron number density ( $n_e \approx \sum_s n_s$ ).

Some words of caution regarding the DR reaction. Firstly, it depends on (i) the electron temperature (the colder the electrons are, the more efficient the DR is), and (ii) the molecular ion species (Heritier et al. 2017). In fact,  $\alpha_s(T_e)$

exhibits very different  $T_e$ -dependency.  $\alpha_s(T_e)$  is often assumed to behave like  $\alpha_s(T_e) \propto 1/\sqrt{T_e}$  as theoretically derived (Wigner 1948), an approximation that works well with many ion species (Florescu-Mitchell and Mitchell 2006). In reality, this dependency might only hold for a specific electron temperature range whether the molecular ions are diatomic or polyatomic (McGowan and Mitchell 1984). For instance,  $\alpha_{\text{H}_2\text{O}^+} = 4.3 \times (300/T_e)^{0.74} \times 10^{-13} [\text{m}^3 \text{s}^{-1}]$  (Rosén et al. 2000) for  $T_e < 1000$  K and  $\alpha_{\text{CO}_2^+} = 4.2 \times (300/T_e)^{0.75} \times 10^{-13} [\text{m}^3 \text{s}^{-1}]$  (Viggiano et al. 2005) without constraints on  $T_e$ , where  $T_e$  is expressed in K. Nevertheless, these recombination rates are of the same order of magnitude for similar  $T_e \lesssim 10^3$  K so that assuming initially a common value is reasonable. When the range of  $T_e$  encountered at comets is considered,  $\alpha_s$  may span over several orders of magnitude (see Section 2.4.1).

Secondly, DR introduces non-linearity into the continuity equation. For ion-neutral chemistry in the inner coma, one may safely assume that the neutral density profile  $n_p$  is decreasing as  $1/r^2$  (see Eq. 2). DR introduces non-linear terms, such as  $n_s^2$  and  $n_s n_e$ . Last but not least,  $\alpha_s$  is often greater than the coefficient rate  $k$  associated with ion-neutral chemistry. Despite ions being much less abundant than neutrals in the inner part of the coma by a factor  $\sim \nu^{\text{ioni}} r/V_n$  (see Eqs. 2 and 42),  $\nu^{h\nu,\text{ioni}}$  (a main contributor of ionisation for  $r_h < 2$  au) increases as the comet gets closer to the Sun and the gap reduces. In addition, as the activity rises, collisions occur more frequently, cooling the electrons: The electron temperature decreases, the loss through DR increases, and potentially overcoming the loss through transport (see Section 2.4.1). This appears to be the case for outgassing rates  $\gtrsim 10^{28} \text{ s}^{-1}$  (Heritier et al. 2018; Beth et al. 2019).

## 2.4. The Ionosphere: Putting it all together

### 2.4.1. Total ionospheric density

As shown in Section 2.1, one has to solve a complex system made of  $s'$  continuity equations, one for each ion species  $s$ , in order to model the cometary ion composition under steady-state conditions. This can be summarised by combining Eqs. 26, 27, and 28 for the chemical reactions, as follows:

	transport	ionisation	ion-neutral chemistry	electron-ion recombination	
s' eqs. {	$\nabla \cdot (n_{A^+} \mathbf{V}_{A^+})$	$= \nu_{A^+}^{\text{ioni}} n_n$	$-\cancel{k_{A^+,B} n_{A^+} n_B} \pm \dots$	$-\alpha_{A^+} n_i n_{A^+}$	(29)
	+ $\nabla \cdot (n_{B^+} \mathbf{V}_{B^+})$	$= \nu_{B^+}^{\text{ioni}} n_n$	$+\cancel{k_{A^+,B} n_{A^+} n_B} \pm \dots$	$-\alpha_{B^+} n_i n_{B^+}$	
	$\vdots$	$\vdots$			
sum	$\nabla \cdot (n_i \mathbf{V}_i)$	$= \nu_i^{\text{ioni}} n_n$	+0	$-\left(\sum_{s=1}^{s'} \alpha_s n_s\right) n_i$	

where

$$\mathbf{V}_i = \sum_s n_s \mathbf{V}_s / n_i \quad (30)$$

$$\nu_s^{\text{ioni}} = \sum_p n_p (\nu_{p,s}^{h\nu,\text{ioni}} + \nu_{p,s}^{e-,\text{ioni}}) / n_n \quad (31)$$

$$\nu_i^{\text{ioni}} = \sum_s \nu_s^{\text{ioni}} \quad (32)$$

$n_n$  stands for the total neutral density,  $n_i$  for the total ion number density (equal to the electron density, assuming no doubly-charged ions),  $\mathbf{V}_i$  for the mean ion velocity,  $\nu_i^{\text{ioni}}$  for a mean/effective ionisation rate (via photoionisation, see Section 2.2.1, and electron impact, see Section 2.2.2), and  $\alpha_s$  for the electron-ion dissociative recombination rate coefficient associated with ion species  $s$ . Indices  $p$  and  $s$  refer to a specific neutral and a specific ion species, respectively. Note that in Eq. 31, only photoionisation and electron-impact ionisation terms are included, as solar wind ionisation and charge-exchange terms are usually negligible in the inner coma (see Sections 2.2, 2.2.3, and 2.2.4).

Once all ion continuity equations are summed, the ion-neutral chemistry terms (second set of terms on the right-hand side of Eq. 29) cancel out between lost and produced ion species. From Eq. 29, the continuity equation ruling the total ion number density is weakly depending on the ion composition through the last term on the right-hand side (electron-ion recombination) as the kinetic rates are different between ion species (see Section 2.3).

Let us look more closely at the transport term (left-hand side of Eq. 29). Its contribution in non-cometary environments, such as a planetary ionosphere in the plane-parallel approximation (Schunk and Nagy 2009), is limited: Vertical transport between atmospheric layers remains small and is dominated by eddy or molecular diffusion. In contrast, at comets, the neutrals, and therefore the newly-born ions, are moving at speeds  $V_n$  ranging from 300 m s<sup>-1</sup> close to the surface, up to 1 km s<sup>-1</sup> farther away, assuming adiabatic expansion. The radial velocity thus plays a significant role at comets. In spherical symmetry and under steady-state conditions, physical quantities depend only on the cometocentric distance  $r$  and the bulk cometary ion velocity  $V_i(r)$  being mainly radial, although these assumptions are only valid for the inner cometary ionosphere and may significantly break at larger cometocentric distances (see the chapter by Götz et al. in this volume). Under such conditions, the transport term is reduced to:

$$\nabla \cdot (n_i \mathbf{V}_i) = \frac{1}{r^2} \frac{d(n_i V_i r^2)}{dr} = V_i \frac{dn_i}{dr} + n_i \frac{dV_i}{dr} + \frac{2n_i V_i}{r} \quad (33)$$

The spherical shell enclosed in  $[r, r + dr]$  has a volume  $4\pi r^2 dr$  such that ions move into shells of increasingly larger volumes the more outwards they move. The last term  $2n_i V_i / r$  in Eq. 33 accounts for this geometrical effect.

As a whole, Eq. 29 represents the balance between the source of the ionospheric plasma through ionisation of the cometary neutrals and ionospheric loss terms, namely

radial transport and electron-ion dissociative recombination (net chemical loss). Unfortunately, it is not possible to solve Eq 29 analytically or without making assumptions/approximations as one needs the radial ion velocity and electron temperature profiles.

Before going further, the first question should be: Which of these terms are the most relevant to consider and are there any that can be neglected? One approach is to look at a typical physical quantity characterising each term. If Eq. 29, combined with Eq. 33, is now divided by  $n_i$ :

$$-\underbrace{\frac{1}{n_i r^2} \frac{d(n_i V_i r^2)}{dr}}_{1/\mathcal{T}_{\text{transport}}} + \underbrace{\frac{\nu_i^{\text{ioni}} n_n}{n_i}}_{1/\mathcal{T}_{\text{ionisation}}} - \underbrace{\sum_s \alpha_s n_s}_{1/\mathcal{T}_{\text{recombination}}} \approx 0 \quad (34)$$

an equation whose dimension is the inverse of time. Large (resp. small) terms in Eq. 34 are associated with fast (resp. slow) processes, that is, short (resp. long) timescales.

Let us review each loss term first (terms with negative signs in Eq. 34 which represent a physical sink), that is, transport and dissociative recombination, and assess their respective timescale. The transport timescale is given by:

$$\frac{1}{\mathcal{T}_{\text{transport}}} = V_i \frac{d \log n_i}{dr} + \frac{dV_i}{dr} + \frac{2V_i}{r} \quad (35)$$

independent of the cometary activity. From observations, the plasma density in the inner cometary ionosphere of 1P and 67P alike varies in  $1/r$  (Balsiger et al. 1986; Edberg et al. 2015; Heritier et al. 2017) such that  $d \log n_i / dr \sim -1/r$ . Regarding the variation of the radial speed, there is no evidence of a strong velocity gradient (acceleration or deceleration) except near the contact surface at 1P (Goldstein et al. 1989). However, within the diamagnetic cavity of 1P, the ion velocity was relatively constant (Schwenn et al. 1987). At 67P, there is no evidence of strong velocity gradients either. This term can thus be neglected and we end up with:

$$\frac{1}{\mathcal{T}_{\text{transport}}} \sim \frac{V_i}{r} \text{ or } \frac{V_n}{r} \quad (36)$$

In fact, Eq. 36 is an approximation which only holds beyond a few cometary radii, beyond the location where the plasma density peaks, where  $n_i \propto 1/r$ . Below and up to the location of this maximum, this is an underestimate and Eq. 35 must be used (see Fig. 7).

By comparison, the electron-ion recombination timescale for the whole plasma population (electron sink term) is given by:

$$\frac{1}{\mathcal{T}_{\text{recombination}}} \approx \alpha_i(T_e) n_i(r) \sim \frac{\alpha_i(T_e) n_{i,\text{obs}} r_{\text{obs}}}{r} \quad (37)$$

where:

$$\alpha_i = \frac{\sum_s \alpha_s n_s}{n_i}$$

and the subscript ‘obs’ corresponds to a location of reference where the cometocentric distance and number plasma

density are known, for instance, probed and observed at a spacecraft. The numerator in Eq. 37 has the dimension of a speed and should be compared with the ion speed. The recombination timescale may span over several orders of magnitude because it depends both on electron temperature (through the recombination coefficient  $\alpha_i$ , see Section 2.3) and plasma density.

Experimentally,  $\alpha_i$  ranges between  $10^{-12}$  and  $10^{-15}$   $\text{m}^3 \text{s}^{-1}$  for  $10^2 < T_e < 10^4$  K (Gombosi *et al.* 1996; Rosén *et al.* 2000). The electron temperature may be very different throughout the coma or even between comets. The lowest range for  $T_e$  typically corresponds to the inner cometary ionosphere at 1P under active outgassing conditions. As further discussed in Section 3.1.2, frequent electron-neutral collisions are expected to bring the electron temperature close to the nucleus down to that of the neutral gas, which is consistent with indirect observations at comet 1P (see Eberhardt and Krankowsky 1995). The highest range has been observed at 67P under low outgassing conditions when the bulk of the thermal population is not thermalised (Wattiaux *et al.* 2019, 2020), see Section 3.1.1). During Giotto’s flyby, ion number densities reached almost  $10^{10} \text{ m}^{-3}$  at  $r_{\text{obs}} \sim 10^4$  km (Altwegg *et al.* 1993) such that  $n_{i,\text{obs}} r_{\text{obs}} \approx 10^{17} \text{ m}^{-2}$ . Because  $\alpha_i \sim 10^{-14} \text{ m}^3 \text{ s}^{-1}$  in those conditions, the dissociative recombination timescale was  $\mathcal{T}_{\text{recombination}} \sim 10^4$  s (or  $\sim 2$  h 45 min, Gombosi *et al.* 1996). Compared with the transport timescale of about  $r/V_i \sim 10^4$  s at the same location, transport and dissociative recombination were contributing equally to the ion sink at that location at 1P (Beth *et al.* 2019). However, for  $r \lesssim 10^4$  km,  $T_e$  fell drastically by 2–3 orders of magnitude: The recombination timescale was then shorter than the transport timescale and hence dissociative recombination was the main ion sink in the innermost of 1P’s ionosphere.

Unlike the transport timescale, the recombination timescale depends on cometary activity: The higher the outgassing activity, the larger the ion number density, the more efficient the recombination. We can then try to find out for which activity we should consider/neglect the recombination. Let us consider a very simplistic case in the coma, with a uniform electron temperature and therefore a constant  $\alpha_i$ . Under steady-state conditions and spherical symmetry, the ionospheric continuity equation (Eq. 29), combined with Eqs. 2 and 33, reduces to:

$$\frac{1}{r^2} \frac{d(n_i V_i r^2)}{dr} = \frac{\nu_i^{\text{ioni}} Q}{4\pi V_n r^2} - \alpha_i n_i^2 \quad (38)$$

where  $Q$  is the total outgassing rate for the comet (all major neutral species included). Assuming constant and radial ion speed  $V_i$ , ionisation frequency  $\nu_i^{\text{ioni}}$ , and recombination rate coefficient  $\alpha_i$  to be independent of  $r$ , the solution of Eq. 38 is given by (Beth *et al.* 2019):

$$n_i(r) = \frac{V_i}{2\alpha_i r} (\delta - 1) \frac{r^\delta - r_c^\delta}{r^\delta + \frac{\delta - 1}{\delta + 1} r_c^\delta} \quad (39)$$

where:

$$\delta = \sqrt{1 + \frac{Q}{Q_0}}, \quad Q_0 = \frac{\pi V_n V_i^2}{\nu_i^{\text{ioni}} \alpha_i},$$

and  $r_c$  is the nucleus’ radius.  $Q_0$  is homogeneous to an outgassing rate [ $\text{s}^{-1}$ ]. The different timescales (namely transport, recombination, and ionisation) associated with this profile are given for illustration in Fig. 7. Even though ion-neutral chemical reactions do not affect the total ion density, their typical timescale (varying in  $\propto r^2$ ) is indicated.

Regarding the assessment of  $Q_0$ , and unlike  $\alpha_i$ , the order of magnitude for  $\nu_i^{\text{ioni}}$ ,  $V_n$ , and  $V_i^2$  can be reasonably estimated (resp. see Section 2, the chapter by Biver *et al.* in this volume, and Section 4). In the case of active comets,  $\nu_i^{\text{ioni}}$  is not uniform (even when assuming spherical symmetry for the neutral density) and can be significantly reduced closer to the nucleus in the inner coma due to photoabsorption (see Section 2.2.1). This has also the consequence of limiting the effect of recombination near the nucleus (Beth *et al.* 2019): As the ion number density is near zero at the nucleus’ surface, the recombination is negligible there.

Interestingly, Eq. 38 gives a constraint on the flux. By integrating Eq. 38 over radial distance  $r$ , one gets:

$$n_i(r) V_i(r) \leq \frac{1}{r^2} \int_{r_c}^r \frac{\nu_i^{\text{ioni}} Q}{4\pi V_n} dr = \frac{\nu_i^{\text{ioni}} Q}{4\pi V_n} \frac{r - r_c}{r^2} < \frac{\nu_i^{\text{ioni}} Q}{4\pi V_n r} \quad (40)$$

Equation 40 may be used in two ways:

- If the ion number density is known based on in situ observations, it provides an upper limit for the ion radial velocity.
- When recombination is negligible compared to transport, Eq. 40 reduces to the equality (see Eq. 38):

$$n_i(r) V_i(r) = \frac{\nu_i^{\text{ioni}} Q}{4\pi V_n} \frac{r - r_c}{r^2} \quad (41)$$

This corresponds to a solution to the ion continuity equation reduced to the simple balance between transport (loss) and ionisation (source). In contrast with Eq. 39, Eq. 41 is valid for  $V_i(r)$  varying with  $r$  but still purely radial.

For weakly active comets, such as 67P, the recombination timescale is much longer than the transport timescale (Galand *et al.* 2016). This corresponds to the ‘equality’ case given by Eq. 41. Applying Eq. 2, Eq. 41 can be rewritten as:

$$n_i(r) = \frac{\nu_i^{\text{ioni}} n_n (r - r_c)}{V_i(r)} \quad (42)$$

This equation was successfully used at 67P at low activity to retrieve the electron number density observed by the Mutual Impedance Probe and Langmuir Probe (see Section 3.1.1) onboard Rosetta (Galand *et al.* 2016; Heritier *et al.* 2018).

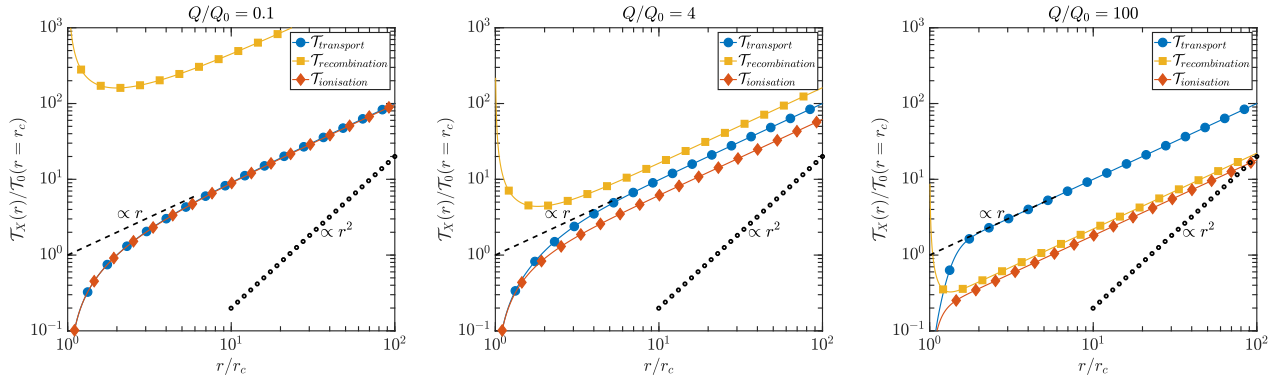


Fig. 7.— Timescales for the ion number density profile from Eq. 39 for different activities normalised to  $Q_0$ :  $Q/Q_0 = 0.1$  (left, loss dominated by transport),  $Q/Q_0 = 4$  (middle, losses through transport and recombination are similar), and  $Q/Q_0 = 100$  (right, loss dominated by recombination) as a function of cometocentric distances normalised to  $r_c$  and expressed in terms of the approximated transport timescale  $\mathcal{T}_0$  at the nucleus’ surface (Eq. 36). Timescale dependencies in  $r$  and  $r^2$  (losses in  $1/r$  and  $1/r^2$ ) are indicated for reference. Photoabsorption is ignored for simplicity.

A multi-instrument approach was applied to cometocentric distances from 10 km to 80 km, for heliocentric distances larger than 2 au. In those conditions, photoabsorption and dissociative recombination were negligible (*Heritier et al.* 2018). The ions were assumed not to have undergone any significant acceleration at Rosetta’s position and to have a bulk velocity similar to that of the neutrals ( $V_i(r) \approx V_n$  at  $r = r_{\text{Rosetta}}$ ). Electron-impact ionisation frequency was derived from the electron spectrometer onboard Rosetta (see Section 3.1.3), whereas photoionisation frequency was extrapolated from solar flux measurements from Earth. Neutral density and neutral composition were derived from Rosetta pressure gauge and double-focusing mass spectrometer (*Balsiger et al.* 2007, see the chapter by Biver et al. in this volume). Equation 42 captured very well the observed electron density from the balance between transport of non-accelerated ions and the major sources of ionisation, photoionisation and electron-impact ionisation. The latter source was found to dominate at times, especially post-perihelion for large heliocentric distances ( $> 2$  au, see *Heritier et al.* 2018). Eq. 42 held even under solar-wind disturbed conditions, such as CMEs and CIRs (*Galand et al.* 2016; *Heritier et al.* 2018).

This multi-instrument approach was also applied all the way down to the surface at the end of the Rosetta mission (*Heritier et al.* 2017). In that case, the model was refined by taking into account adiabatic expansion and acceleration of the cometary neutrals following sublimation near the surface (*Huebner and Markiewicz* 2000). Excellent agreement was found between observed and modelled ionospheric densities, as shown in Fig. 8. The only exception was around 3 UTC near the neck of the comet which had a concave shape and which is a region where the local outgassing has a complex structure and the gas may be collimated (see the chapter by Marschall et al. in this volume).

#### 2.4.2. A rich diversity of ions: a real ion zoo

After the focus on the total ionospheric density (Section 2.4.1), let us now have a look at the ion composition in the coma. We consider here individual ion species, whose number density is governed by the continuity equation given in Eq. 5. In terms of loss, three processes are in competition depending on the outgassing activity: transport, ion-neutral collisions, and electron-ion dissociative recombination (Sections 2.3 and 2.4.1). Note that the recombination timescale for ion species  $s$  is simply given by  $\mathcal{T}_{s,\text{recombination}} \approx (\alpha_s n_i(r))^{-1}$  (Eqs. 34 and 37). Because it involves the electron density (or total ion density,  $n_i$ ), it is almost the same for the different ion species. A given ion species also undergoes loss through ion-neutral collisions (see Section 2.3 and Eq. 5). The loss timescale for an ion species  $s$  through ion-neutral collisions is given by:

$$\frac{1}{\mathcal{T}_{s,\text{ion-neut loss}}} = \sum_p k_{s,p}(T) n_p(r) = k_{s,n} n_n(r) \propto \frac{1}{r^2} \quad (43)$$

where

$$k_{s,n} = \frac{1}{n_n} \sum_p k_{s,p} n_p(r) \quad (44)$$

is the average reaction rate coefficient between ion species  $s$  and the set of neutral species  $n$ . The subscript  $p$  refers to the neutral species  $p$  and is incremented over all neutral species chemically reacting with ion species  $s$ . Excluding extended sources, the neutral density of a neutral species follow a spatial dependence in  $1/r^2$  (Eq. 2), thus the timescale  $\mathcal{T}_{s,\text{ion-neut loss}}$  varies in  $r^2$ , whereas dissociative recombination and transport timescales vary in  $r$  (see Fig. 7). Therefore, the loss timescale through ion-neutral chemistry increases much faster with cometocentric distance  $r$  than that through transport or recombination. The ion-neutral chemistry and coupling are relevant in the region where

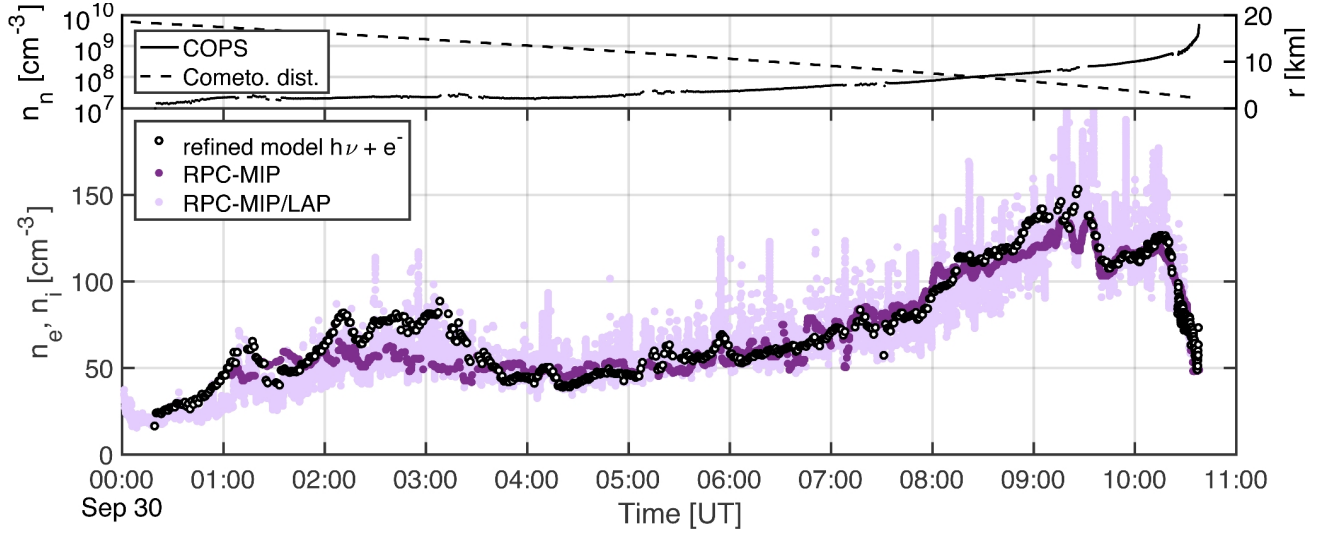


Fig. 8.— Top panel: Time series of neutral number density from ROSINA pressure gauge (solid line) and of cometocentric distance (dashed line). Bottom panel: Time series of the modelled (black dots) and observed (magenta) ionospheric number densities at the end of Rosetta’s mission, from 20 km down to the surface on 30 September 2016. The outgassing rate was around  $4 \times 10^{25} \text{ s}^{-1}$ . The dark magenta dots correspond to RPC Mutual Impedance Probe measured electron density, while the light magenta dots represent the high time resolution RPC Langmuir Probe data cross-calibrated with RPC Mutual Impedance Probe. (Fig. 9 from *Heritier et al. 2017*)

$\mathcal{T}_{s,\text{ion-neut loss}} \leq \mathcal{T}_{\text{transport}}$  (*Gombosi 2015*), that is, within a region around the nucleus bounded by:

$$R_{s,n} = \frac{k_{s,n} Q}{4\pi V_s V_n} \lesssim \frac{k_{s,n} Q}{4\pi V_n^2} \quad (45)$$

where the distance  $R_{s,n}$  corresponds to  $\mathcal{T}_{\text{transport}}$  (combining Eqs. 2, 36, and 43). Ions and neutrals are assumed to flow radially outward at the same speed (see Sections 2.4.1 and 4.1). However, recombination may shrink this region of coupling (i.e. reduce  $R_{s,n}$ ) if  $\mathcal{T}_{\text{recombination}} \leq \mathcal{T}_{\text{transport}}$ .

Ion species can be separated into three broad categories whose  $r$ -dependency of their number density is summarised in Table 1 and exemplified in Fig. 9:

- (A) Ions produced from ionisation but not (or barely) reacting with neutrals, that is,  $R_{s,n} < r_c$  even for high outgassing activity (see Eq. 47),
- (B) Ions produced from ionisation and which are able to react efficiently with the main neutral cometary species for high enough outgassing activity ( $r_c < R_{s,n}$ ),
- (C) Ions only produced through ion-neutral chemistry, such as protonated molecules (except  $\text{H}_2\text{O}^+$ ), and lost through mainly transport or chemistry (Section 2.3). They are born from collisions between neutrals and ions from category (B).

When  $R_{s,n} \lesssim r_c \leq r$ , ions from category A and ions from category B for weak outgassing activity are mainly produced through ionisation and are primarily lost through

transport, which implies:

$$\frac{1}{r^2} \frac{d(n_s V_s r^2)}{dr} \approx \nu_s^{\text{ioni}} n_n(r) \quad (46)$$

Applying Eq. 2 leads to:

$$n_s(r) \approx \frac{\nu_s^{\text{ioni}} Q}{4\pi V_n V_s(r)} \frac{r - r_c}{r^2} \approx \frac{\nu_s^{\text{ioni}} (r - r_c)}{V_s(r)} n_n(r) \quad (47)$$

When  $R_{s,n} > r_c$  (moderate to high activity), for  $r_c \lesssim r \lesssim R_{s,n}$ , ion species  $s$  from category B, produced through ionisation, is lost primarily through ion-neutral chemistry (note that usually such an ion species is not terminal and hence not lost through electron-ion dissociative recombination); it is said to be in *photochemical equilibrium*, meaning that the ion number density is only governed by chemical reactions:

$$0 \approx \nu_s^{\text{ioni}} n_n(r) - k_{s,n} n_n(r) n_s(r) \quad (48)$$

This implies that:

$$n_s(r) \approx \frac{\nu_s^{\text{ioni}}}{k_{s,n}} \approx \text{constant} \quad (49)$$

This value is a plateau and an upper limit for the ion species  $s$  which cannot be surpassed. In addition, photoabsorption may reduce this value in an optically thick coma (see Section 2.2.1).

Ions from category C, so-called *protonated ions* are produced through proton-transfer reactions, either from  $\text{H}_2\text{O}^+$  or through the production of other protonated ions, such as  $\text{H}_3\text{O}^+$ . Neglecting dissociative recombination in Eq. 29, the



total ion density of protonated molecules  $AH^+$  (i.e. the sum of the number densities of the protonated molecules such that  $n_{AH^+} = n_{H_3O^+} + n_{NH_4^+} + \text{etc.}$ ) obeys approximately the equation:

$$\frac{1}{r^2} \frac{d(n_{AH^+} V_{AH^+} r^2)}{dr} \approx k_{H_2O^+,A} n_A n_{H_2O^+} \quad (50)$$

The loss through dissociative recombination did not play a key role to assess ion densities at the location of Rosetta during its escort phase (*Heritier et al.* 2018), hence this process was disregarded in Eq. 50. However, in specific conditions, such as high enough outgassing rates at a certain range of cometocentric distances coupled with a high sensitivity of the recombination rate coefficient  $\alpha_i$  with  $T_e$ , dissociative recombination may represent a key loss for protonated ions: This was for example the case during Giotto's flyby of 1P (*Rubin et al.* 2009).

To solve Eq. (50), one needs to know the dependence of  $n_{H_2O^+}$  with  $r$  as it plays the role of precursor for the formation of protonated molecules (see e.g. *Aikin* 1974). Indeed, the protonated molecules dominate the ion composition near the nucleus only when  $H_2O^+$  is close to photochemical equilibrium and triggers the formation of  $H_3O^+$  (see e.g. Fig. 9). On the one hand, in the region  $r_c \lesssim r \lesssim R_{H_2O^+,n}$  occurring only for high enough outgassing rates,  $H_2O^+$  is in photochemical equilibrium and thus the left-hand side of Eq. 50 is  $\propto 1/r^2$ . Therefore, we have:

$$n_{AH^+}(r) \propto \frac{r - r_c}{r^2} \text{ for } r \lesssim R_{H_2O^+,n} \quad (51)$$

On the other hand, for  $r > R_{H_2O^+,n}$ ,  $H_2O^+$  dominates again the ion composition and behaves  $\propto 1/r$ . The right hand side of Eq. 50 is  $\propto 1/r^3$  and thus:

$$n_{AH^+}(r) \propto \frac{\log r}{r^2} \text{ for } r \gtrsim R_{H_2O^+,n} \quad (52)$$

At low activity ( $Q \leq 10^{25} \text{ s}^{-1}$ ), ion species from category B exhibit an ion density profile (blue, solid line) similar to that of ions from category A (black, dashed line) and given by Eq. 47, as shown in the left panels in Fig. 9. Ions from B, although reacting with  $H_2O$  and  $CO_2$  like  $H_2O^+$ , have their associated ion-neutral coupling limit  $R_{B,n}$  smaller than  $r_c$  due to the low outgassing rate. So effectively, they behave as ions from category A. Ions from category C are hence barely produced as they require at least one ion-neutral collision and their density decreases very quickly with increasing  $r$  (see red profile, left panels, Fig. 9). A and B-type ion species are dominating the ion composition.

As the outgassing activity increases ( $Q \gtrsim 10^{25} \text{ s}^{-1}$ ), so does the number density of the neutral species (e.g.  $H_2O$  and  $CO_2$ ), and  $R_{B,n}$  passes above the surface ( $R_{B,n} > r_c$ ) meaning there exists a region where ion-neutral chemistry dominates over transport. Within this region, ions from category B are efficiently reacting with neutrals and their density profile is near photochemical equilibrium (Eq. 49,

Table 1: Different radial number density dependency for each category below and above the ion-neutral coupling limit  $R_{s,n}$  (Eq. 45) when transport dominates the ion loss ( $Q/Q_0 \lesssim 1$ ). The  $r$ -dependencies given are for an optically thin coma. \*For category A,  $R_{s,n} < r_c$ , so third column refers to  $r_c < r$ . †For category C,  $s$  in  $R_{s,n}$  is not associated with the ion itself but to its parent ion, for example,  $s = H_2O^+$  and  $n = H_2O$  for  $H_3O^+$  and  $s = H_2O^+/H_3O^+$  and  $n = NH_3$  for  $NH_4^+$ . For category C, transport is here assumed to be the ion loss process.

Cat.	Ion density $n_s$ when:		Ref. Eqs.
	$r_c < r < R_{s,n}$	$r_c < R_{s,n} < r$	
A	N/A ( $R_{s,n} \ll r_c$ )	$\propto \frac{r - r_c^*}{r^2}$	47
B	$\approx \text{constant} \leq \frac{\nu}{k}$	$\propto \frac{1}{r}$	47, 49
C†	$\propto \frac{r - r_c}{r^2}$	$\propto \frac{\log r}{r^2}$	51, 52
A+B+C	$\propto \frac{r - r_c}{r^2}$	$\propto \frac{r - r_c}{r^2}$	–

see blue profile, middle and right panels in Fig. 9). In the same region, ions from category C are efficiently produced, such as  $H_3O^+$  (and  $NH_4^+$ ), and may dominate the composition region with a profile following the red, solid line, middle and right panels, in Fig. 9. Beyond  $R_{B,n}$ , transport or electron-ion recombination govern the loss. Ions from B (resp C) are barely lost (resp. produced) through ion-neutral collisions. A-type and C-type ions are dominating the ion composition at low  $r$  distances, whereas A-type and B-type ions are dominating at high  $r$ .

Regarding the detection of ion species in a cometary environment, Rosetta has revolutionised the field (*Beth et al.* 2020). If the mass resolution of the ion mass spectrometer onboard a cometary probe is high enough, the mass, or mass-per-charge, may work as a unique identifier of ion species. For example, the mass of  $H_2O^+$  is 18.015 u while that of  $NH_4^+$  is 18.039 u. We thus need an instrument with a minimum resolving power of  $\Delta m \approx 0.025$  u to separate both species. During the Giotto flyby of comet 1P, a snapshot of the ion density profiles was obtained at different integer masses (*Altwegg et al.* 1993); ion species of the same integer mass could however not be distinguished due to the too low mass resolution of the ion mass spectrometer. In contrast, at comet 67P, ion species were identified individually over a two-year period and a wide range of outgassing activities thanks to the ROSINA double-focusing mass spectrometer (DFMS) aboard Rosetta (see Fig. 10-top). This spectrometer was one of the most powerful spectrometers ever flown on a planetary probe in terms of mass resolution, reaching up to  $R \approx 3000$ . Thanks to its high accuracy, more than 20 ion species were unambiguously identified in comet 67P's ionosphere (*Beth et al.* 2020, see

Fig. 10-centre and Fig. 10-bottom), with the serendipitous detection of the  $\text{CO}_2^{++}$  dication.

### 3. Electron population and its impact

#### 3.1. Different electron populations

At any given time, the electrons in a cometary environment can be classified into three broad populations: *cold*, *warm*, and *hot*. Although the energy range of each population may slightly vary between published studies, this classification allows to distinguish different electron sources and processes affecting electrons. The cold and warm electron populations, which are primarily of cometary origin with some contribution from the solar wind to the warm electrons, as discussed below, represent a dense population, compared with the rarefied hot electron population. Note that, while cold and warm populations cohabit, one of them may be greatly dominating over the other, depending on the outgassing activity, neutral composition, and cometocentric distance. These three electron populations were first reported from in situ observations at around 12000 km of comet 21P during its flyby by ICE (Zwickl *et al.* 1986). During the course of the Rosetta escort mission, these three populations were also identified. They were differentiated by their signatures as detected by different Rosetta Plasma Consortium (RPC, Glassmeier *et al.* 2007) sensors onboard Rosetta. The characteristics, prime origin (photoelectrons, Section 2.2.1, solar wind electrons, or their secondaries, Section 2.2.2), and detection of each of the three electron populations are discussed in more details hereafter:

- the newly-born, warm, cometary electrons (5-15 eV), which dominate the plasma density at large heliocentric distances, but are always present (Section 3.1.1). They include photoelectrons (for coma optically thin to EUV radiation) and electrons from electron-impact ionisation by hot electrons.
- the cold, cometary electrons ( $< 1$  eV), which are energy-degraded warm electrons and whose relative importance increases with outgassing activity (Section 3.1.2),
- the more rarefied, hot electrons ( $> 20$  eV). When the coma is optically thin to EUV at large heliocentric distances, they are mainly accelerated, solar wind electrons, and are responsible for the bulk ionisation of the neutral coma and for the auroral FUV emissions (Section 3.1.3). When the coma is optically thick (e.g. during the flyby of 1P by Giotto), they are mainly photoelectrons in the inner coma (Bhardwaj 2003; Beth *et al.* 2019).

##### 3.1.1. Newly-born warm, cometary electrons

The warm electron population refers to electrons produced through (i) photoionisation in an optically thin coma (see Section 2.2.1) and (ii) electron-impact ionisation (see Section 2.2.2). Photoionisation of a neutral species  $p$  by

solar radiation of incident energy  $E_{h\nu}$  above ionisation energy  $E_{p,s}^{th}$  yields the production of a photoelectron and an ion (see Eq. 6). The rate at which neutrals  $p$  are ionised per unit time is given by the photoionisation frequency,  $\nu_p^{h\nu,ioni}$  (see Eq. 12 and Fig. 4). The total photoelectron production rate,  $S_{e^-}^{h\nu}$ , depends on the neutral composition and total neutral density (Eq. 16). During photoionisation of a neutral  $p$  yielding the production of a photoelectron and an ion  $s$ , the excess energy,  $\Delta E = E_{h\nu} - E_{p,s}^{th}$ , goes mainly to the released photoelectron, in the form of kinetic energy. However, as this process is largely isotropic, the electrons are uniformly scattered in every direction. The energy distribution of the produced photoelectrons is as structured as the incident solar radiation flux, some strong solar lines producing a peak of photoelectrons at a given energy, like at 27–28 eV (photoionisation of  $\text{H}_2\text{O}$  or  $\text{CO}_2$  by the HeII 30.4 nm (40.8 eV) solar line, Körömezey *et al.* 1987; Bhardwaj 2003; Vigren and Galand 2013). Nevertheless, in an optically thin coma, the average photoelectron energy is around 10–15 eV (Huebner *et al.* 1992). These electrons are referred to as *warm*, prior to efficient cooling in the coma through collisions (see Section 3.1.2). In an optically thick coma, the mean photoelectron energy increases in regions of large neutral column densities (Bhardwaj 2003). Indeed, as illustrated in Fig. 3, photoabsorption cross sections have the largest values above 20 nm. Hence it is this part of the solar spectrum which is going to be absorbed first, at an optical depth  $\tau = 2$  (Eq. 17). Inward of the boundary corresponding to  $\tau = 2$  at 20 nm, photoelectrons are produced by the remaining solar photons of wavelength less than 20 nm (energy larger than  $\sim 60$  eV). Subtracting the ionisation energy (typically 10–15 eV), this means that all photoelectrons in this region are born with an energy larger than 45 eV. In such a case, photoelectrons are *hot*, no longer warm.

Electrons themselves can be energetic enough to ionise the neutral species. This is the case if their energy is above the ionisation energy (see Section 2.2.2). As energetic electrons at 67P were found to have typical energies of 30–40 eV (Myllys *et al.* 2019), the energy of the secondary electron produced through ionisation is less than 15 eV, because the primary electron retains at least half of the remaining energy (where the remaining energy corresponds to the primary electron original energy minus the ionisation energy). Thus, electrons produced by electron-impact ionisation also contribute to the warm population.

The warm electron population was detected throughout the Rosetta escort phase by several instruments. Firstly, the Ion and Electron Sensor (IES, Burch *et al.* 2007), part of the RPC consortium, measured energy distributions of negatively-charged particles (primarily electrons) above the noise level over an energy range from 4.3 eV  $\text{q}^{-1}$  to a few 100 eV  $\text{q}^{-1}$  with an energy resolution  $\Delta E/E \sim 8\%$ . The electron velocity/energy distribution, fitted by a suprathermal double-kappa function, exhibited signatures from two populations: one warm and one hot (Broiles *et al.* 2016b;

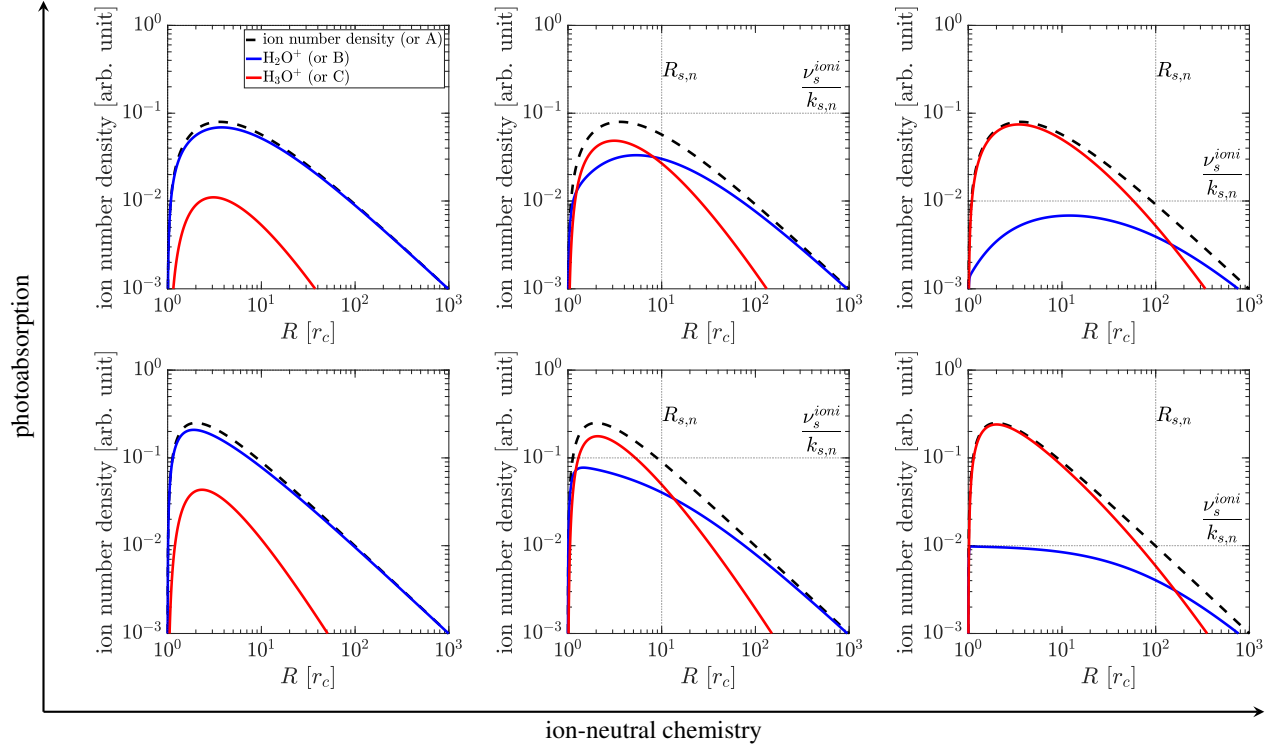


Fig. 9.— Total ion number density profile (dashed, representative of the category as well) and those of  $\text{H}_2\text{O}^+$  (blue, representative of category B) and  $\text{H}_3\text{O}^+$  (red, representative of category C) for a coma made of  $\text{H}_2\text{O}$  only, in arbitrary unit using the analytical model from *Beth et al. (2020)*. Electron-ion dissociative recombination is ignored. Although photoabsorption and ion-neutral chemistry are both linked to the outgassing rate, different conditions are achieved by increasing either photoabsorption (from bottom to top) or ion-neutral chemistry (from left to right) separately. The  $\text{H}_2\text{O}^+$  number density at photochemical equilibrium (Eq. 49, horizontal dotted line) and the ion-neutral coupling limit (Eq. 45 vertical dotted line) are indicated.

*Myllys et al. 2019*). Whereas the hot population was rarefied (see Section 3.1.3), the warm population was dense ( $\sim 10\text{--}200\text{ cm}^{-3}$ ) with temperatures typically below 10 eV (*Myllys et al. 2019*). At the beginning of Rosetta’s mission, on 14 November 2014, *Broiles et al. (2016a)* identified two dense populations in the RPC-IES dataset: One with temperatures above 8.6 eV was observed when the local neutral number density at Rosetta was high ( $n_n > 8 \times 10^6\text{ cm}^{-3}$ ) and one with temperature below 8.6 eV when  $n_n$  was generally low ( $n_n < 8 \times 10^6\text{ cm}^{-3}$ ). *Myllys et al. (2019)* did not find that the electron temperature of the warm population  $T_w$  decreased with heliocentric distance but the spread in electron temperature estimates was found to range from 1 eV to 15 eV. It should be pointed out that the warm population is *not* thermalised, its distribution is *not* following a Maxwellian and the double-kappa fit is often *not* suitable, especially at large heliocentric distances (*Myllys et al. 2019*). Furthermore, part of the warm population is unseen by RPC-IES (*Madanian et al. 2016*), as a result of the combination of the lowest energy of detection (4.3 eV for electrons) and of the precarious effect of the spacecraft potential. Prior to launch, it was not anticipated that the spacecraft would ‘charge’ so negatively. In space, there is no

ground/earth and the spacecraft may charge positively or negatively, depending on the material it is made of and the interaction with the surrounding plasma environment. At 1P, the spacecraft potential of Vega-1 and Vega-2 was only a few volts, negative ( $V_{\text{SC}} < 0$ ) or positive ( $V_{\text{SC}} > 0$ ) (*Pedersen et al. 1986*). In contrast, at 67P, the warm and dense cometary electron population was responsible for the negative spacecraft potential, often between  $-15\text{ V}$  and  $-5\text{ V}$ , rarely below  $-20\text{ V}$  (*Odelstad et al. 2017*). Biased elements on solar panels attracting cold electrons also contributed to the negative spacecraft potential (*Johansson et al. 2020*). The presence of a negative spacecraft potential prevented low-energy electrons ( $0 < E_{k,e^-} < -qV_{\text{SC}}$ , where  $E_{k,e^-}$  is the electron kinetic energy and  $q > 0$ ) to reach the spacecraft itself. In contrast, those with energies  $E_{k,e^-} > -qV_{\text{SC}}$  could reach the spacecraft with a reduced kinetic energy,  $E_{k,e^-} + qV_{\text{SC}}$  (see Fig. 6). This should be accounted and corrected for when analysing the RPC-IES electron spectrometer dataset (*Broiles et al. 2016a*; *Galand et al. 2016*).

The warm electron population was detected at 67P by two other instruments less sensitive to the spacecraft potential: the spherical Langmuir Probe (*Eriksson et al. 2007*, LAP) and the Mutual Impedance Probe (*Troignon et al.*

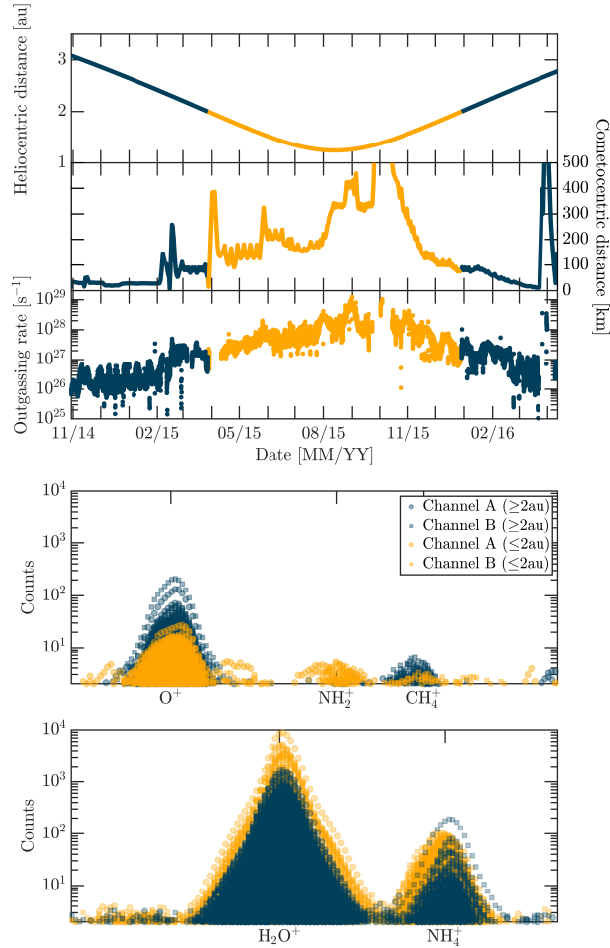


Fig. 10.— Top: Overview of the heliocentric and comencentric distances of Rosetta, and of the outgassing rate during the operational phase of ROSINA-DFMS mass spectrometer in ion mode. Middle and bottom: Spectra at 16 u and 18 u from ROSINA/DFMS mass spectrometer during Rosetta’s mission. Both colours are associated with different heliocentric distances: above (blue) or below (yellow) 2 au. Adapted from *Beth et al. (2020)*.

2007, MIP), both part of the RPC consortium. The RPC-LAP, based on a century-old technique, provides insight on both the ion and electron populations. The principle is relatively simple. A metallic sphere is set at different voltages, scanning from  $-30$  V to  $+30$  V in a short period of time, and the total current from charged particles in the plasma collected by the probe is measured. It results in a characteristic  $I - V$  curve (collected current  $I$  vs applied voltage  $V$ ) which, upon strong assumptions on the velocity distribution function of the ions and electrons, and on the ion mass, may give access to macroscopic properties of the surrounding plasma, including number density, electron temperature, and ion speed (*Mott-Smith and Langmuir 1926*). The second instrument, RPC-MIP, is able to probe the dielectric characteristics of the plasma to derive electron number density and temperature. In active mode, it consists

in two emitting/transmitting electrodes excited by an intensity source of very high impedance. The excited electrodes inject an alternating current  $I(\omega)$  (where  $\omega$  is the angular frequency) into the medium, here the cometary plasma environment. This induces a voltage difference  $V(\omega)$  between the two other receiving electrodes, itself a function of the frequency,  $\omega$ . Expanding the concept of resistance to alternating currents, the ratio  $Z(\omega) = V(\omega)/I(\omega)$  is therefore an impedance containing information on both amplitude and phase (complex number). Between emitting and receiving electrodes, the surrounding plasma plays the role of a ‘filter’ as its dielectric constant  $\epsilon$  depends on the frequency:  $Z(\omega)$  is maximum near the electron plasma frequency  $\omega_{p,e}$ , that is,  $\max Z(\omega) \approx Z(\omega_{p,e})$  where:

$$\omega_{p,e} = \sqrt{\frac{q^2 n_e}{m_e \epsilon_0}}, \quad (53)$$

(with  $m_e$  the electron mass and  $\epsilon_0$  the vacuum permittivity) as the plasma is in resonance. Indeed,  $\omega_{p,e}$  corresponds to the natural frequency at which electrons oscillate in response to a small charge separation. Beside this simple approach to derive the electron density in a non-magnetised plasma characterised by only one electron temperature, more elaborated processing taking advantage of the full RPC-MIP mutual impedance spectra as a function of frequency can be applied to the dataset in order: (1) to derive electron density and temperature for two different electron populations, here warm and cold (when the densities are high enough and Debye length suitable for the operation mode). Indeed, the Debye length is defined by

$$\lambda_{\text{Debye}} = \sqrt{\frac{\epsilon_0 k_B T_e}{q^2 n_e}} = \frac{v_{\text{th},e}}{\omega_{p,e}} \quad (54)$$

where  $v_{\text{th},e} = \sqrt{k_B T_e / m_e}$  is the electron thermal speed.  $\lambda_{\text{Debye}}$  is a characteristic plasma length which corresponds to the typical distance at which electromagnetic waves are screened and damped by the surrounding plasma (here mainly electrons): RPC-MIP operates efficiently when the emitter-receiver distance is greater than  $2\lambda_{\text{Debye}}$ . (2) to take into account the magnetisation of the environment, and/or (3) to include the presence of an ion sheath surrounding the spacecraft and the probe as a result of the negative spacecraft charging (*Gilet et al. 2017, 2020; Wattieaux et al. 2019, 2020*). In passive mode, the emitting antennas are turned off and the plasma plays the role of a natural emitter of electromagnetic waves. The spectra measured corresponds to the Fourier Transform of the voltage in this case.

At 67P at low activity ( $> 2$  au), the cometary plasma is dominated by warm electrons, with a mean energy typically around 5–10 eV but varying between 2–20 eV (*Wattieaux et al. 2020*). Observations from RPC-LAP (*Edberg et al. 2015*), RPC-MIP (*Heritier et al. 2017*), and RPC-IES (*Myllys et al. 2019*) showed that the (warm) electron number density  $n_{e,\text{warm}}$  followed a  $1/r$  dependence with comencentric distance. *Galand et al. (2016), Heritier et al.*

(2017), and *Heritier et al.* (2018) demonstrated that the warm electrons were produced by electron-impact ionisation and, to a lesser extent, photoionisation, and are lost through transport: The plasma density is well captured by Eq. 42 following a  $1/r$  dependence (see Section 2.4.1). The warm electron number density was found to be slightly decreasing with increasing heliocentric distance at Rosetta’s position, a result of the increase in  $r$  with heliocentric distance throughout the mission. It is more pronounced when the electron number density is normalised to a given cometocentric distance  $r$  (*Myllys et al.* 2019). Moreover,  $n_{e,warm}$  increased during solar events due to an increase in the ionising electron population (*Hajra et al.* 2018). Its dependence with season and hemisphere is discussed in *Heritier et al.* (2018).

Near perihelion, the warm population around 67P was primarily driven by photoionisation (*Heritier et al.* 2018). The newborn, warm photoelectrons are quickly cooled through collisions with neutral species and the cometary electron population becomes *cold* (*Gilet et al.* 2020). The relative importance of the warm versus cold electron populations observed in the inner coma of 67P during the Rosetta mission is reviewed in Section 3.1.2.

### 3.1.2. From warm to cold cometary electrons

Since the newborn electrons have average energies ( $\sim 10$  eV, see Section 3.1.1) well above the cometary neutrals (0.01 eV near the surface, see *Gombosi et al.* 1986, and the chapters by Marschall et al. and Biver et al. in this volume), if the coma is dense enough, electrons may undergo efficient energy degradation through collisions with neutrals. The lowest electron temperature which can be reached is the temperature of the cometary neutrals.

Evidence of cold electrons was provided by electron spectrometer measurements from the ICE spacecraft in the tail of 21P (*Meyer-Vernet et al.* 1986; *Zwickl et al.* 1986). Indirect evidence during 1P’s flyby by Giotto near 1 au from the analysis of observed ion composition by the use of an ionospheric model and observed neutral densities and composition (*Eberhardt and Krankowsky* 1995): They derived electron temperature as low as  $10^2$  K ( $\sim 0.1$  eV) at a cometocentric distance of 2000 km.

At 67P, the RPC-LAP and RPC-MIP sensors detected cold electrons (*Eriksson et al.* 2017; *Gilet et al.* 2017). Both instruments have their own limitations in the cold electron detectability (i.e. the highly negative potential of Rosetta when the cold electron density is high can completely hide cold electrons from RPC-LAP, while assumptions used in the complex model used for RPC-MIP analysis of cold electrons may not always be valid, for example when the ratio of warm and cold temperatures is too small, see *Gilet et al.* 2020; *Wattiaux et al.* 2019). Despite these limitations, general trends were inferred (*Engelhardt et al.* 2018; *Odelstad et al.* 2018; *Gilet et al.* 2020; *Wattiaux et al.* 2020). Though largely fluctuating, the contribution of the cold electrons to the total electron population was observed

to mainly increase with local outgassing (hence latitude through season) and to decrease with cometocentric distance  $r$  and heliocentric distance  $r_h$ . Cold electrons were always detected when Rosetta was within the diamagnetic cavity where cold electrons made up close to 100% of the total electron density. Post-perihelion, the largest contribution of cold electrons was found to be over the southern, summer/autumn hemisphere, reaching values up to 70% to 90% of the total electron population, with temperatures as low as 0.05 eV and number densities as high as  $1000\text{ cm}^{-3}$ . *Gilet et al.* (2020) ruled out the influence of the neutral composition as  $\text{H}_2\text{O}$  (abundant in the northern hemisphere) and  $\text{CO}_2$  (more abundant in the southern hemisphere) have similar momentum-transfer cross sections. However, one may note that  $\text{H}_2\text{O}$  has higher total cross-sections than  $\text{CO}_2$  (see Fig. 6): Electrons, on average, lose more momentum by colliding with  $\text{CO}_2$  than with  $\text{H}_2\text{O}$ , although collisions with the former are scarcer.

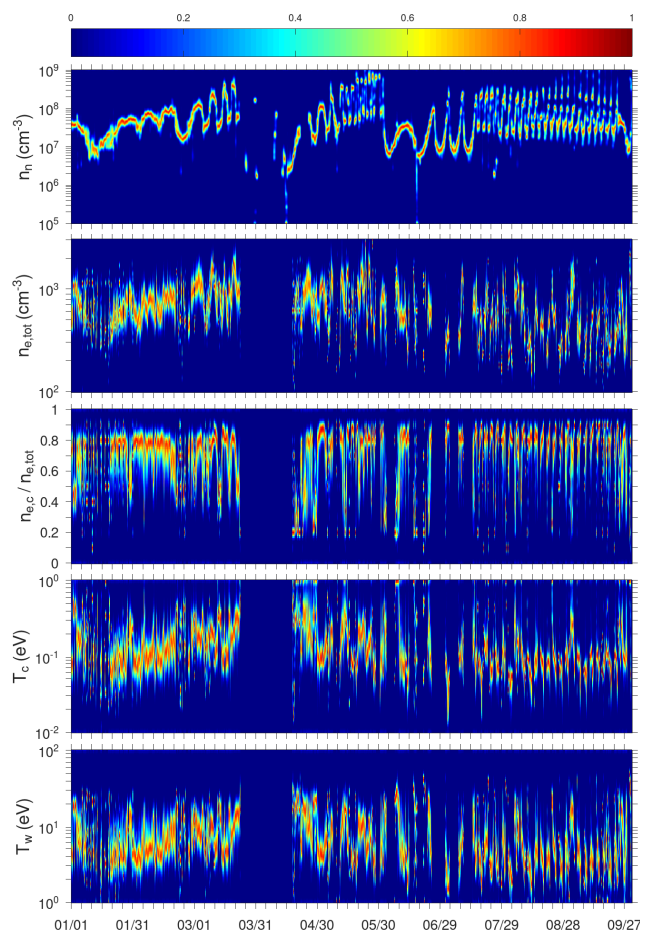


Fig. 11.— Evolution of the total neutral number density  $n_n$ , electron number density  $n_e$ , fraction of cold electrons  $n_{e,cold}/n_{e,total}$ , and temperatures of both populations  $T_{cold}$  and  $T_{warm}$  from January to September 2016 (DD/MM) at Rosetta. The dispersion of the results was computed and normalised over time intervals of 6 h. Colour bar corresponds to the occurrence. Adapted from *Wattiaux et al.* (2020).

At 1P, the presence of cold electrons was predicted by ionospheric models and showed that, for high outgassing activity, the bulk of the cometary plasma is cold, with electron temperatures reaching values as low as the neutral temperature within the diamagnetic cavity (See Section 3.3), whereas warm electrons, constantly produced, but in minority, continue to be present (Mendis *et al.* 1985; Kőrösmezey *et al.* 1987; Gan and Cravens 1990; Eberhardt and Krankowsky 1995). At larger cometocentric distances, the electron temperature is expected to increase as: (i) electron and neutral densities decrease, hence their collision probability decreases and (ii) there is efficient heating of the cold electrons through Coulomb collisions between the cold electrons and the newborn, more energetic, electrons.

In order to assess where electrons may undergo significant collisions, a heuristic approach may be applied. Similar to planetary atmospheres, one may estimate the position of the so-called *exobase* (also *critical level*, Jeans 1923; Spitzer 1949; Chamberlain 1963), that is, the boundary where the gas (here electrons) transitions from a continuum flow (collisional) to a free-molecular regime (collisionless). It is also defined as the critical limit where the atom/molecule undergoes one collision on average along its path outwards to infinity. For this, one may evaluate the *Knudsen* number:

$$\text{Kn} \sim \frac{\ell_{e^-, \text{mfp}}}{L}$$

where  $\ell_{e^-, \text{mfp}}$  stands for the mean free path (i.e. the mean distance covered by a particle between two successive collisions, here  $(n_n \sigma_{e,n})^{-1}$  where  $\sigma_{e,n}$  is the electron-neutral total cross section as electrons mainly collide with neutrals) and  $L$  stands for a characteristic length (for instance, the electron number density scale height  $|\nabla \log n_i|^{-1}$ , here  $\sim r$ ). The electron exobase is expected to be located at a cometocentric distance:

$$\text{Kn} \sim 1 \longrightarrow r_{e^-, \text{exo}} = L \sim \frac{1}{n_n \sigma_{e,n}} \quad (55)$$

Cold electrons were expectedly detected near perihelion (around 1.24 au, with  $Q \sim 10^{28} \text{ s}^{-1}$ , Hansen *et al.* 2016; Engelhardt *et al.* 2018; Gilet *et al.* 2020) when the electron exobase predicted by Eq. 55 can reach a few hundred kilometres.

Surprisingly, cold electrons were also detected away from perihelion beyond heliocentric distances of 3 au ( $Q < 10^{26} \text{ s}^{-1}$ , Gilet *et al.* 2020), when the electron exobase predicted by Eq. 55 is located below the surface (Engelhardt *et al.* 2018; Gilet *et al.* 2020). Hence, no efficient cooling of the electrons by collisions with neutrals was anticipated. The simple approach based on the Knudsen number implies a radial flow for the electrons, which is not sufficient to generate a cold electron population as observed with Rosetta (Gilet *et al.* 2020). 3D modelling from Particle-in-Cell (PiC) simulations, applied to low outgassing comets, have shown that electrons are trapped in the close environment of the nucleus (Deca *et al.* 2017, 2019; Sishila *et al.* 2019).

This region is set up by an ambipolar electric field produced by the cometary plasma. Based on a 3D kinetic test particle model, Stephenson *et al.* (2022) demonstrated that the trapping increases significantly the path of electrons in the dense coma close to the nucleus: This allows electrons to undergo substantial collisions and become cold despite low neutral densities. In the light of the complex, electromagnetic environment at low outgassing, the electron exobase needs to be moved closer to the nucleus than originally predicted through the Knudsen number.

### 3.1.3. Accelerated electrons

The most energetic electron population is often referred to as *suprathermal*, either as their energy exceeds  $k_B T_e$  where  $T_e$  is the mean temperature of the whole electron population, or as their energy distribution departs from a Maxwellian distribution at high energies (that is,  $f_e(E) dE \propto \sqrt{E} \exp(-E/k_B T_e) dE$ ). Note that the warm electron distribution in energy also departs from a Maxwellian distribution. The electron population under focus in this section corresponds to electrons with energies above the mean energy of the whole electron population dominated by cold and warm electrons (and above the upstream solar wind electrons, i.e. around 10 eV). Their energy distribution tends not to decrease exponentially (i.e.  $f_e(E) \propto \sqrt{E} \exp(-E/k_B T_e)$ ) but rather follows a power law (i.e.  $f_e(E) \propto E^{-\kappa}$ , as in kappa distributions). The reason for such a behaviour in a plasma and its possible ubiquity in nature are still debated and beyond the scope of this chapter (Pierrard *et al.* 2016).

Let us review the findings on the *hot* electron population detected by Rosetta by the RPC-IES electron spectrometer (Broiles *et al.* 2016a,b; Myllys *et al.* 2019). It was derived by fitting a suprathermal double-kappa function on the electron velocity distribution. From such a fitting, characteristics of the warm and hot populations were derived. While the bulk of the electron population is dominated by warm and/or cold electrons (see Section 3.1.1 and Section 3.1.2), the hot electrons with temperatures of a few tens of eV are rarefied with typical densities below a few  $\text{cm}^{-3}$  (Myllys *et al.* 2019). Their density was found to decrease significantly from 3-10  $\text{cm}^{-3}$  near perihelion down to less than 0.1  $\text{cm}^{-3}$  at large heliocentric distances (3.0-3.8 au, Broiles *et al.* 2016a; Myllys *et al.* 2019). Their temperature does not exhibit any strong dependence with heliocentric distance or cometocentric distance. The dependence of the hot population with  $r$  is significantly less than for the warm population, with a dependence more in  $r^{-2}$  than in  $r^{-1}$ , though the uncertainty is large and the dependence breaks below 50 km. The energy distribution measured by RPC-IES needs to be corrected to take into account the spacecraft potential which is ranging between  $-20$  to  $-5$  eV typically (see Fig. 6 and Section 3.1.1).

The source of the hot electron population has been under debate. It was first proposed by Broiles *et al.* (2016a) to be suprathermal halo solar wind electrons (Pierrard *et al.*

2016). *Myllys et al.* (2019) however showed that the hot electron population observed at Rosetta is denser (by almost an order of magnitude) and colder than the solar wind halo component. Furthermore, they found an increase in the electron temperature with increasing invariant kappa index, an opposite trend to the one derived for the halo solar wind electrons (*Pierrard et al.* 2016). Hence, the bulk of the hot electrons has a different origin.

At large heliocentric distances, *Madanian et al.* (2016) suggested that electrons could be accelerated towards the comet by an ambipolar electric field and that this field was the result of the electron pressure gradient due to plasma inhomogeneity observed close to the comet. When an electron is born far from the comet or comes from the space environment, such as the solar wind electrons, it is accelerated towards the cometary nucleus when falling into the potential well set up by the ambipolar electric field. Using a self-consistent collisionless PiC model applicable to weakly outgassing comets, *Deca et al.* (2017) showed that the suprathermal electrons present close to the comet are originating from the solar wind and accelerated by the ambipolar electric field set up by cometary plasma. This explanation is consistent with the large-scale acceleration process for the source of the suprathermal electrons responsible for auroral emissions (*Galand et al.* 2020; *Stephenson et al.* 2022). These atomic emissions observed in the Far UltraViolet (FUV) by the UV spectrograph Alice onboard Rosetta were shown to result from the dissociative excitation of molecules, such as water and CO<sub>2</sub>, by energetic (> 15–20 eV) electrons. Through a multi-instrument analysis, it was found that the variation in the FUV brightnesses correlated very closely with the variation in the electron-impact emission frequency, driven by the RPC-IES electron flux. This remained true even during solar events and when the FUV emissions were observed at the limb, far from the location of Rosetta where the RPC-IES was measuring the suprathermal electrons. These accelerated solar wind electrons play a critical role in the cometary environment, as they are responsible not only for the auroral emissions, but also for the bulk of the ionisation, and hence of the cometary plasma, at large heliocentric distances (see *Galand et al.* 2016; *Heritier et al.* 2018, and Section 2.2.2).

Near perihelion, the source of the suprathermal electrons is still under debate. Indeed, with the formation of a dense ionosphere under solar illumination, a diamagnetic cavity (see Section 3.3) is formed around the cometary nucleus and solar wind electrons do not have (easy) access to the inner ionosphere any more. *Madanian et al.* (2017) observed a modest but consistent drop in the RPC-IES electron fluxes over the 40 eV to 100 eV range between outside and inside the diamagnetic cavity. They showed that the lower fluxes measured inside the cavity are however too high to be explained by photoelectrons alone. They proposed two mechanisms to explain the observations: a trapping mechanism of the photoelectrons inside the cavity and/or the penetration of part of the solar wind electrons into it.

### 3.2. Effect on the ion dynamics

Electrons play a critical role in the plasma and ion dynamics. Indeed, as their mass is much lower than that of positive charges, such as protons, they have a greater mobility and react quicker to changes in the electromagnetic fields.

Ion dynamics is largely driven by macroscopic electric fields. In cometary and classical (i.e. not relativistic) plasmas, quasi-neutrality holds ( $n_i \approx n_e$ ) and hence the charge density ( $q(n_i - n_e)$ ) is very small at large temporal and spatial scales. This means that the Maxwell-Gauss equation is reduced to  $\nabla \cdot \mathbf{E} \approx 0$  and it cannot be used to derive the electric field (no unique solution in absence of boundary conditions). An alternative equation needs to be used; this is the Generalised Ohm's Law (GOL) which can be derived from the electron momentum equation as follows. For the electron momentum density  $n_e m_e \mathbf{V}_e$ , its temporal evolution in conservation form is given by:

$$m_e \frac{\partial(n_e \mathbf{V}_e)}{\partial t} = - \overbrace{\nabla \cdot \mathbf{P}_e}^{\text{P}_e \text{ gradient}} - \overbrace{\nabla \cdot (n_e m_e \mathbf{V}_e \otimes \mathbf{V}_e)}^{\text{Electron dynamic pressure gradient}} - \underbrace{qn_e(\mathbf{E} + \mathbf{V}_e \times \mathbf{B})}_{\text{Lorentz force}} + \underbrace{n_e m_e \mathbf{a}_{ext}}_{\text{External forces}} + \frac{\delta \mathcal{P}_e}{\delta t} \quad (56)$$

where  $\mathbf{a}_{ext} = \mathbf{F}_{ext}/m_e$  with  $\mathbf{F}_{ext}$  the set of forces acting upon electrons which are not electromagnetic and independent of the environment, for instance gravity,  $\mathbf{P}_e$  and  $\mathbf{V}_e \otimes \mathbf{V}_e$  are tensors of rank 2, which are  $3 \times 3$  matrices in 3D, and  $\delta \mathcal{P}_e/\delta t$  encompasses all microscopic source and loss of electron momentum, for instance frictional interactions between electrons and neutrals/ions (*Cravens* 1997b; *Szegö et al.* 2000).

The electron number density  $n_e$  (a scalar), the electron mean (bulk) velocity  $\mathbf{V}_e$  (a vector), and the electron thermal pressure  $\mathbf{P}_e$  (a matrix) are mathematically defined respectively as the zeroth, first, and second central moments of the electron distribution function over velocity space and are given by:

$$n_e(\mathbf{r}) = \int_{\mathbb{R}^3} f_e(\mathbf{r}, \mathbf{v}) d^3\mathbf{v} \quad (57)$$

$$V_{e,j}(\mathbf{r}) = \frac{1}{n_e(\mathbf{r})} \int_{\mathbb{R}^3} v_j f_e(\mathbf{r}, \mathbf{v}) d^3\mathbf{v} \quad (58)$$

$$P_{e,jk}(\mathbf{r}) = m_e \int_{\mathbb{R}^3} [v_j - V_{e,j}(\mathbf{r})][v_k - V_{e,k}(\mathbf{r})] f_e(\mathbf{r}, \mathbf{v}) d^3\mathbf{v} \quad (59)$$

$$[\mathbf{V}_e \otimes \mathbf{V}_e]_{jk} = V_{e,j}(\mathbf{r}) V_{e,k}(\mathbf{r}) \quad (60)$$

where  $\mathbf{v}$  is the particle's velocity vector, a microscopic quantity to distinguish from the particle's bulk velocity  $\mathbf{V}(\mathbf{r})$ , a macroscopic (averaged) quantity at the location  $\mathbf{r}$ .  $j$  and  $k$  are indices for the different components (e.g.  $j, k = x, y, z$  and  $d^3\mathbf{v} = dv_x dv_y dv_z$  in Cartesian coordinates, 9 possible combinations in 3D, but there are different

for other geometries).  $f_e(\mathbf{r}, \mathbf{v})$ , in electrons  $\text{m}^{-6} \text{s}^3$ , is a fundamental function which contains all the properties of the electrons: It is the so-called velocity distribution function and corresponds to the density of particles (here electrons) in the volume element  $d^3\mathbf{r} d^3\mathbf{v}$  around the position  $(\mathbf{r}, \mathbf{v})$  in the space-velocity domain (6 dimensions).  $f_e$  gives a continuous statistical description of the behaviour of the electrons with their number at a given velocity and at a given position.  $f_e(\mathbf{r}, \mathbf{v})/n_e(\mathbf{r})$  may be interpreted as a *probability distribution function* in the mathematical sense. As such,  $f_e$  can be reconstructed from moments at all orders. However, this is impossible in practice: Only a limited set of equations can be solved and moments can be known or approximated. In addition, the temporal evolution of the moment of order  $n$  always involves the divergence of the moment of order  $n + 1$  (Eq. 56). This is the reason why most mathematical models (e.g. MHD approach) apply closures which approximate the expressions of high order moments in terms of low order ones (e.g. see *Grad 1949; Chapman and Cowling 1970*, for a mathematical description).

Two simplifying assumptions may be done here: steady state and massless electrons. As electrons have a very low mass, they do not have inertia nor contribute to the dynamic pressure. In addition, at comets, forces such as gravity are irrelevant. Within a cometary plasma, the thermal energy is mainly carried by the electrons, while the dynamic pressure is carried by the ions. If we ignore microscopic source and loss terms of electron momenta and with the aforementioned assumptions, Eq. (56) becomes:

$$0 \approx -\nabla \cdot \mathbf{P}_e - qn_e \mathbf{E} - qn_e \mathbf{V}_e \times \mathbf{B} \quad (61)$$

Instead of writing in terms of electron velocities, it is more common to use  $\mathbf{V}$ , the mean plasma velocity, and  $\mathbf{J}$ , the current density, given by:

$$\begin{aligned} \mathbf{V} &= \frac{n_i m_i \mathbf{V}_i + n_e m_e \mathbf{V}_e}{n_i m_i + n_e m_e} \\ \mathbf{J} &= qn_i \mathbf{V}_i - qn_e \mathbf{V}_e \end{aligned}$$

and conversely

$$\mathbf{V}_i \approx \mathbf{V} \text{ and } \mathbf{V}_e \approx \mathbf{V} - \frac{\mathbf{J}}{qn_e}$$

if  $n_i \approx n_e$  and as  $m_e \ll m_i$ . Eq. (61) becomes:

$$0 \approx -\nabla \cdot \mathbf{P}_e - qn_e \mathbf{E} - qn_e \mathbf{V} \times \mathbf{B} + \mathbf{J} \times \mathbf{B} \quad (62)$$

that is

$$\mathbf{E} \approx -\mathbf{V} \times \mathbf{B} - \underbrace{\frac{1}{qn_e} \nabla \cdot \mathbf{P}_e}_{\text{Motional/convective}} + \underbrace{\frac{1}{qn_e} \mathbf{J} \times \mathbf{B}}_{\text{Hall term}} \quad (63)$$

known as the GOL. It is not the most rigorous demonstration and, for more details, the reader is referred to *Somov (2007)* or *Valentini et al. (2007)*, for example. This equation is fundamental as it provides a relatively good, unique,

and physical estimate of the electric field without solving the Maxwell-Gauss equation at large temporal and spatial scales. The contributions of the different terms have been assessed at low outgassing activity by *Deca et al. (2019)* and are detailed in the chapter by *Götz et al.* in this volume.

In Eq. 63, one term is dominating the ion acceleration in the inner coma, within the diamagnetic cavity, and along the magnetic field: the ambipolar/polarisation electric field, defined as  $\mathbf{E}_{P_e} \approx -\nabla \cdot \mathbf{P}_e / (qn_e)$ . In the inner coma, electron and ion densities are dominated by the population of cometary origin which only depends on the cometocentric distance (assuming spherical symmetry). Let us extend this assumption to the electron pressure and temperature. In such a case,  $\mathbf{E}_{P_e}$  is only radial and its amplitude is given by:

$$E_{P_e} \approx -\frac{1}{qn_e} \frac{\partial P_{e,rr}}{\partial r} - \frac{2P_{e,rr} - P_{e,\theta\theta} - P_{e,\phi\phi}}{r} \quad (64)$$

where  $P_{e,rr}$  stands for the electron pressure component along  $r$  and  $P_{e,\theta\theta}$  and  $P_{e,\phi\phi}$  stand for both perpendicular components. In spherical symmetry,  $P_{e,\theta\theta} = P_{e,\phi\phi}$  with  $\theta$  and  $\phi$  the polar and azimuthal angles in spherical, polar coordinates. If the electron temperature is isotropic with a temperature  $T_e(r)$  (i.e.  $P_e = P_e(r) \mathbf{I}_3 = n_e(r) k_B T_e(r) \mathbf{I}_3$  where  $\mathbf{I}_3$  is the identity matrix and  $P_e(r) = n_e(r) k_B T_e(r)$  is a scalar), Eq. 64 is reduced to (*Cravens et al. 1984*):

$$E_{P_e} \approx -\frac{1}{qn_e} \frac{dP_e}{dr} = -\frac{k_B T_e}{q} \frac{d \log n_e}{dr} - \frac{k_B}{q} \frac{dT_e}{dr} \quad (65)$$

Neglecting the electron temperature gradient and as  $n_e(r) \propto 1/r$  from theory and observations (e.g. see *Balsiger et al. 1986; Edberg et al. 2015; Beth et al. 2019*), one gets (*Vigren et al. 2015*):

$$E_{P_e} \approx \frac{k_B T_e}{qr} \quad (66)$$

As the electrons have often more energy in the form of thermal agitation (though it may not be valid in the inner coma of 1P), electrons can leave the coma faster than the ions. However, quasi-neutrality should be maintained and  $\mathbf{E}_{P_e}$  ensures to keep it that way, in particular along the magnetic field lines as other components act perpendicular to  $\mathbf{B}$ .  $\mathbf{E}_{P_e}$  appears mainly radial, oriented outwards near the nucleus: it decelerates escaping cometary electrons inwards and accelerates cometary ions outwards. Conversely, ions coming from outside would be deflected and repelled from the nucleus, while electrons would be attracted and accelerated as they approach the nucleus (see Fig. 12).

Eq. 66 should be considered with great caution as it is based upon some assumptions (e.g. constant and isotropic  $T_e$  through the coma) difficult to verify with a single spacecraft and, above all, a negatively charged one. It provides insight on how the electric field and associated potential might behave in the inner ionosphere but should not be applied over large scales (e.g. from the surface to the infinity in terms of cometocentric distances) or at low outgassing activity. Indeed, the associated potential would be



in  $\log(r)$  trapping all cometary electrons, preventing them to reach infinity while cometary ions could escape, leading to a charge imbalance. In addition, PiC simulations performed by *Deca et al.* (2019) at low outgassing activity show that  $\mathbf{E}_{P_e}$  is not spherically symmetric near the nucleus (despite having assumed a spherically symmetric outgassing) and hence it cannot be described by Eq. 66.

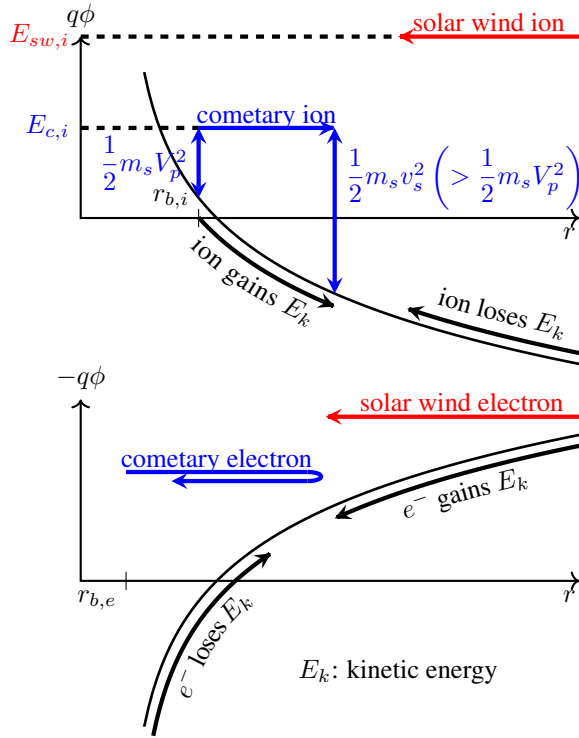


Fig. 12.— Schematic of how ions and electrons may gain/lose energy by means of the electric potential  $\phi$  (black line). This potential is driven by the electron pressure and is plotted as a function of the cometocentric distance  $r$ . Solar wind electrons gain energy as they fall and dive towards the nucleus, while cometary electrons born close to the nucleus at  $r_{b,e}$  ( $< 10 - 100 r_c$ ) are trapped by the potential well. In contrast, solar wind ions are barely decelerated and cometary ions are accelerated, though the gain in kinetic energy will depend on their birthplace  $r_{b,i}$  and the potential profile. Magnetic field and collisions have been ignored here. The red and blue arrows show the direction of motion of the particles.

From this approach, one would expect ions to be accelerated and exceed the local neutral speed at which they are born in the first tens or hundreds kilometres above the surface. However, this was not the case at 1P for example. *Schwenn et al.* (1987) showed that the radial component of the ion velocity at 1P remained steady, close to the neutral speed between the closest approach and 20,000 km. This means either that ions and neutrals are collisionally cou-

pled and ions might not experience any radial acceleration by means of electromagnetic forces. As aforementioned,  $\mathbf{E}_{P_e}$  depends on the electron/plasma temperature. *Eberhardt and Krankowsky* (1995) showed that the plasma temperature in the same region was cold, increasing gradually from 100 K (0.01 eV) at 2000 km to 900 K (0.09 eV) at 8500 km. This must be compared with the kinetic energy of newborn water ions which is around 0.1 eV. Therefore, at 1P, near the nucleus, newborn ions are slightly supersonic (their initial speed exceeds  $\sqrt{k_B(T_i + T_e)/m_i}$ ). This translates into the presence of an inner shock ahead of the contact surface (*Cravens* 1989; *Goldstein et al.* 1989). As ions decelerate when approaching the contact surface, supersonic ions become subsonic and a shock forms before being deflected. The existence of this shock was anticipated before Giotto (see *Houpis and Mendis* 1980). However, it was difficult and hard to observe as Giotto was too fast.

The situation is different at 67P. Although cold electrons were observed during Rosetta’s escort phase, the mean electron temperature was mostly around 5–15 eV. Nevertheless, *Gilet et al.* (2020) showed that within the diamagnetic cavity the electron population was dominated by the cold component ( $< 0.1$  eV), consistent with previous observations by *Odelstad et al.* (2018). It is then not clear whether or not ions were subsonic/supersonic at birth, if that depends on the cometary activity and location (e.g. within and outside the diamagnetic cavity) or on the ability of solar wind ions and electrons to access the inner ionosphere. This aspect should be further investigated in the future.

### 3.3. Diamagnetic cavity

Amongst the different regions met at comets and the boundaries separating the different environments, covered in the chapter by *Götz et al.* in this volume, one in particular draws our attention regarding the inner cometary ionosphere: the *diamagnetic cavity*. The adjective ‘diamagnetic’ comes from an analogy to materials which, if subject to an external magnetic field, generate in response an induced magnetic field in the opposite direction in order to reduce or nullify the total magnetic field strength. The diamagnetic cavity is characterised by an almost null magnetic strength (below instrumental detection) and a steep magnetic field gradient at its edge, the latter having different nicknames in the literature: *ionopause*, *contact surface*, or the *diamagnetic cavity boundary layer* (DCBL). This boundary is a tangential discontinuity whose existence was already anticipated by *Biermann et al.* (1967). The diamagnetic cavity was observed at two comets. The first time was during Giotto’s flyby on 13/14 March 1986 (*Neubauer et al.* 1986) when the spacecraft entered into the cavity for two minutes crossing the boundary at around 4500–5000 km (*Neubauer* 1987). The second time was during the Rosetta mission on 26 July 2015 (*Goetz et al.* 2016b), followed later by the identification of more than 600 crossings (*Goetz et al.* 2016a). The detections were performed a few months on either side of the perihelion passage when 67P was most ac-

tive; however, no detection at the location of Rosetta could be achieved at large heliocentric distances, missing the anticipated shrinking and/or disappearance of the diamagnetic cavity.

The origin of the boundary, the physics at play at the boundary, and how to maintain it were ardently debated in the 1990s following the detection of the diamagnetic cavity at 1P during the Giotto flyby. Debates converged in one idea: As the coma of 1P was extremely dense, the force induced by the magnetic field gradient (pressure and tension) may be balanced by the force exerted by the neutrals on the ions by means of collisions, the so-called *ion-neutral drag*, of which the strength depends on  $|\mathbf{V}_i - \mathbf{V}_n|$  (Cravens 1986; Ip and Axford 1987). Indeed, at the microscopic level, as ions and neutrals may have very different velocities and neutrals are much more abundant, collisions tend to reduce the gap between both speeds and force the velocity of ions to be closer to that of neutrals. However, to balance the magnetic pressure in the right direction, ions are required to be slower than neutrals at the boundary and beyond, with for instance a null or even inward ion velocity. This strong velocity requirement was in general not fulfilled at 67P during Rosetta’s many hundred crossings of the boundary, questioning the validity of the simple ion-neutral drag model at low outgassing conditions. The question of whether or not this region is associated with collisions is open. Nevertheless, statistical studies have provided valuable insight. For instance, at 67P, Henri *et al.* (2017) showed that the DCBL crossings occurred close to the electron-neutral exobase (see Section 3.1.2), meaning that collisions between electrons and neutrals might play a critical role in the formation of this cavity. Further evidence that collisions and electron cooling might have a significant role in its formation was the presence of a shock on the inner edge of the diamagnetic cavity at 1P (Gombosi *et al.* 1996; Rubin *et al.* 2009). The cause is quite well understood: Ions are born supersonic at 1P (i.e.  $V_n \gtrsim \sqrt{k_B T_e / m_i}$ ) and as they are slowed down by the magnetic field gradient, they undergo deceleration from supersonic to subsonic speeds and a shock forms at the transition. Although  $V_n$  is not expected to vary between comets,  $T_e$  does and was extremely low at 1P compared with 67P. Such a low value is associated with high outgassing and cooling through collisions with the neutrals.

For a modelling perspective, it is critical to predict whether a diamagnetic cavity is formed and which shape and size it has, as the plasma dynamics in a magnetised and an unmagnetised medium are very different. On the one hand, in an unmagnetised medium, the plasma dynamics is driven by  $\mathbf{E}_{P_e}$  (see Section 3.2) and symmetries may exist. On the other hand, in a magnetised medium, the symmetry is broken (in a spherically symmetric problem, there is no magnetic field) and the dynamics of ions and electrons becomes more complex. For instance, ions may travel radially in the former case but not in the latter. In addition, the ability to accurately model the transition between collisionless and collisional media with the same approach is challeng-

ing, computationally and mathematically. In the collisional case, kinetic physics including elastic and inelastic collisions is required. 3D modelling of the DCBL remains a key challenge to tackle in the future.

## 4. Ion population

As for electrons, several ion populations, discriminated in energy and origin, were identified during past cometary flybys and during the course of the Rosetta mission. They consist of pickup ions, solar wind ions, and cold cometary ions; each may predominate depending on cometocentric distance and/or cometary activity. Instruments of choice to characterise these populations are ion mass spectrometers. Aboard Rosetta, these were: (1) ROSINA-DFMS, which provided detailed ion composition of the cometary ionosphere thanks to its high mass resolution mode (see Section 2.4.2 for details), (2) RPC-ICA, able to determine the ion distribution function and distinguish in energy, mass, and direction between different populations (e.g. solar wind protons, solar wind alpha particles, pick up ions, cometary ions). In addition, there were the Langmuir probe, RPC-LAP, with the ability to measure the ion current and the electron-ion analyser, RPC-IES, which, although lacking the mass determination, measured the total ion fluxes throughout the mission. This section is dedicated to the different ion populations present within the cometary ionosphere in terms of energy and the processes which might affect the latter.

### 4.1. Collisions versus acceleration

In a cometary ionosphere, energy is stored under different forms, either in the electromagnetic fields ( $B^2/\mu_0$  and  $\epsilon_0 E^2$ ) or within the particles, kinetic or thermal. For electrons ( $T_e \sim 10$  eV at most, see Section 3.1.1) which are light species, the energy is mainly thermal, whereas for ions, it is mainly kinetic.

Cometary ions are produced from neutrals (see Section 3.1.1). During an ionisation, most of the energy goes to the newborn electron and hence the ion keeps the original momentum of the incident neutral. Thus, newborn ions have an initial speed of  $\sim 0.5\text{--}1$  km s<sup>-1</sup>, namely a kinetic energy of 0.1–0.2 eV for ion masses spanning from 18 to 44 u. If most of the available energy is stored by the electrons in absence of electron and ion collisions, ions should undergo acceleration and ‘drain’ energy from the electrons by means of electromagnetic fields. However, when ion collisions are frequent and ion-neutral chemistry is dominant (see Section 2.4.1), ions struggle to accelerate: An ion may collide with a neutral (e.g. charge exchange or proton transfer), the ion, which may have accelerated, becomes a neutral, the neutral a cold ion (or one of its fragments), reducing the energy of the ion present albeit not affecting the total plasma charge. Although the produced ion may have a different mass from the original one, the total plasma momentum is overall reduced. In a collisional coma (high outgassing rate), another reason why ions have difficulty to be

accelerated by electromagnetic fields is because the latter is weak: The region usually corresponds to the diamagnetic cavity (i.e. low or null magnetic field), dominated by cold electrons, yielding a weak electric field from the weak electron pressure gradient (see Section 3.3).

At comet 1P during the Giotto flyby at 0.89 au, ions were not accelerated in the inner ionosphere (*Schwenn et al. 1987*), either because the coma was dense and/or cometary electrons were too cold for causing a large enough electron pressure-gradient-driven field. Acceleration by ions was observed beyond the diamagnetic cavity, especially from 20,000 km (*Altwegg et al. 1993; Rubin et al. 2009*). What is the situation at 67P? During low outgassing at large heliocentric distances (beyond 2 au), a multi-instrument analysis linking datasets from the Rosetta Plasma Consortium (RPC-IES, RPC-MIP, RPC-LAP) and ROSINA (COPS, DFMS) by a physics-based model (see Section 2.4.1) gave excellent agreement in terms of ionospheric density within the instrument uncertainties (*Galand et al. 2016; Heritier et al. 2017, 2018; Vigren et al. 2019*). The model assumes that the ions are moving radially at the speed of neutrals, that is, they have not suffered from any acceleration between their birth place and the location of Rosetta.

Why the models work so well at large heliocentric distances/low outgassing activity (e.g. *Heritier et al. 2018*) is not entirely clear, as there are theoretical as well as observational indications for the acceleration of newborn ions, flowing at speeds around an order of magnitude above the neutral gas speed. Based on theory and models,  $E_{pe}$  must accelerate the ions away from the coma as they are born at subsonic speeds in the case of 67P. Therefore, are the ion-neutral collisions present at 67P, as discussed in Section 2.3, sufficient to limit/prevent this acceleration? Simulations by *Vigren and Eriksson (2019)* indicate that this was not the case at the location of Rosetta even at perihelion, the most active outgassing phase. From RPC-ICA observations, *Bercic et al. (2018)* estimated the outward flow of low-energy cometary ion population during a one-month period when Rosetta was at 28 km from the nucleus at 2.5–2.7 au (low outgassing rate), around  $6 \text{ km s}^{-1}$ . Similar results were also reported by *Nilsson et al. (2020)*. Ion velocities from combined analysis of RPC-LAP and RPC-MIP data (and by two different approaches) have also showed similar ion speeds (*Johansson et al. 2021*).

While these observations appear to be consistent with the expected effect of the ambipolar electric field, one has to be aware of the technical problems with observing low energy ions (a few eVs) by detectors on a spacecraft charging down to negative potentials, typically  $-5$  to  $-20$  V (see Section 3.1.1), accelerating the ions to similar energies. The negative spacecraft potential is believed to be somehow beneficial for RPC-ICA measurements: all the ions must reach the spacecraft and be detectable as the minimum energy threshold of RPC-ICA was below  $-qV_{SC}$ . Simulations of the ion measurements based on Spacecraft Plasma Interaction System (SPIS) did not clearly identify the reason(s) why low energy ions should not reach the RPC-ICA

detector (*Bergman et al. 2020; Bergman et al. 2021*). Some possibilities include the obstruction of its  $360^\circ \times 90^\circ$  field of view, the limited angular coverage in some operational modes, and/or large uncertainties regarding the geometric factor at low energies, that is, the factor which allows to convert counts from the instrument to physical quantities such as the ion differential flux in this case. However, these simulations have also showed that ions, particularly low-energy ones, had very distorted trajectories around Rosetta prior their detection. Regardless, it is clear that the plasma density (the zeroth order moment) from the ion distribution measured by RPC-ICA is one to two orders of magnitude lower than those measured by RPC-MIP and RPC-LAP, considered as baselines, such that the direct measurements of the low energy ions on and at Rosetta is still an open question.

The ion speed derived from combining both measurements by RPC-LAP and RPC-MIP was more indirect. The ion current measured by RPC-LAP is combined with the plasma density from RPC-MIP, assuming only one ion species at 18 or 19 u (an assumption far from being true especially near perihelion, when many ions coexist and might have different speeds, *Beth et al. 2020*), to derive an effective speed, regardless of the direction (*Johansson et al. 2021*). The only indication of flow direction by RPC-LAP was the observation of a dropout in the ion current observed when the spacecraft itself obstructed the ion flow, preventing the ions to reach the probe. It occurred a few times when 67P, the spacecraft, and one of the RPC-LAP probes were aligned (*Odelstad et al. 2018*), as expected for a radial outflow. While completely excluding effects of the spacecraft potential on RPC-LAP is difficult, errors sufficient to explain the large difference to the speed of the neutral gas are equally difficult to conceive. Some might be still inherent to the analysis of Langmuir probes' measurements. Indeed, deriving plasma properties from  $I - V$  curves has never been a straightforward and easy task and relies on assumptions. For instance, it is common to derive the effective ion speed (thermal and bulk speeds are indistinguishable) based on strong assumptions (see the seminal paper by *Mott-Smith and Langmuir 1926*): a single ion population and specific distribution functions (e.g. ring or Maxwellian distribution), drifted or not, in the Orbital Motion Limited (OML) regime (the Debye length is infinite compared with the probe's size, which is not always the case), and for an unmagnetised plasma (while at low outgassing, the environment is magnetised). Depending on the ratio between the probe's radius and the ambient Debye length, the estimates of the ion effective speed may be very different (*Laframboise 1966*) and can differ significantly from the bulk ion speed.

The multi-instrumental approach proposed at large heliocentric distances is not applicable near perihelion due to higher outgassing rates. Additional processes have to be taken into account. For instance, chemical loss through electron-ion dissociative recombination needs to be included (besides loss through transport) as well as attenu-

ation of the EUV solar flux. Although the effect on the electron density of photoabsorption by the neutral gas is ruled out at the location of Rosetta (*Heritier et al.* 2018), *Johansson et al.* (2017) observed attenuation of the EUV solar flux near perihelion. This was attributed to dust, lessening the ionisation rate and causing in part this overestimation as models did not take into account dust absorption. Finally, large ion speeds were also reported (*Vigren et al.* 2017; *Odelstad et al.* 2018) implying that acceleration takes place. If confirmed, this would reduce the electron density locally (*Vigren et al.* 2019) as the models are based on flux conservation.

The apparent discrepancy at low activity between the success of the multi-instrument analysis, assuming  $V_i \approx V_n$  to reproduce the measured ion density, and the observations, indicating much higher ion speeds, needs to be solved. The physics of the interplay of ion-neutral collisions in an inhomogeneous gas with an inhomogeneous and dynamic plasma, bathed in electromagnetic fields varying in space and time, is a very rich and complex matter, with much still to be explored. On the one hand, hybrid simulations may include ion-neutral collisions, but as they lack the electron kinetics, much of the detailed physics causing acceleration is partially lost (e.g. *Koenders et al.* 2015). On the other hand, particle-in-cell (PIC) simulations may include collisions either self-consistently or by application of them as an extra layer somewhat along the lines of *Stephenson et al.* (2022). This approach is expected to be more and more pertinent in the coming years.

#### 4.2. Pick-up ions

In a region where the solar wind flows, the newborn, cometary ions, initially at rest with respect to the ambient plasma, may feel the solar wind convective electric field  $\mathbf{E}_{sw}$  and start being accelerated by it. This process, called ‘pickup’, results, in a kinetic sense, in these accelerated ions of cometary origin having cycloid trajectories in the  $\mathbf{E} \times \mathbf{B}$ -drift direction, where  $\mathbf{B}$  is the local magnetic field. The implicit assumption is that solar wind flow and magnetic field directions are not aligned, so that the cross product is non-zero, otherwise the pickup process would be rendered negligible. In velocity space, the accelerated pickup ions form so-called ‘ring’-shaped velocity distribution functions (VDFs), with a maximum velocity of the picked-up particles of the order of  $2V_{sw} \sin \xi$ , where  $\xi$  is the angle between the local solar wind magnetic field  $\mathbf{B}$  and solar wind velocity  $\mathbf{V}_{sw}$ . Pitch-angle scattering further distributes the energy in phase space transforming the initial ideal pickup ring or partial ring VDFs into bispherical shell VDFs (*Coates* 2004). Such VDFs, from ring-beam to bispherical shells, have been observed at comets including 1P and 67P (e.g. *Coates et al.* 2015; *Nilsson et al.* 2015; *Goldstein et al.* 2015), denoting several stages of evolution in the pickup ion process. In turn, these distributions are unstable and generate waves heating the ambient plasma (*Wu and Davidson* 1972). A more detailed outlook of pickup ions,

their effect on large plasma structures, and wave-particle interactions, is given in the chapter by *Götz et al.* in this volume.

The pickup process has a drastic effect on the solar wind flow (*Glassmeier* 2017). As the energy and momentum are directly transferred from *light* solar wind to *heavy* cometary ions, two effects simultaneously take place: To conserve energy, the solar wind is slowed down upstream of the cometary nucleus, and, to conserve momentum, is deflected in the direction opposite to the pickup ions’ motion. Moreover, due to the instability of the VDFs created in the pickup process, part of the transferred energy is diverted towards the excitation of low-frequency waves (ion cyclotron waves, Alfvén waves, etc.), which in turn heat the plasma and produce local turbulence. Momentum transfer between solar wind and accelerated cometary ions can be particularly encouraged when VDFs are non-gyrotropic, further feeding local instabilities. Because of the implantation of heavy ions into the solar wind flow, the pickup process thus contributes to the mass-loading of the solar wind (*Szegö et al.* 2000), an idea first put forward by *Biermann et al.* (1967).

#### 4.3. Solar wind versus ionospheric plasma

The interaction between the solar wind and the cometary neutral environment gives rise to several coexisting populations of ions, which may take precedence over one another in the inner coma depending on heliocentric distance (and hence, nucleus activity) and on cometocentric distance. What are the conditions for cometary ions (at high or low energy) to prevail over solar wind ions? Historical missions composing the Halley armada or more recently Rosetta give us clues to answer this question.

The transition region where cometary ions gradually become dominant is usually called the *cometopause* (*Cravens and Gombosi* 2004), and sometimes *protonopause* (*Sauer et al.* 1995). It has historically been defined in two ways (see also the chapter by *Götz et al.* in this volume):

- [1] the *charge-exchange collisionopause*,
- [2] the inner region delimited by  $n_{sw} \approx n_{ci}$  (or  $F_{sw} \approx F_{ci}$ ), where  $n$  (resp.  $F$ ) are the total number densities (energy and/or momentum fluxes) of solar wind ions (*sw*) and of cometary ions (*ci*, referred to as solely  $i$  in Section 2).

In definition [2], the cometopause may not be a sharp boundary but rather a smooth cross-over transition between dominating species in the plasma; in the case when the solar wind plasma is shocked and thermal speeds of cometary and solar wind ions are similar, density and flux ratio definitions are equivalent. In fact, the presence or not in the data of a cometopause at 1P and its physical relevance were highly debated at the time of its first discovery (*Gringauz et al.* 1986; *Reme et al.* 1994). *Gombosi* (1987) introduced a typical ion-neutral collision scale linked to the charge-exchange

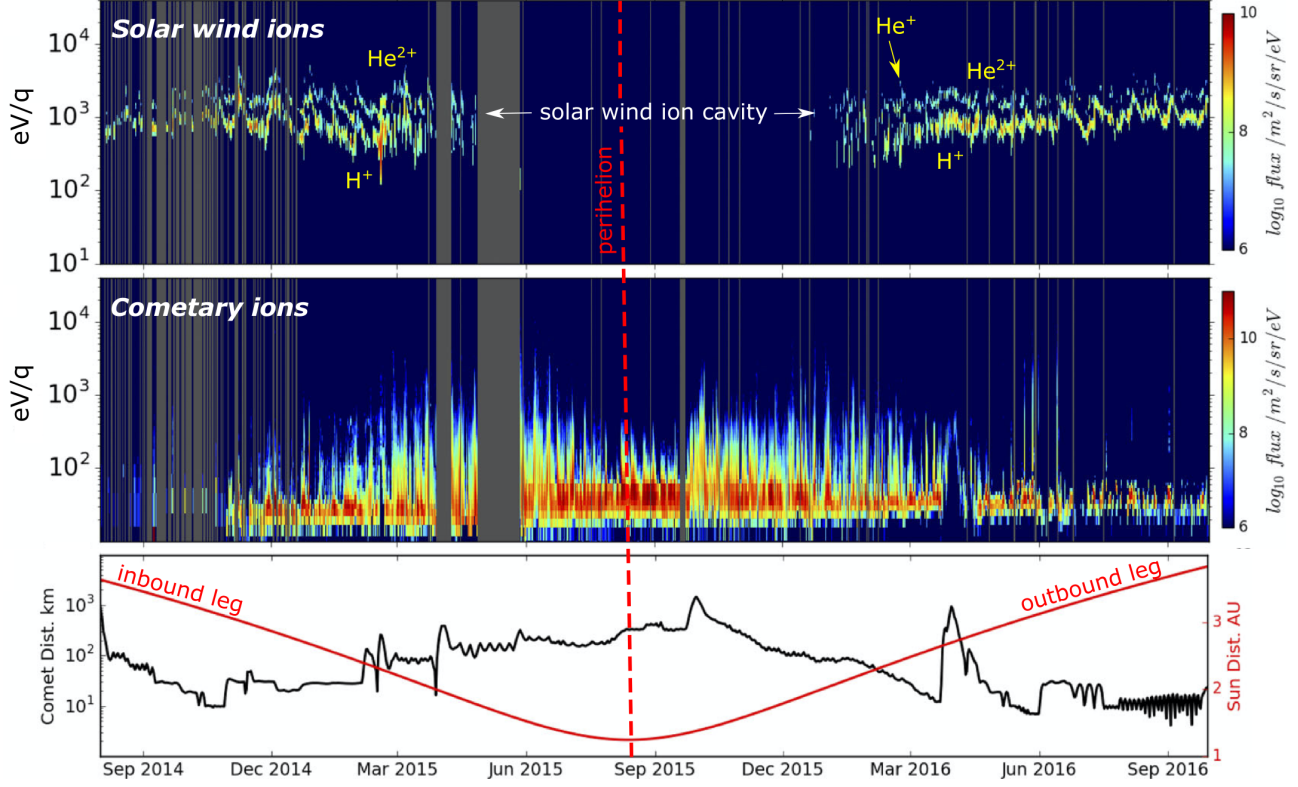


Fig. 13.— Overview of the solar wind (top) and cometary ion (middle) energy spectrograms during the Rosetta mission, as measured by RPC-ICA and angle-integrated over 1 hour. Heliocentric and cometocentric distances are shown for reference on the bottom panel. At this low temporal resolution, solar wind protons (around  $E_p/q \sim 1$  keV  $q^{-1}$ ) and alphas (around  $2E_p/q$  energy, fourfold heavier but doubly-charged) can be clearly identified, whereas charge-exchange products  $\text{He}^+$  (around  $4E_p/q$ ) are more seldom seen. The *solar wind ion cavity* spans April-December 2015, with no detection of solar wind ions during that period. Data gaps are highlighted as grey zones. Note that the colour bars on the first two panels do not have the same upper bounds. (Adapted from Fig. 1 of Nilsson *et al.* 2017).

collisionopause (definition [1]):

$$\ell_{\text{CX}} = \frac{\sigma_{p,s}^{\text{sw,CX}}(E_{\text{sw}}) Q}{4\pi V_p} \quad (67)$$

resulting, from the point of view of the ion composition, in the conversion of fast (but already decelerated) light solar wind ions  $sw$  to slow heavy cometary ions. For a solar wind speed of  $300 \text{ km s}^{-1}$ , a charge-exchange cross section of protons in water of  $2 \times 10^{-19} \text{ m}^2$  (Simon Wedlund *et al.* 2019c),  $Q \sim 10^{26}\text{--}10^{30} \text{ s}^{-1}$  (representative of activity levels of 67P and 1P), and  $V_p \sim 600 \text{ m s}^{-1}$ ,  $r_c \lesssim \ell_{\text{CX}} \lesssim 2.5 \times 10^4 \text{ km}$ . In turn, the subsolar position of the cometopause was defined by Gombosi (1987) as:

$$R_{\text{CX}} \sim \sqrt{\ell_{\text{CX}} r_0} \quad (68)$$

where  $r_0$  is the distance at which the flow speed of the shocked solar wind ions decreases down to the mean solar wind proton thermal speed. This is due to solar wind mass-loading behind the bow shock once the latter has formed (and which is situated thousands of kilometres upstream of the nucleus). In the case of 1P,  $r_0 \sim 1.6 \times 10^5 \text{ km}$ , so that

$R_{\text{CX}} \sim 6 \times 10^4 \text{ km}$ , possibly consistent with off-Sun-comet-axis Giotto and Vega-2 observations around  $1.5 \times 10^5 \text{ km}$  along their respective path (Gombosi 1987). At 67P around perihelion ( $Q \sim 5 \times 10^{27} \text{ s}^{-1}$ ), numerical hybrid simulations predicted  $R_{\text{CX}} \geq 800 \text{ km}$  using definition [2] to image the density cross-over (Simon Wedlund *et al.* 2017; Alho *et al.* 2021) with  $\ell_{\text{CX}} \sim 130 \text{ km}$  (from Eq. 67), which implies  $r_0 \sim 5000 \text{ km}$  (calculated by inverting Eq. 68).

Two intimately intertwined aspects drive the evolution of the total plasma ion composition: cometocentric distance on the one hand, and outgassing rate on the other (for a description of the cometary ion composition, see Section 2.4.2). The more the coma shrinks as the result of a smaller outgassing rate, the deeper into the coma must a given spacecraft venture to observe a relatively comparable ion composition. As a rule,  $\text{H}_2\text{O}^+$  and  $\text{CO}_2^+$  are the most prominent cometary ion species in the inner ionosphere whatever the outgassing rate, provided that we are at a sufficient distance from the nucleus, typically above  $R_{s,n} \sim R_{\text{CX}}$  (see Eq. 45 and Section 2.4.2). Let us illustrate this with two examples from the Rosetta mission: one at large heliocentric distance (low outgassing), one near perihelion

ihelion (high outgassing). What would a mass spectrometer see? As a guide, typical ion spectrograms, captured during the Rosetta mission, of the solar wind ions and of the cometary ions are displayed in Fig. 13.

From the start of the activity to medium activities, the neutral outgassing rate of a typical Jupiter-family comet (Lowry *et al.* 2008), such as 67P, is of the order of  $10^{25}$ – $10^{26}$  s<sup>-1</sup> (see Fig. 2 or Coates and Jones 2009; Hansen *et al.* 2016). Under such conditions,  $R_{CX} \sim r_c$  and solar wind ions are expected to have energy and momentum fluxes (although not necessarily densities) at least equal to those of cometary ions, as they pass almost undisturbed through the comet environment, with minimal mass-loading effects such as deflection and slowing down. However, the onset of magnetospheric-like behaviours, with the production of cometary pickup ions and sporadic solar wind charge-exchanged products, such as He<sup>+</sup>, can already be seen from  $Q \geq 10^{26}$  s<sup>-1</sup>, as demonstrated by Rosetta’s ion energy spectrograms (from RPC-ICA and RPC-IES) during both inbound and outbound conditions (Nilsson *et al.* 2015, 2017; Goldstein *et al.* 2017; Simon Wedlund *et al.* 2019b). Of note, negatively charged H<sup>-</sup> ions, thought to be arising from double charge exchange of solar wind protons, were also observed in the electron channel of RPC-IES (Burch *et al.* 2015). Thus, a lot of the total ion energy and momentum flux is still contained in the solar wind ions at relatively small cometocentric distances (Williamson *et al.* 2020), such as those probed by Rosetta ( $r \leq 150$  km). From Rosetta’s point of view, the cometopause transition, seen as a gradual flux cross-over between cometary and solar wind ions, occurred for  $Q \approx 2$ – $5 \times 10^{26}$  s<sup>-1</sup>, that is, in and around January 2015 (inbound leg of 67P’s orbit around the Sun) and February 2016 (outbound leg) (see chapter of Götz *et al.* in this volume).

At medium-to-high outgassing activity, typically for  $Q \gtrsim 10^{27}$  s<sup>-1</sup>, corresponding to closing in on perihelion conditions for 67P,  $R_{CX} \gtrsim 500$  km, and the angular deflection of the solar wind ahead of the obstacle may become so large that the solar wind is effectively kept from entering the inner coma. This region, where no solar wind ions can be detected outside of occasional solar wind-driven events, such as CMEs, was dubbed by the Rosetta team the *solar wind ion cavity* (SWIC). Rosetta stayed in this region from around April to December 2015 (Behar *et al.* 2017, and see Fig. 13). In it, the heavier, slower plasma of cometary origin, produced locally by photoionisation and electron impact ionisation, dominated the total ion composition and fluxes. Hence, for these relatively high outgassing rates, Rosetta was always inward of the cometopause, with the SWIC possibly being its inner edge (Mandt *et al.* 2019). This is mainly because: (i) Rosetta orbited close to the comet at any given time ( $< 500$  km outside of temporary excursions); (ii) RPC-MIP and RPC-LAP, instruments measuring  $n_{ci}$ , could not probe plasma densities below  $\sim 50$  cm<sup>-3</sup>. As the solar wind density is typically  $n_{sw} \approx 1$ – $10$  cm<sup>-3</sup>, it was not possible to locate where  $n_{sw} \approx n_{ci}$ . Thus, in a way similar to onions, the

cometopause successively encompasses the ion-neutral and electron-neutral collisionopauses, where plasma-neutral collisions start to play a major role in the coma, but also the diamagnetic cavity once it forms. For more discussion on the formation of large-scale boundaries including the cometopause, the diamagnetic cavity, the collisionopauses, and the solar wind ion cavity, the reader is directed to the chapter by Götz *et al.* in this volume.

## 5. Dusty (dirty) complex plasma

When we look at a comet in the night sky, our eyes mostly detect sunlight reflected by dust grains emitted from the comet nucleus, forming the coma and the dust tail (usually the more visible of the two tails, see the chapter by Agarwal *et al.* in this volume). This obvious presence of dust in the same volume of space as the cometary plasma immediately suggests that the coma and dust tail may be regions where there are lots of interaction between the dust and the plasma. The plasma may charge the dust, which in turn can influence the motion of the plasma, coupling them together in what is known as a *dusty* or *complex plasma*.

In this section, we will only provide a very limited introduction to the range of possible effects of dust-plasma effects at comets (Section 5.1) and to the mechanics of dust charging (Section 5.2). The main reason for spending so little space on this is very simple: In contrast to the dust-free physics of a cometary ionosphere, presented in this chapter until now, and against many expectations before the mission arrival at 67P, the analysis of the Rosetta data has as yet not provided any entirely new picture of dust-plasma interactions at comets. As we will see in Section 5.3, some dust-plasma interaction signatures have been identified in the Rosetta data. But the same Section will show that the rich Rosetta data sets on plasma and cometary dust actually suggest such interactions probably have only a small impact on the plasma, at least for most of the mission and for the regions visited around this particular comet. For a more extensive treatment of dust charging and its possible effects on the comet plasma environment, we refer to previous literature on the subject (see for example Mendis and Horányi 2013).

### 5.1. Why care about dust charging?

Consider free electrons moving around in the coma. If there are lots of dust grains, an electron might now and then hit one of the grains, perhaps knocking out one electron (in the process known as *secondary emission*) and thereby increasing the number of *free* electrons and charging the dust grain positively. The dust grain would then effectively become an enormously heavy positive ion. Alternatively, the impacting electron might stick to a dust grain, decreasing the number of free electrons and charging the dust negatively. The charge acquired on the dust grain suddenly couples it to the electromagnetic fields around it, and it will itself influence these fields and thereby other charges. Both plasma and dust interact as seen in Fig. 14.

Two main effects may ensue from dust charging and variations in the number density of free electrons. The first one affects the collective behaviour of the plasma and its wave modes, such as the frequency at which it naturally pulsates,  $\omega_{pe} \propto \sqrt{n_e}$  (see Eq. 53). One can show that the decrease in the free-electron number density due to attachment to dust grains changes the dispersion relation of *ion acoustic waves* in such a way as to push them to higher frequency, also decreasing their Landau damping (Barkan *et al.* 1996). It also allows a completely new wave mode, known as *dust acoustic waves*, which, because of the huge dust grain inertia, propagates much slower than usual plasma waves (Merlino 2014). Moreover, electromagnetic modes can be influenced as the charged dust provides the plasma with a higher inertia, and with a continuous distribution of dust masses: This may be interpreted as a continuum of cyclotron resonances. However, due to the large dust grain mass (see the chapter by Engrand *et al.* in this volume for a discussion of dust size distribution) and weak magnetic field (of the order of 10 nT) at a comet outside 1 au, the effects on electromagnetic waves are expected only at very low frequency such as to not be of practical relevance. Consequently acoustic modes are the most relevant wave modes at comets. For a discussion of the physics related to cometary plasma waves (albeit not dust-related), see the chapter by Götzt *et al.* in this volume.

But dust charging can also affect the dynamics of the dust. From the point of view of cometary evolution, the most important of these effects is the so-called *levitation*, in which dust grains can be expelled from the cometary nucleus by electrostatic repulsion if they and their immediate neighbourhood are charged negatively when bombarded by electrons from the surrounding plasma. This effect could potentially be important as it may increase the nucleus dust production from the surface. We refer to the chapter by Agarwal *et al.* in this volume for further discussion on processes that lift off dust grains from the nucleus. In contrast, farther out from the nucleus' surface, a charged dust grain is subject not only to the forces of gravity and radiation pressure (i.e. a momentum transfer between the impacting solar photons and atoms, molecules, and dust grains in the coma) acting on any grain, but also to the electromagnetic fields in the plasma. Due to the large dust grain inertia, fields acting over large scales in space and time are most significant: We will see below that this effect actually was observed in situ by Rosetta. In addition, the attachment of charges (electrons) to a dust grain causes a repelling electrostatic force between various parts of the grain itself. This force may contribute to erosion of the grain, either by more or less continuous ablation with small fractions of the grain splitting off or fragmentation, when the grain breaks in two (or more) pieces of approximately the same size. Note, however, that other processes may also lead to the same result (see the chapter by Engrand *et al.* in this volume).

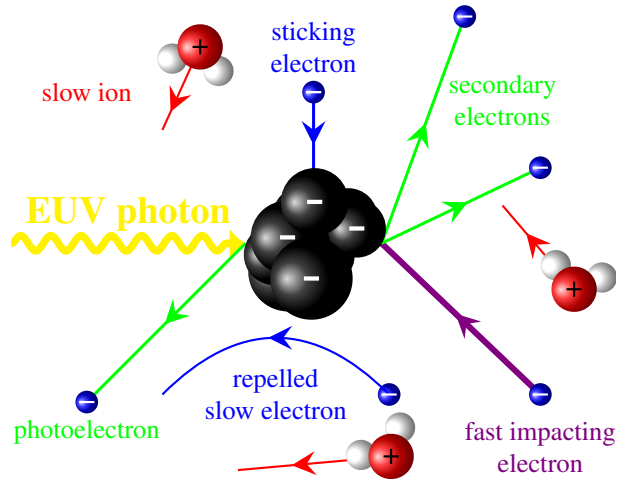


Fig. 14.— Schematic of various effects influencing the charging of a dust grain (conglomerated black spheres).  $n_i$  and  $n_e$  are assumed equal within the figure (not every ion or electron is represented) but the higher thermal speed of the electrons leads to more hits on a dust grain thereby charging the grain negatively when impacting electrons stick to the grain. Sufficiently energetic free electrons (magenta line) and solar EUV photons (yellow) can kick out electrons from the grain (green lines), gradually shifting the total charge towards positive values and leading to a non-uniform charging of the grain.

## 5.2. Dust charging

What are the effects influencing the charge of a dust grain? As discussed earlier, a plasma consists of free charges, positive and negative, moving around at random velocities distributed in accordance with their temperatures ( $T_s$  for ion species  $s$  or  $T_e$  for free electrons) and masses ( $m_s$  and  $m_e$ ). One of their typical speeds is the thermal speed  $v_{th} = \sqrt{k_B T/m}$  corresponding to the *standard deviation* around their mean bulk velocity  $\mathbf{V}$ . Ions and electrons have masses which differ by about 4 orders of magnitude ( $m_s/m_e \sim 3.3 \times 10^4$  for water-group ions, typical for a cometary coma), while their temperatures are usually alike. In addition, in the inner cometary ionosphere,  $|\mathbf{V}_s| \gg v_{th,s}$  for ions whereas  $|\mathbf{V}_e| \ll v_{th,e}$ . As a consequence, electrons typically move much faster (typically a few hundred times faster) than ions such that in a given time span, a dust grain (or any ‘body’ in the ionised cometary gas) will be hit more frequently by electrons than by ions. The grain thus preferentially charges negatively, until reaching an equilibrium potential  $V_d$  sufficient to stop further charging by repulsion of electrons and catching of ions. This potential can be estimated as:

$$V_d \sim -\frac{3k_B T_e}{q} \quad (69)$$

It can be noted that these considerations for dust grains apply similarly to a spacecraft, so that the spacecraft potential (discussed in Section 3.1.1) is in principle set by a similar

equation. However, analysis and modelling have shown that due to the design of the Rosetta spacecraft, its electrostatic potential in the inner coma was rather determined by the plasma density (*Johansson et al.* 2021).

From the grain potential  $V_d$ , we can calculate its charge:

$$q_d = C_d V_d \quad (70)$$

where  $C_d$  is the dust's capacitance. The latter can be estimated, or at least a minorant may be found, by considering a spherical grain of radius  $r_d$  in vacuum such that

$$C_d = 4\pi\epsilon_0 r_d \quad (71)$$

Therefore, if all grains have the same size and are all spherical, the total charge density  $\rho_d$  (in  $\text{A s m}^{-3}$ ) carried by the dust is obtained by combining Eqs. 69–71:

$$\rho_d = q_d n_d \sim -12\pi\epsilon_0 r_d n_d k_B T_e / q \quad (72)$$

where  $n_d$  is the number of dust grains per unit volume.

In reality, the attachment of free electrons is not the only factor influencing the grain potential (Figure 14). The emission of electrons from sunlit dust grains due to the photoelectric effect will tend to charge the grains positively whereas, if the impacting flux of free electrons is sufficiently high, the negative charging by electrons attaching to grains will dominate. In practice, the limiting density is on the order of  $10^2 \text{ cm}^{-3}$  at 1 au (scaling with  $r_h^{-2}$ ), depending on the dust grain properties. In the dense parts of a coma, we expect to find mainly negatively-charged dust grains. Another major effect is secondary emission, occurring when an electron of sufficiently high energy kicks out one or more electrons from a grain. It is typically important when the incoming electron has an energy of  $\sim 100$  eV and does not matter much below 10 eV, although this depends on the detailed dust properties, often not very well known (size and mass distributions, shape, composition).

A further complicating factor is the time it takes to charge a dust grain to its equilibrium potential  $V_d$  (Eq. 69). The total electric current collected by the grain  $I_e$  [A], due to the randomly moving plasma and mainly driven by the free electrons, is approximately given by  $I_e \approx J_e S_d$  where  $S_d = 4\pi r_d^2$  [ $\text{m}^2$ ] is the grain surface and  $J_e$  [ $\text{A m}^{-2}$ ] is the electron thermal current density, driven by free electrons moving towards the grain.  $J_e$  is given by (e.g. *Mott-Smith and Langmuir* 1926):

$$J_e = -qn_e \sqrt{\frac{k_B T_e}{2\pi m_e}}. \quad (73)$$

Determining  $q_d$  as a function of time requires solving a differential equation, exactly as for a resistor–capacitor circuit. The characteristic time, or time constant, for charging a dust grain from 0 to  $V_d$  is given by:

$$\mathcal{T}_d \sim \frac{C_d V_d}{I_e} = 3\epsilon_0 \frac{\sqrt{2\pi m_e k_B T_e}}{n_e q^2 r_d} = 3\sqrt{2\pi} \frac{\lambda_{\text{Debye}}}{r_d \omega_{p,e}} \quad (74)$$

where  $\lambda_{\text{Debye}}$  and  $\omega_{p,e}$  are defined by Eqs. 53–54. Each dust grain can be seen as a capacitor and a resistor in series with its characteristic capacitance  $C_d$  and resistance  $R_d = V_d/I_e$  [ $\Omega$ ], depending not only on their size and shape but also on the local electron number density and temperature. The current is provided to this circuit by means of free electrons in the plasma falling on the dust grain. From Eq. 74, we note that large grains charge up faster than small ones (as  $C \propto r_d$  and  $I_e \propto r_d^2$ , bigger grains collect more electrons). Only one of the most relevant dust charging processes at comets has been described here and a more exhaustive description is given in *Meyer-Vernet* (2013).

How long does a dust grain take to reach  $\sim V_d$  for typical cometary plasma parameters? For a grain of radius  $r_d = 10 \mu\text{m}$  in a plasma with  $n_e = 10^3 \text{ cm}^{-3}$  and  $T_e = 10 \text{ eV}$ , we get  $\mathcal{T}_d \sim 10 \text{ s}$ , while a 100-nm ‘nanograin’ requires  $\sim 10^3 \text{ s}$  (more than 15 minutes). During this time, the grain may travel through plasmas of quite varying characteristics, particularly in the inner coma (see the chapter by Agarwal et al. in this volume and *Marschall et al.* 2020, for discussions of dust grain velocities). At some distances, the different  $\mathcal{T}_d$  between grains associated with the outward dust flow through a plasma such that  $n_e(r) \propto 1/r$  can lead to complex situations where small grains may conserve the negative charge acquired closer to the nucleus (long  $\mathcal{T}_d$ ) while larger grains may quickly charge positively by means of photoemission (short  $\mathcal{T}_d$ ). In addition, the secondary emission, which tends to be more efficient for small grains, can lead to similar results. As dust grains may travel at different speeds and take different trajectories through the plasma, they experience different charging along their path. All this leads to an expectation of a distribution of charge states even for similar dust grains – and, as is clear from the chapter by Engrand et al. in this volume, there is a large variation among dust grain properties.

In these circumstances, is it possible to estimate the fraction of the free electrons which will attach to dust grains? This is an important question, because this fraction must be significant in order for the dust charging to have any considerable effect on the plasma. Clearly, the answer must depend on  $n_e$  and  $n_d$ . However, the dust size distribution is also crucial in this respect. For example, let's assume that all dust grains have the time to reach their equilibrium potential as given by Eq. 69. The charge carried by a grain depends on its capacitance, which scales linearly with its size (as seen in the example of a sphere, Eq. 71). Contrarily, the mass of a grain scales with its volume  $\mathcal{V}_d \propto r_d^3$ . As a consequence, for a fixed total dust mass, the plasma is more depleted in free electrons and dust charging is more efficient if the dust is mostly made of lots of small grains than of a few large ones (*Vigren et al.* 2015). For a given dust size distribution, detailed calculations can be used to estimate the total amount of dust charging.

As the size distribution of dust in the innermost coma of comet 67P is quite well constrained by the dust instruments (see the chapter by Engrand et al. in this volume), *Vigren et al.* (2021) carried out such calculations and constrained



the possible electron depletion in this environment. Their model, combining observed plasma densities and electron energies with dust size distributions derived from the dust observations at Rosetta by means of Eq. (72), shows that because of the preponderance of large grains, the fraction of electrons attaching to dust grains must have been small or even negligible during most parts of the Rosetta mission. Quite extreme assumptions on the dust distribution had to be taken even to push the electron depletion to a few percent. A similar negative conclusion was reached by *Vigren et al.* (2022), using analogous arguments, for positive charging of dust grains.

There may be exceptions at specific locations and times, as in outbursts (see, for example, the 2016 Feb 19 event studied by *Grün et al.* 2016) which could lead to a locally high density of small grains, though no clear signatures of obvious electron depletion have yet been identified in the Rosetta data set. An apparent absorption of solar EUV radiation has also been used to argue that the dust size distribution at large distances from Rosetta (several thousand kilometres or more) may include larger amounts of grains down to the size of tens of nanometres (*Johansson et al.* 2017). As few such grains have been observed close to the nucleus, they have presumably resulted from one or several erosion and fragmentation processes (see discussion in Section 5.1 and the chapter by Engrand et al. in this volume) which possibly could lead to stronger dust-plasma coupling farther from the nucleus than the regions investigated by Rosetta. One may note that very small dust grains, with masses down to  $10^{-23}$  kg, were observed by the Vega spacecraft  $\sim 10^5$  km from the nucleus of comet Halley (*Sagdeev et al.* 1989).

While there may still be much to learn from the Rosetta data set, the combination of the observed average properties of dust and plasma quite clearly indicates that the typical electron depletion in the innermost coma of 67P is small, with correspondingly weak impact of the dust on the overall plasma dynamics. However, charged dust grains of very small size were indeed observed in some events, as discussed in Section 5.3.

### 5.3. Charged dust dynamics at Comet 67P

How do charged dust grains move in the coma? Let us start by considering neutral dust grains. Close to the nucleus, the grain is dragged by the outflowing cometary gas. As the neutral gas density decreases with cometocentric distance (see Eq. 3), the neutral drag force decays rapidly with distance and is hence stronger close to the nucleus. The very weak gravitational force of a comet nucleus can also mostly be neglected for most dust grains farther outside (however, see *Davidsson et al.* 2015, for examples of gravitationally bound dust motion around comet 67P). In addition, the solar radiation pressure impresses a constant force on every grain in the anti-sunward direction. Grains emitted from the nucleus in the direction of the Sun can therefore be turned back by the radiation pressure and re-

turn towards the nucleus and farther out downstream of the comet. The radiation pressure force on a grain depends on  $r_d^2$ , while the inertia scales with its volume, through its mass, which is  $\propto r_d^3$ . Therefore, the radiation pressure affects more efficiently the dynamics of small/light grains than that of large/heavy grains. Other effects, such as Mie scattering and Poynting–Robertson drag, are not discussed here: Fuller details are given in *Burns et al.* (1979).

Charged grains are, in addition, subject to electromagnetic forces arising in the comet-plasma interaction, discussed in the chapter by Götz et al. in this volume. Due to the large mass of dust grains, compared with cometary ions and electrons (in the gas phase) (even a small 10 nm grain are estimated to have a mass of order  $10^5$  u by *Gombosi et al.* 2015), the gyroradius of dust grains generally becomes so large that the grain’s gyromotion can be neglected within the inner coma explored by Rosetta at 67P. Nevertheless, the magnetic field indirectly leads to the appearance of a convection electric field which may efficiently affect the dust dynamics. If this force is constant over the region traversed by the dust grain, the dust’s trajectory will describe a parabola of which its axis of symmetry is along this force. However, electric and magnetic fields change in time, and, as aforementioned in Section 5.2, the charge of a grain may evolve as well, as it travels through plasma regions of different  $J_e(\mathbf{r})$ , while grains eventually erode and/or fragment which yields changes in the dust’s mass, size, charge, and number. Therefore, the picture of motion in a conservative field must be applied with caution.

The RPC-IES spectrometer was designed for the measurement of (positive) ions and electrons. However, it was able to detect charged dust grains. As there was no possibility for direct mass separation, charged dust signatures could not be unambiguously separated from those of ions and electrons by IES. That said, some signatures stand out from ordinary charged particle signatures and better fit to expectations for charged dust. *Burch et al.* (2015) found a few events with negatively charged grains moving outward from the nucleus at kinetic energies of a few hundreds of eVs (if assumed to be singly-charged; higher charge states would have correspondingly higher energy) as well as much more energetic grains ( $1\text{--}17$  keV  $q^{-1}$ ), also negatively charged, arriving from the approximate Sun’s direction. All these detections were from the very early phase of the Rosetta escort of 67P, from 23 August to 1 September 2014, when Rosetta was at 50–60 km sunward of the nucleus and the outgassing activity was still very low. *Gombosi et al.* (2015) analysed the observations of outward moving grains in terms of neutral gas drag acceleration. The anti-sunward moving grains were attributed to radiation pressure acting on small grains likely created from larger grains by erosion at large distances from the nucleus. For both types of grains, consistency between model and data resulted for grains’ sizes within the 30–80 nm range. The convection electric field, changing in time in response to the interplanetary magnetic field, was discussed as a possible reason for the intermittency of the observations, deviating grains from the densest

regions away or towards Rosetta.

*LLera et al.* (2020) could identify another event, for a similar period (19 Sep 2014), with positively-charged and negatively-charged grains over a broad energy range, as expected from the competing charging processes discussed in Section 5.1. Both showed signatures very similar to the negatively charged antisunward moving grains previously reported. Interestingly, while grains of both signs had an antisunward velocity component, their trajectory was symmetric with respect to the antisunward component. This is what is to be expected for charged dust grains subject to a combination of the solar radiation pressure, same for both signs, and the solar wind convection electric field in the comet reference frame, which accelerates grains of opposite charge in opposite directions.

These are, as yet, the only events with signatures which have been attributed to charged dust grains in the tens of nm-size range, all from the initial part of the Rosetta mission. Why are there so few? Regarding the outflowing grains discussed by *Burch et al.* (2015), their signature is quite weak and may be swamped with electron fluxes in the same range, which were significant through most of the mission. The higher energy signature of the (roughly) antisunward grains should not suffer as much, and here it seems likely they are just not present in significant numbers in the inner coma. According to the interpretation by *Johansson et al.* (2017) of anomalously low flux of solar radiation in the EUV observed at Rosetta around perihelion when 67P's activity peaked, nm-size dust grains were mainly present at cometocentric distances of at least a few thousand kilometres during this period. This may point to the fragmentation of dust grains occurring farther out at high activity than at low activity. Alternatively, the dust itself may already have different properties depending on  $Q$  and  $r_h$ .

Rosetta has as yet only showed some tantalising glimpses of dust-plasma interactions, concentrated on the early phase of very low activity, while mission wide modelling indicated that the dust impact on the plasma mostly is small or negligible. Nevertheless, the Rosetta data set are far from exhausted and may still hold more clues to the presence and importance of dust charging.

## 6. Summary & open questions

Prior to the 1980s, comets and their plasma environment had relied only on speculation and simulation work, either in the laboratory or starting with the first numerical simulations. Thanks to the historical missions that followed, from the first flybys of comets in the 1980s to Rosetta's 2-year mission escorting comet 67P around the Sun 30 years later, many questions regarding the ionosphere of comets, its formation, structure and evolution at different outgassing activities have now been answered. Table 2 presents highlights of our current understanding sorted by the themes structuring this chapter, from the physics presiding at the creation of a cometary ionosphere (Section 2, presented as a tutorial-style toolbox), the description of the plasma pop-

ulation, electrons (Section 3) and ions (Section 4), and the puzzling and still largely unexplored role of charged dust in the overall dynamics and composition of the cometary ionosphere (Section 5).

Many open questions remain, some of the more prominent ones are summarised in Table 3. With the advent of new missions, several of these questions will hopefully be answered. Ideally, multi-point, multi-instrument, in situ exploration of the cometary coma, either through a flyby or an extended escort phase of the comet nucleus “à-la-Rosetta”, are necessary to address them with more than one spacecraft if possible as already proposed by the community for the ESA Voyage 2050 programme call for white papers (*Goetz et al.* 2021). This is among the goals of the highly anticipated ESA/JAXA *Comet Interceptor* mission (*Snodgrass and Jones* 2019), currently in-the-works as an international endeavour: boasting simultaneous 3-point measurements thanks to a mother spacecraft A complemented by two smaller probes, B1 and B2, the mission is planned to be launched in 2029 and to fly by a ‘dynamically new comet’ yet to be discovered (that is, visiting our inner Solar System for the first time). Of particular interest for cometary ionospheric physics, probe A, farthest from the cometary nucleus, hosts a Dust, Field, and Plasma (DFP) set of sensors to probe the dust, electromagnetic fields, (dusty) plasma and energetic particles (electrons, ions, and neutral atoms). This set is complemented by a neutral pressure gauge and mass spectrometer probing the major volatile species (MANiAC). On probe B2 which will get closest to the cometary nucleus, the DFP package is reduced to a dust impact sensor and counter, and a magnetometer. Probe B1 hosts a plasma suite, which includes a time-of-flight mass spectrometer and a magnetometer. All these sensors will be probing the plasma environment around the target to deepen our understanding of cometary ionospheres, including formation, loss, and interaction with the space environment.

No new dedicated cometary mission, with sample return or not, is envisaged in the decade following Comet Interceptor, despite a strong call from the community, as proposed for the ESA Voyage 2050 programme call (*Bockelée-Morvan et al.* 2021; *Goetz et al.* 2021). Because of their complexity, costs, and necessary multidisciplinary approach, future cometary missions will likely be international collaborations between space agencies (as for Comet Interceptor) and address a broad range of physics including plasma physics. By escorting comet 67P around perihelion for two years, Rosetta is a successful proof of concept showing that a spacecraft orbiting a comet for a long period of time can be designed, flown, and can harvest an amazingly rich dataset, despite the weak nucleus gravity. With our increasing capacity to detect more and more new targets of interest, interstellar objects or not, one can envision multiple flybys during an extended mission phase, with several small-scale missions, like Comet Interceptor or along the lines of the original Halley Armada. The next passage of comet 1P/Halley in our vicinity in 2061, together with other comets from different reservoirs, may provide an

interesting window of opportunity.

### **Acknowledgments.**

We would like to warmly thank P. Stephenson (Imperial College London, UK) and G. Wattiaux (Université of Toulouse, France) for their help and support, in particular in providing un/processed dataset shown in Fig. 6 and in generating Fig. 11, respectively. We warmly thank Z. Lewis for her careful reading of the chapter and her suggestions. A.B. and his work at Umeå University was supported by the Swedish National Space Agency (SNSA) grant 108/18. C.S.W. thanks the Austrian Science Fund (FWF) P32035-N36. Work by M.G. at Imperial College London was supported in part by STFC of UK under grant ST/W001071/1.

Topic	Highlights
Birth of cometary ionosphere:	<ul style="list-style-type: none"> <li>• Identification of ionospheric sources and losses, and of their relative contribution, for different outgassing activities (Section 2.2.4)</li> <li>• CMEs/CIRs impact on the ionospheric sources and densities (Sections 2.2.4 and 2.4.1)</li> <li>• Plasma density profile observed all the way down to the surface (Section 2.4.1)</li> <li>• First detection &amp; confirmation of ion species (up to 39 u/q); Evolution of the ion composition over heliocentric distance and season (Section 2.4.2)</li> </ul>
Electron population:	<ul style="list-style-type: none"> <li>• Three populations confirmed: cold, warm, and hot (Section 3.1)</li> <li>• Symbiosis between the three populations: coexist and are dependent on each other (Section 3.1)</li> <li>• Hot electrons: Similarities with auroral Physics at Earth (Section 3.1.3)</li> <li>• Detection of cold electrons even when the coma is quasi-collisionless (Section 3.1.2)</li> <li>• Evidence of the role played by electrons in the location of the diamagnetic cavity boundary (see Section 3.3)</li> </ul>
Ion population:	<ul style="list-style-type: none"> <li>• Three populations: slow cometary ions, early picked-up cometary ions, solar wind ions (Sections 4.2 and 4.3)</li> <li>• Evidence of chemistry (ion-neutral collisions) taking place in the coma (Sections 2.4.2 and 4.1)</li> <li>• Evidence for accelerated cometary ions (Sections 3.2 and 4.1)</li> <li>• Cometary ion density (but not flux) dominating over that of solar wind ions even at very low outgassing rate (Section 2.2.4)</li> </ul>
Dusty plasma:	<ul style="list-style-type: none"> <li>• No evidence yet of a dusty plasma at comet 67P with Rosetta (Section 5.3)</li> <li>• Observations of a few events of charged dust grains, positive and negative (Section 5.3)</li> </ul>

Table 2: Highlights of this chapter on cometary ionospheres

#### Open questions

##### **Birth of cometary ionosphere:**

- What is the plasma balance near perihelion? What are the key plasma source and loss?
- What is the 3D distribution of the ionospheric densities under different outgassing activities?
- What is the composition of heavy ions ( $>40 \text{ u q}^{-1}$ )?
- What is the change, if any, of the ion composition in different plasma regions and boundaries?
- What is the role played by the dust regarding EUV absorption under high activity?

##### **Electron population**

- What is the energy distribution of electrons at high temporal and energy resolutions? How does it vary in space?
- What is the exact origin of cold electrons in a quasi-collisionless coma?
- What is the role of cold electron in the presence of a diamagnetic cavity?
- What is the source of hot electrons at high activity, when a diamagnetic cavity is formed?

##### **Ion population:**

- What is the energy distribution of cometary, slow ions?
- Are ions accelerated near the surface at high activity and, if so, what is the process responsible for it?
- What is driving the cometary ion dynamics ?
- What is the exact role of electrons on the ion acceleration?
- How to reconcile the observed high ion bulk speeds and the observed electron densities explained by a model excluding ion acceleration?
- How to reconcile the observed high ion bulk speeds and the observed ion composition attesting of ion-neutral chemistry in the coma?

##### **Dusty plasma:**

- Does dust have significant impact on the cometary ionosphere for more active comets?
- Are dusty plasma interactions the same at all comets and, if not, what are the conditions driving those effects?

Table 3: Non-exhaustive list of open questions regarding cometary ionospheres.

## REFERENCES

- Aikin A. C. (1974) *Cometary coma ions*, *The Astrophysical Journal*, 193, 263.
- Alho M., Jarvinen R., Simon Wedlund C. et al. (2021) *Remote sensing of cometary bow shocks: modelled asymmetric outgassing and pickup ion observations*, *Mon. Not. R. Astron. Soc.*, 506, 4735–4749.
- Allen M., Delitsky M., Huntress W. et al. (1987) *Evidence for methane and ammonia in the coma of comet P/Halley*, *Astron. Astrophys.*, 187, 502–512.
- Altwegg K., Balsiger H., Bar-Nun A. et al. (2016) *Prebiotic chemicals—amino acid and phosphorus—in the coma of comet 67P/Churyumov-Gerasimenko*, *Science Advances*, 2, e1600285–e1600285.
- Altwegg K., Balsiger H., Geiss J. et al. (1993) *The ion population between 1300 km and 230000 km in the coma of comet P/Halley*, *Astron. Astrophys.*, 279, 260–266.
- Auger P. (1923) *Sur les rayons  $\beta$  secondaires produits dans un gaz par des rayons x.*, *Comptes rendus hebdomadaires des séances de l'Académie des sciences.*, 177, 169.
- Balsiger H., Altwegg K., Benson J. et al. (1987) *The ion mass spectrometer on Giotto*, *Journal of Physics E: Scientific Instruments*, 20, 759–767.
- Balsiger H., Altwegg K., Bochsler P. et al. (2007) *Rosina – rosetta orbiter spectrometer for ion and neutral analysis*, *Space Science Reviews*, 128, 745–801.
- Balsiger H., Altwegg K., Bühler F. et al. (1986) *Ion composition and dynamics at comet halley*, *Nature*, 321, 330–334.
- Barkan A., D'Angelo N., and Merlino R. L. (1996) *Experiments on ion-acoustic waves in dusty plasmas*, *Planet. Space Sci.*, 44, 239–242.
- Behar E., Nilsson H., Alho M. et al. (2017) *The birth and growth of a solar wind cavity around a comet - Rosetta observations*, *Mon. Not. R. Astron. Soc.*, 469, S396–S403.
- Bercic L., Behar E., Nilsson H. et al. (2018) *Cometary ion dynamics observed in the close vicinity of comet 67P/Churyumov-Gerasimenko during the intermediate activity period*, *A&A*, 613, A57.
- Bergman S., Stenberg Wieser G., Wieser M. et al. (2020) *The Influence of Varying Spacecraft Potentials and Debye Lengths on In Situ Low-Energy Ion Measurements*, *Journal of Geophysical Research (Space Physics)*, 125, e27870.
- Bergman S., Stenberg Wieser G., Wieser M. et al. (2021) *Ion bulk speeds and temperatures in the diamagnetic cavity of comet 67P from RPC-ICA measurements*, *Monthly Notices of the Royal Astronomical Society*, 503, 2733–2745.
- Beth A., Altwegg K., Balsiger H. et al. (2017) *First in situ detection of the cometary ammonium ion  $NH_4^+$  (protonated ammonia  $NH_3$ ) in the coma of 67P/C-G near perihelion*, *Monthly Notices of the Royal Astronomical Society*, 462, S562–S572.
- Beth A., Altwegg K., Balsiger H. et al. (2020) *ROSINA ion zoo at Comet 67P*, *Astron. Astrophys.*, 642, A27.
- Beth A., Galand M., and Heritier K. L. (2019) *Comparative study of photo-produced ionosphere in the close environment of comets*, *A&A*, 630, A47.
- Bhardwaj A. (2003) *On the Solar EUV Deposition in the Inner Comae of Comets with Large Gas Production Rates*, *Geophysical Research Letters*, 30.
- Bhardwaj A., Elsner R. F., Randall Gladstone G. et al. (2007) *X-rays from solar system objects*, *Planet. Space Sci.*, 55, 1135–1189.
- Biermann L. (1951) *Kometenschweife und solare Korpuskularstrahlung*, *Zeitschrift für Astrophysik*, 29, 274.
- Biermann L. (1952) in *Liege International Astrophysical Colloquia* (P. Swings, ed.), vol. 4 of *Liege International Astrophysical Colloquia*, pp. 251–262.
- Biermann L., Brosowski B., and Schmidt H. U. (1967) *The interactions of the solar wind with a comet*, *Solar Physics*, 1, 254–284.
- Biver N., Bockelée-Morvan D., Hofstadter M. et al. (2019) *Long-term monitoring of the outgassing and composition of comet 67P/Churyumov-Gerasimenko with the Rosetta/MIRO instrument*, *A&A*, 630, A19.
- Bockelée-Morvan D., Filacchione G., Altwegg K. et al. (2021) *Ambition – comet nucleus cryogenic sample return*, *Experimental Astronomy*.
- Broiles T. W., Burch J. L., Chae K. et al. (2016a) *Statistical analysis of suprathermal electron drivers at 67P/Churyumov-Gerasimenko*, *Monthly Notices of the Royal Astronomical Society*, 462, S312–S322.
- Broiles T. W., Livadiotis G., Burch J. L. et al. (2016b) *Characterizing cometary electrons with kappa distributions*, *Journal of Geophysical Research: Space Physics*, 121, 7407–7422.
- Burch J. L., Cravens T. E., Llera K. et al. (2015) *Charge exchange in cometary coma: Discovery of  $H^-$  ions in the solar wind close to comet 67P/Churyumov-Gerasimenko*, *Geophys. Res. Lett.*, 42, 5125–5131.
- Burch J. L., Goldstein R., Cravens T. E. et al. (2007) *RPC-IES: The Ion and Electron Sensor of the Rosetta Plasma Consortium*, *Space Science Reviews*, 128, 697–712.
- Burch J. L., Gombosi T. I., Clark G. et al. (2015) *Observation of charged nanograins at comet 67P/Churyumov-Gerasimenko*, *Geophysical Research Letters*, pp. 6575–6581, 2015GL065177.
- Burns J. A., Lamy P. L., and Soter S. (1979) *Radiation forces on small particles in the solar system*, *Icarus*, 40, 1–48.
- Chamberlain J. W. (1963) *Planetary coronae and atmospheric evaporation*, *Planet. Space Sci.*, 11, 901–960.
- Chapman S. (1931) *The absorption and dissociative or ionizing effect of monochromatic radiation in an atmosphere on a rotating earth*, *Proceedings of the Physical Society*, 43, 26–45.
- Chapman S. and Cowling T. G. (1970) *The mathematical theory of non-uniform gases.*, Cambridge University Press.
- Coates A. J. (2004) *Ion pickup at comets*, *Advances in Space Research*, 33, 1977–1988.
- Coates A. J., Burch J. L., Goldstein R. et al. (2015) in *Journal of Physics Conference Series*, vol. 642 of *Journal of Physics Conference Series*, p. 012005.
- Coates A. J. and Jones G. H. (2009) *Plasma environment of Jupiter family comets*, *Planet. Space Sci.*, 57, 1175–1191.
- Cowley S. W. H., McCrea W. H., Turner G. et al. (1987) *ICE observations of Comet Giacobini-Zinner*, *Philosophical Transactions of the Royal Society of London. Series A, Mathematical and Physical Sciences*, 323, 405–420.
- Cravens T. E. (1986) in *ESLAB Symposium on the Exploration of Halley's comet* (B. Battrick, E. J. Rolfe, and R. Reinhard, eds.), vol. 250 of *ESA Special Publication*, p. 241.
- Cravens T. E. (1989) *A magnetohydrodynamical model of the inner coma of comet halley*, *Journal of Geophysical Research: Space Physics*, 94, 15025–15040.
- Cravens T. E. (1997a) *Comet Hyakutake X-ray source: Charge transfer of solar wind heavy ions*, *Geophysical Research Letters*, 24, 105–108.

- Cravens T. E. (1997b) *Physics of Solar System Plasmas*, Cambridge Atmospheric and Space Science Series, Cambridge University Press.
- Cravens T. E. (2002) *X-ray Emission from Comets*, *Science*, 296, 1042–1046.
- Cravens T. E. and Gombosi T. I. (2004) *Cometary magnetospheres: a tutorial*, *Advances in Space Research*, 33, 1968–1976.
- Cravens T. E., Gombosi T. I., Gribov B. E. et al. (1984) *The role of electric fields in the cometary environment*, Tech. rep., Hungarian Academy of Sciences, kFKI–1984-41.
- Davidsson B. J. R., Gutiérrez P. J., Sierks H. et al. (2015) *Orbital elements of the material surrounding comet 67P/Churyumov-Gerasimenko*, *Astron. Astrophys.*, 583, A16.
- Deca J., Divin A., Henri P. et al. (2017) *Electron and Ion Dynamics of the Solar Wind Interaction with a Weakly Outgassing Comet*, *Phys. Rev. Lett.*, 118, 205101.
- Deca J., Henri P., Divin A. et al. (2019) *Building a Weakly Outgassing Comet from a Generalized Ohm's Law*, *Phys. Rev. Lett.*, 123, 055101.
- Dennerl K. (2010) *Charge Transfer Reactions*, *Space Sci. Rev.*, 157, 57–91.
- Dennerl K., Lisse C. M., Bhardwaj A. et al. (2012) *Solar system X-rays from charge exchange processes*, *Astronomische Nachrichten*, 333, 324.
- Deslandres H. and Bernard A. (1907) in *Comptes rendus hebdomadaires des séances de l'Académie des sciences*, vol. 145, pp. 445–448, Académie des Sciences, Gauthier-Villars (Paris).
- Eberhardt P. (1999) *Comet halley's gas composition and extended sources: Results from the neutral mass spectrometer on giotto*, *Space Science Reviews*, 90, 45–52.
- Eberhardt P. and Krankowsky D. (1995) *The electron temperature in the inner coma of comet P/Halley.*, *Astronomy and Astrophysics*, 295, 795.
- Edberg N. J. T., Eriksson A. I., Odelstad E. et al. (2015) *Spatial distribution of low-energy plasma around comet 67p/cg from rosetta measurements*, *Geophysical Research Letters*, 42, 4263–4269.
- Engelhardt I. A. D., Eriksson A. I., Vigren E. et al. (2018) *Cold electrons at comet 67p/churyumov-gerasimenko*, *A&A*, 616, A51.
- Eriksson A. I., Boström R., Gill R. et al. (2007) *RPC-LAP: The Rosetta Langmuir Probe Instrument*, *Space Science Reviews*, 128, 729–744.
- Eriksson A. I., Engelhardt I. A. D., André M. et al. (2017) *Cold and warm electrons at comet 67P/Churyumov-Gerasimenko*, *Astron. Astrophys.*, 605, A15.
- Evershed J. (1907) *Spectrum of Comet d 1907 (Daniel)*, *Mon. Not. R. Astron. Soc.*, 68, 16.
- Farquhar R. W. (2001) *The flight of isee-3/ice: Origins, mission history, and a legacy*, *The Journal of the Astronautical Sciences*, 49, 23–73.
- Finson M. J. and Probst R. F. (1968) *A theory of dust comets. I. Model and equations*, *Astrophys. J.*, 154, 327–352.
- Florescu-Mitchell A. and Mitchell J. (2006) *Dissociative recombination*, *Physics Reports*, 430, 277–374.
- Fowler A. (1907) *The origin of certain bands in the spectra of sunspots*, *Monthly Notices of the Royal Astronomical Society*, 67, 530–534.
- Fowler A. (1910) *Comets of 1909, investigations relating to the spectra of*, *Monthly Notices of the Royal Astronomical Society*, 70, 484–496.
- Fox J. L., Galand M. I., and Johnson R. E. (2008) *Energy deposition in planetary atmospheres by charged particles and solar photons*, *Space Science Reviews*, 139, 3–62.
- Fuselier S. A., Altwegg K., Balsiger H. et al. (2016) *Ion chemistry in the coma of comet 67P near perihelion*, *Monthly Notices of the Royal Astronomical Society*, 462, S67–S77.
- Galand M., Feldman P. D., Bockelée-Morvan D. et al. (2020) *Far-ultraviolet aurora identified at comet 67P/Churyumov-Gerasimenko*, *Nature Astronomy*, 4, 1084–1091.
- Galand M., Héritier K. L., Odelstad E. et al. (2016) *Ionospheric plasma of comet 67P probed by Rosetta at 3 au from the Sun*, *Monthly Notices of the Royal Astronomical Society*, 462, S331–S351.
- Gan L. and Cravens T. E. (1990) *Electron energetics in the inner coma of comet halley*, *Journal of Geophysical Research: Space Physics*, 95, 6285–6303.
- Gasc S., Altwegg K., Balsiger H. et al. (2017) *Change of outgassing pattern of 67P/Churyumov-Gerasimenko during the March 2016 equinox as seen by ROSINA*, *Mon. Not. R. Astron. Soc.*, 469, S108–S117.
- Geiss J., Altwegg K., Anders E. et al. (1991) *Interpretation of the ion mass spectra in the mass per charge range 25-35 amu/e obtained in the inner coma of Halley's comet by the HIS-sensor of the Giotto IMS experiment*, *Astron. Astrophys.*, 247, 226–234.
- Gilet N., Henri P., Wattieaux G. et al. (2017) *Electrostatic potential radiated by a pulsating charge in a two-electron temperature plasma*, *Radio Science*, 52, 1432–1448.
- Gilet N., Henri P., Wattieaux G. et al. (2020) *Observations of a mix of cold and warm electrons by RPC-MIP at 67P/Churyumov-Gerasimenko*, *A&A*, 640, A110.
- Glassmeier K.-H. (2017) *Interaction of the solar wind with comets: a Rosetta perspective*, *Philosophical Transactions of the Royal Society of London Series A*, 375, 20160256.
- Glassmeier K.-H., Boehnhardt H., Koschny D. et al. (2007) *The Rosetta Mission: Flying Towards the Origin of the Solar System*, *Space Sci. Rev.*, 128, 1–21.
- Goetz C., Gunell H., Volwerk M. et al. (2021) *Cometary plasma science*, *Experimental Astronomy*.
- Goetz C., Koenders C., Hansen K. C. et al. (2016a) *Structure and evolution of the diamagnetic cavity at comet 67P/Churyumov-Gerasimenko*, *Monthly Notices of the Royal Astronomical Society*, 462, S459–S467.
- Goetz C., Koenders C., Richter, I. et al. (2016b) *First detection of a diamagnetic cavity at comet 67p/churyumov-gerasimenko*, *A&A*, 588, A24.
- Goldstein B. E., Altwegg K., Balsiger H., Fuselier S. A. et al. (1989) *Observations of a shock and a recombination layer at the contact surface of comet halley*, *Journal of Geophysical Research: Space Physics*, 94, 17251–17257.
- Goldstein R., Burch J. L., Mokashi P. et al. (2015) *The Rosetta Ion and Electron Sensor (IES) measurement of the development of pickup ions from comet 67P/Churyumov-Gerasimenko*, *Geophys. Res. Lett.*, 42, 3093–3099.
- Goldstein R., Burch J. L., Mokashi P. et al. (2017) *Two years of solar wind and pickup ion measurements at comet 67P/Churyumov-Gerasimenko*, *Mon. Not. R. Astron. Soc.*, 469, S262–S267.
- Gombosi T., Burch, J.L., and Horanyi, M. (2015) *Negatively charged nano-grains at 67P/Churyumov-Gerasimenko*, *Astron. Astrophys.*
- Gombosi T. I. (1987) *Charge exchange avalanche at the come-*

- topause, *Geophysical Research Letters*, 14, 1174–1177.
- Gombosi T. I. (2015) *Physics of Cometary Magnetospheres*, chap. 10, pp. 169–188, American Geophysical Union (AGU).
- Gombosi T. I., De Zeeuw D. L., Häberli R. M. et al. (1996) *Three-dimensional multiscale mhd model of cometary plasma environments*, *Journal of Geophysical Research: Space Physics*, 101, 15233–15253.
- Gombosi T. I., Nagy A. F., and Cravens T. E. (1986) *Dust and neutral gas modeling of the inner atmospheres of comets*, *Reviews of Geophysics*, 24, 667–700.
- Grad H. (1949) *On the kinetic theory of rarefied gases*, *Communications on Pure and Applied Mathematics*, 2, 331–407.
- Gringauz K. I., Gombosi T. I., Tátrallyay M. et al. (1986) *Detection of a new “chemical” boundary at comet Halley*, *Geophys. Res. Lett.*, 13, 613–616.
- Grün E., Agarwal J., Altbelli N. et al. (2016) *The 19 feb. 2016 outburst of comet 67p/cg: An esa rosetta multi-instrument study*, *Monthly Notices of the Royal Astronomical Society*.
- Hajra R., Henri P., Myllys M. et al. (2018) *Cometary plasma response to interplanetary corotating interaction regions during 2016 June–September: a quantitative study by the Rosetta Plasma Consortium*, *Monthly Notices of the Royal Astronomical Society*, 480, 4544–4556.
- Hansen K. C., Altwegg K., Berthelier J. J. et al. (2016) *Evolution of water production of 67P/Churyumov-Gerasimenko: An empirical model and a multi-instrument study*, *Mon. Not. R. Astron. Soc.*, 462, S491–S506.
- Haser L. (1957) *Distribution d’intensité dans la tête d’une comète*, *Bulletin de la Societe Royale des Sciences de Liège*, 43, 740–750.
- Haser L., Oset S., and Bodewits D. (2020) *Intensity distribution in the heads of comets*, *The Planetary Science Journal*, 1, 83.
- Hässig M., Altwegg K., Balsiger H. et al. (2015) *Time variability and heterogeneity in the coma of 67p/churyumov-gerasimenko*, *Science*, 347.
- Heays A. N., Bosman A. D., and van Dishoeck E. F. (2017) *Photodissociation and photoionisation of atoms and molecules of astrophysical interest*, *A&A*, 602, A105.
- Henri P., Vallières X., Hajra R. et al. (2017) *Diamagnetic region(s): structure of the unmagnetized plasma around Comet 67P/CG*, *Monthly Notices of the Royal Astronomical Society*, 469, S372–S379.
- Heritier K. L., Altwegg K., Balsiger H. et al. (2017) *Ion composition at comet 67P near perihelion: Rosetta observations and model-based interpretation*, *Mon. Not. R. Astron. Soc.*, 469, S427–S442.
- Heritier K. L., Galand, M., Henri, P. et al. (2018) *Plasma source and loss at comet 67p during the rosetta mission*, *A&A*, 618, A77.
- Heritier K. L., Henri P., Vallières X. et al. (2017) *Vertical structure of the near-surface expanding ionosphere of comet 67P probed by Rosetta*, *Monthly Notices of the Royal Astronomical Society*, 469, S118–S129.
- Hoffmeister C. (1943) *Physikalische Untersuchungen an Kometen. I. Die Beziehungen des primären Schweifstrahls zum Radiusvektor. Mit 2 Abbildungen.*, *ZAp*, 22, 265.
- Houpis H. L. F. and Mendis D. A. (1980) *Physicochemical and dynamical processes in cometary ionospheres. I - The basic flow profile*, *The Astrophysical Journal*, 239, 1107–1118.
- Huebner W. and Markiewicz W. (2000) *The temperature and bulk flow speed of a gas effusing or evaporating from a surface into a void after reestablishment of collisional equilibrium*, *Icarus*, 148, 594–596.
- Huebner W. and Mukherjee J. (2015) *Photoionization and photodissociation rates in solar and blackbody radiation fields*, *Planetary and Space Science*, 106, 11–45.
- Huebner W. F., Giguere P. T., and Slattery W. L. (1982) in *Comets* (L. L. Wilkening, ed.), pp. 496–515, University of Arizona Press.
- Huebner W. F., Keady J. J., and Lyon S. P. (1992) *Solar photo rates for planetary atmospheres and atmospheric pollutants*, *Astrophysics and Space Science*, 195, 1–294.
- Hunter E. P. L. and Lias S. G. (1998) *Evaluated gas phase basicities and proton affinities of molecules: An update*, *Journal of Physical and Chemical Reference Data*, 27, 413–656.
- Ip W. H. (2004) in *Comets II* (M. C. Festou, H. U. Keller, and H. A. Weaver, eds.), p. 605, University of Arizona Press.
- Ip W. H. and Axford W. I. (1982) in *IAU Colloq. 61: Comet Discoveries, Statistics, and Observational Selection* (L. L. Wilkening, ed.), pp. 588–634.
- Ip W.-H. and Axford W. I. (1987) *The formation of a magnetic-field-free cavity at comet Halley*, *Nature*, 325, 418–419.
- Itikawa Y. (2002) *Cross sections for electron collisions with carbon dioxide*, *Journal of Physical and Chemical Reference Data*, 31, 749–767.
- Itikawa Y. and Mason N. (2005) *Cross sections for electron collisions with water molecules*, *Journal of Physical and Chemical Reference Data*, 34, 1–22.
- IUPAC (1978) *Recommendations for symbolism and nomenclature for mass spectroscopy*, *Pure and Applied Chemistry*, 50, 65–74.
- Jeans J. (1923) *The Dynamical Theory of Gases*, Cambridge Library Collection - Physical Sciences, Cambridge University Press.
- Johansson F. L., Eriksson A. I., Gilet N. et al. (2020) *A charging model for the Rosetta spacecraft*, *Astron. Astrophys.*, 642, A43.
- Johansson F. L., Eriksson A. I., Vignen E. et al. (2021) *Plasma densities, flow and Solar EUV flux at comet 67P - A cross-calibration approach*, *arXiv e-prints*, arXiv:2106.15491.
- Johansson F. L., Odelstad E., Paulsson J. J. P. et al. (2017) *Rosetta photoelectron emission and solar ultraviolet flux at comet 67P*, *Monthly Notices of the Royal Astronomical Society*, 469, S626–S635.
- Koenders C., Glassmeier K.-H., Richter I. et al. (2015) *Dynamical features and spatial structures of the plasma interaction region of 67p/churyumov-gerasimenko and the solar wind*, *Planetary and Space Science*, 105, 101–116.
- Krankowsky D., Lämmerzahl P., Herrwerth I. et al. (1986) *In situ gas and ion measurements at comet halley*, *Nature*, 321, 326–329.
- Krasnopolsky V. A., Greenwood J. B., and Stancil P. C. (2004) *X-ray and extreme ultraviolet emissions from comets*, *Space Science Reviews*, 113, 271–373.
- Körösmezey A., Cravens T. E., Gombosi T. I. et al. (1987) *A new model of cometary ionospheres*, *Journal of Geophysical Research: Space Physics*, 92, 7331–7340.
- Laframboise J. G. (1966) *Theory of Spherical and Cylindrical Langmuir Probes in a Collisionless, Maxwellian Plasma at Rest.*, Ph.D. thesis, UNIVERSITY OF TORONTO (CANADA).
- Lallement R. (2012) *Charge-exchange X-ray emission at hot/cool gas interfaces*, *Astronomische Nachrichten*, 333, 347.
- Larsson M., Geppert W. D., and Nyman G. (2012) *Ion chemistry in space*, *Reports on Progress in Physics*, 75, 066901.

- Le Roy L., Altwegg, Kathrin, Balsiger, Hans et al. (2015) *Inventory of the volatiles on comet 67p/churyumov-gerasimenko from rosetta/rosina*, *A&A*, 583, A1.
- Lean J. (1991) *Variations in the sun's radiative output*, *Reviews of Geophysics*, 29, 505–535.
- Lisse C. M., Dennerl K., Englhauser J. et al. (1996) *Discovery of x-ray and extreme ultraviolet emission from comet c/hyakutake 1996 b2*, *Science*, 274, 205–209.
- LLera K., Burch J. L., Goldstein R. et al. (2020) *Simultaneous observation of negatively and positively charged nanograins at comet 67p/churyumov-gerasimenko*, *Geophysical Research Letters*, 47, e2019GL086147, e2019GL086147 2019GL086147.
- Lowry S., Fitzsimmons A., Lamy P. et al. (2008) *Kuiper Belt Objects in the Planetary Region: The Jupiter-Family Comets*, p. 397.
- Madanian H., Cravens T. E., Burch J. et al. (2017) *Plasma Environment around Comet 67P/Churyumov-Gerasimenko at Perihelion: Model Comparison with Rosetta Data*, *Astron. J.*, 153, 30.
- Madanian H., Cravens T. E., Rahmati A. et al. (2016) *Suprathermal electrons near the nucleus of comet 67P/Churyumov-Gerasimenko at 3 AU: Model comparisons with Rosetta data*, *Journal of Geophysical Research (Space Physics)*, 121, 5815–5836.
- Mandt K. E., Eriksson A., Beth A. et al. (2019) *Influence of collisions on ion dynamics in the inner comae of four comets*, *Astron. Astrophys.*, 630, A48.
- Marshall R., Markkanen J., Gerig S.-B. et al. (2020) *The dust-to-gas ratio, size distribution, and dust fall-back fraction of comet 67p/churyumov-gerasimenko: Inferences from linking the optical and dynamical properties of the inner comae*, *Frontiers in Physics*, 8, 227.
- McGowan J. and Mitchell J. (1984) in *Electron–Molecule Interactions and their Applications* (L. Christophorou, ed.), pp. 65–88, Academic Press.
- Mendis D. A. and Horányi M. (2013) *Dusty plasma effects in comets: Expectations for rosetta*, *Reviews of Geophysics*, pp. n/a–n/a.
- Mendis D. A., Houppis H. L. F., and Marconi M. L. (1985) *The Physics of Comets*, vol. 10.
- Merlino R. L. (2014) *25 years of dust acoustic waves*, *Journal of Plasma Physics*, 80, 773–786.
- Meyer-Vernet N. (2013) *On the charge of nanograins in cold environments and Enceladus dust*, *Icarus*, 226, 583–590.
- Meyer-Vernet N., Couturier P., Hoang S. et al. (1986) *Plasma diagnosis from thermal noise and limits on dust flux or mass in comet giacobini-zinner*, *Science*, 232, 370–374.
- Mott-Smith H. M. and Langmuir I. (1926) *The theory of collectors in gaseous discharges*, *Phys. Rev.*, 28, 727–763.
- Muller P. (1994) *Glossary of terms used in physical organic chemistry (iupac recommendations 1994)*; *Pure and Applied Chemistry*, 66, 1077–1184.
- Myllys M., Henri P., Galand M. et al. (2019) *Plasma properties of suprathermal electrons near comet 67p/churyumov-gerasimenko with rosetta*, *A&A*, 630, A42.
- Neubauer F. M. (1987) *Giotto magnetic-field results on the boundaries of the pile-up region and the magnetic cavity*, *Astronomy & Astrophysics*, 187, 73–79.
- Neubauer F. M., Glassmeier K. H., Pohl M. et al. (1986) *First results from the giotto magnetometer experiment at comet halley*, *Nature*, 321, 352–355.
- Nilsson H., Stenberg Wieser G., Behar E. et al. (2015) *Birth of a comet magnetosphere: A spring of water ions*, *Science*, 347, aaa0571.
- Nilsson H., Wieser G. S., Behar E. et al. (2017) *Evolution of the ion environment of comet 67P during the Rosetta mission as seen by RPC-ICA*, *Mon. Not. R. Astron. Soc.*, 469, S252–S261.
- Nilsson H., Williamson H., Bergman S. et al. (2020) *Average cometary ion flow pattern in the vicinity of comet 67P from moment data*, *Monthly Notices of the Royal Astronomical Society*, 498, 5263–5272.
- Obridko V. N. and Vaisberg O. L. (2017) *On the history of the solar wind discovery*, *Solar System Research*, 51, 165–169.
- Odelstad E., Eriksson A. I., Johansson F. L. et al. (2018) *Ion Velocity and Electron Temperature Inside and Around the Diamagnetic Cavity of Comet 67P*, *Journal of Geophysical Research (Space Physics)*, 123, 5870–5893.
- Odelstad E., Stenberg-Wieser G., Wieser M. et al. (2017) *Measurements of the electrostatic potential of Rosetta at comet 67P*, *Monthly Notices of the Royal Astronomical Society*, 469, S568–S581.
- Ogilvie K. W., Coplan M. A., Bochsler P. et al. (1986) *Ion composition results during the international cometary explorer encounter with giacobini-zinner*, *Science*, 232, 374–377.
- Parker E. N. (1958) *Dynamics of the Interplanetary Gas and Magnetic Fields*, *The Astrophysical Journal*, 128, 664.
- Pedersen A., Grad R., Trotignon J. G. et al. (1986) in *ESLAB Symposium on the Exploration of Halley's Comet* (B. Battrock, E. J. Rolfe, and R. Reinhard, eds.), vol. 250 of *ESA Special Publication*, pp. 425–431.
- Pierrard V., Lazar M., Poedts S. et al. (2016) *The Electron Temperature and Anisotropy in the Solar Wind. Comparison of the Core and Halo Populations*, *Sol. Phys.*, 291, 2165–2179.
- Reinhard R. (1986) *The giotto encounter with comet halley*, *Nature*, 321, 313–318.
- Reme H., Mazelle C., D'Uston C. et al. (1994) *There is no "cometopause" at Comet Halley*, *J. Geophys. Res.*, 99, 2301–2308.
- von Rosenvinge T. T., Brandt J. C., and Farquhar R. W. (1986) *The international cometary explorer mission to comet giacobini-zinner*, *Science*, 232, 353–356.
- Rosén S., Derkatch A., Semaniak J. et al. (2000) *Recombination of simple molecular ions studied in storage ring: dissociative recombination of h2o+*, *Faraday Discuss.*, 115, 295–302.
- Rubin M., Hansen K. C., Gombosi T. I. et al. (2009) *Ion composition and chemistry in the coma of Comet 1P/Halley—A comparison between Giotto's Ion Mass Spectrometer and our ion-chemical network*, *Icarus*, 199, 505–519.
- Sagdeev R. Z., Evlanov E. N., Fomenkova M. N. et al. (1989) *Small-size dust particles near Halley's comet*, *Advances in Space Research*, 9, 263–267.
- Sauer K., Bogdanov A., and Baumgartel K. (1995) *The protonopause - an ion composition boundary in the magnetosheath of comets, Venus and Mars*, *Advances in Space Research*, 16, 153–158.
- Schunk R. and Nagy A. (2009) *Ionospheres: Physics, Plasma Physics, and Chemistry*, Cambridge Atmospheric and Space Science Series, Cambridge University Press, 2 edn.
- Schwenn R., Ip W. H., Rosenbauer H. et al. (1987) *Ion Temperature and Flow Profiles in Comet p/ Halley's Close Environment*, *Astronomy and Astrophysics*, 187, 160.
- Sembay S., Branduardi-Raymont G., Eastwood J. P. et al. (2012) *AXIOM: Advanced X-ray imaging of the magnetosheath*, *Astronomische Nachrichten*, 333, 388–392.



- Simon Wedlund C., Alho M., Gronoff G. et al. (2017) *Hybrid modelling of cometary plasma environments. I. Impact of photoionisation, charge exchange, and electron ionisation on bow shock and cometopause at 67P/Churyumov-Gerasimenko*, *Astron. Astrophys.*, 604, A73.
- Simon Wedlund C., Behar E., Kallio E. et al. (2019a) *Solar wind charge exchange in cometary atmospheres: II. Analytical model*, *A&A*, 630, A36.
- Simon Wedlund C., Behar E., Nilsson H. et al. (2019b) *Solar wind charge exchange in cometary atmospheres: III. Results from the Rosetta mission to comet 67P/Churyumov-Gerasimenko*, *A&A*, 630, A37.
- Simon Wedlund C., Behar E., Nilsson H. et al. (2020) *Solar wind charge exchange in cometary atmospheres. III. Results from the Rosetta mission to comet 67P/Churyumov-Gerasimenko (Corrigendum)*, *A&A*, 640, C3.
- Simon Wedlund C., Bodewits D., Alho M. et al. (2019c) *Solar wind charge exchange in cometary atmospheres: I. Charge-changing and ionization cross sections for He and H particles in H<sub>2</sub>O*, *A&A*, 630, A35.
- Simon Wedlund C., Kallio E., Alho M. et al. (2016) *The atmosphere of comet 67P/Churyumov-Gerasimenko diagnosed by charge-exchanged solar wind alpha particles*, *Astron. Astrophys.*, 587, A154.
- Sishtla C. P., Divin A., Deca J. et al. (2019) *Electron trapping in the coma of a weakly outgassing comet*, *Physics of Plasmas*, 26, 102904.
- Slavin J. A. and Holzer R. E. (1981) *Solar wind flow about the terrestrial planets. I. Modeling bow shock position and shape*, *J. Geophys. Res.*, 86, 11401–11418.
- Snodgrass C. and Jones G. H. (2019) *The european space agency's comet interceptor lies in wait*, *Nature Communications*, 10, 5418.
- Somov B. V. (2007) *The Generalized Ohm's Law in Plasma*, pp. 193–204, Springer New York, New York, NY.
- Spitzer Lyman J. (1949) in *The Atmospheres of the Earth and Planets* (G. P. Kuiper, ed.), p. 211.
- Stephenson P., Galand M., Deca J. et al. (2022) *A collisional test-particle model of electrons at a comet*, *Monthly Notices of the Royal Astronomical Society*, 511, 4090–4108.
- Stephenson P., Galand M., Feldman P. D. et al. (2021) *Multi-instrument analysis of far-ultraviolet aurora in the southern hemisphere of comet 67P/Churyumov-Gerasimenko*, *Astron. Astrophys.*, 647, A119.
- Szegő K., Glassmeier K.-H., Bingham R. et al. (2000) *Physics of mass loaded plasmas*, *Space Science Reviews*, 94, 429–671.
- Trotignon J. G., Michau J. L., Lagoutte D. et al. (2007) *RPC-MIP: the Mutual Impedance Probe of the Rosetta Plasma Consortium*, *Space Science Reviews*, 128, 713–728.
- Valentini F., Trávníček P., Califano F. et al. (2007) *A hybrid-vlasov model based on the current advance method for the simulation of collisionless magnetized plasma*, *Journal of Computational Physics*, 225, 753–770.
- Viggiano A. A., Ehlerding A., Hellberg F. et al. (2005) *Rate constants and branching ratios for the dissociative recombination of CO<sub>2</sub><sup>+</sup>*, *The Journal of Chemical Physics*, 122, 226101.
- Vigren E., André M., Edberg N. J. T. et al. (2017) *Effective ion speeds at ~200-250 km from comet 67P/Churyumov-Gerasimenko near perihelion*, *Mon. Not. R. Astron. Soc.*, 469, S142–S148.
- Vigren E., Edberg N. J. T., Eriksson A. I. et al. (2019) *The evolution of the electron number density in the coma of comet 67p at the location of Rosetta from 2015 November through 2016 March*, *The Astrophysical Journal*, 881, 6.
- Vigren E. and Eriksson A. I. (2019) *On the ion-neutral coupling in cometary comae*, *Monthly Notices of the Royal Astronomical Society*, 482, 1937–1941.
- Vigren E., Eriksson A. I., and Bergman S. (2022) *On Positively Charged Dust in the Coma of Comet 67P*, *Mon. Not. R. Astron. Soc.*.
- Vigren E., Eriksson A. I., Johansson F. L. et al. (2021) *A case for a small to negligible influence of dust charging on the ionization balance in the coma of comet 67p*, *The Planetary Science Journal*, 2, 156.
- Vigren E. and Galand M. (2013) *Predictions of Ion Production Rates and Ion Number Densities within the Diamagnetic Cavity of Comet 67P/Churyumov-Gerasimenko at Perihelion*, *Astron. Astrophys. J.*, 772, 33.
- Vigren E., Galand M., Eriksson A. I. et al. (2015) *On the electron-to-neutral number density ratio in the coma of comet 67p/Churyumov-Gerasimenko: Guiding expression and sources for deviations*, *The Astrophysical Journal*, 812, 54.
- von Steiger R., Schwadron N. A., Fisk L. A. et al. (2000) *Composition of quasi-stationary solar wind flows from Ulysses/Solar Wind Ion Composition Spectrometer*, *J. Geophys. Res.*, 105, 27217–27238.
- Wargelin B. J., Beiersdorfer P., and Brown G. V. (2008) *EBIT charge-exchange measurements and astrophysical applications*, *Canadian Journal of Physics*, 86, 151–169.
- Wattiaux G., Gilet N., Henri P. et al. (2019) *RPC-MIP observations at comet 67P/Churyumov-Gerasimenko explained by a model including a sheath and two populations of electrons*, *A&A*, 630, A41.
- Wattiaux G., Henri P., Gilet N. et al. (2020) *Plasma characterization at comet 67P between 2 and 4 AU from the Sun with the RPC-MIP instrument*, *A&A*, 638, A124.
- Whipple F. L. (1950) *A comet model. I. The acceleration of Comet Encke*, *The Astrophysical Journal*, 111, 375–394.
- Wigner E. P. (1948) *On the behavior of cross sections near thresholds*, *Phys. Rev.*, 73, 1002–1009.
- Williamson H. N., Nilsson H., Stenberg Wieser G. et al. (2020) *Momentum and Pressure Balance of a Comet Ionosphere*, *Geophys. Res. Lett.*, 47, e88666.
- Woods T. N., Eparvier F. G., Bailey S. M. et al. (2005) *Solar EUV Experiment (SEE): Mission overview and first results*, *Journal of Geophysical Research: Space Physics*, 110.
- Wu C. S. and Davidson R. C. (1972) *Electromagnetic instabilities produced by neutral-particle ionization in interplanetary space*, *J. Geophys. Res.*, 77, 5399.
- Zavilopulo A. N., Chipev F. F., and Shpenik O. B. (2005) *Ionization of nitrogen, oxygen, water, and carbon dioxide molecules by near-threshold electron impact*, *Technical Physics*, 50, 402–407.
- Zwicky R. D., Baker D. N., Bame S. J. et al. (1986) *Three component plasma electron distribution in the intermediate ionized coma of comet Giacobini-Zinner*, *Geophysical Research Letters*, 13, 401–404.

---

This 2-column preprint was prepared with the AAS L<sup>A</sup>T<sub>E</sub>X macros v5.2.